

AN ABSTRACT OF THESIS OF

Wade R. Marcum for the degree of Master of Science in Nuclear Engineering presented on January 23, 2008.

Title: Thermal Hydraulic Analysis of the Oregon State TRIGA[®] Reactor Using RELAP5-3D

Abstract approved:

Brian G. Woods

Oregon State University has recently conducted a complete core conversion analysis as part of the Reduced Enrichment for Research and Test Reactors Program. The goals of the thermal hydraulic analyses were to calculate natural circulation flow rates, coolant temperatures and fuel temperatures as a function of core power for both the Highly Enriched Uranium (HEU) and Low Enriched Uranium (LEU) cores; for steady state and pulsed operation, calculate peak values of fuel temperature, cladding temperature, surface heat flux as well as critical heat flux ratio (CHFR) and temperature profiles in hot channel for both the HEU and LEU cores; finally, perform accident analyses for the accident scenarios identified in the Oregon State TRIGA[®] Reactor (OSTR) Safety Analysis Report (SAR).

RELAP5-3D Version 2.4.2 was used for all computational modeling during the thermal hydraulics analysis. This is a lumped parameter code forcing engineering assumptions to be made during the analysis. A single hot channel model's results are compared to that produced from more refined two and eight channel models in order to identify variations in thermal hydraulic characteristics as a function of spatial refinement.

© Copyright by Wade R. Marcum

January 23, 2008

All Rights Reserved

Thermal Hydraulic Analysis of the Oregon State TRIGA[®] Reactor Using RELAP5-3D

by

Wade R. Marcum

A THESIS

Submitted to

Oregon State University

in partial fulfillment of
the requirements for the
degree of

Master of Science

Presented January 23, 2008

Commencement June 2008

Master of Science thesis of Wade R. Marcum presented on January 23, 2008.

APPROVED:

Major Professor, representing Nuclear Engineering

Head of the Department of Nuclear Engineering and Radiation Health Physics

Dean of the Graduate School

I understand that my thesis will become part of the permanent collection of Oregon State University libraries. My signature below authorizes release of my thesis to any reader upon request.

Wade R. Marcum, Author

ACKNOWLEDGEMENTS

I would like to take this opportunity to recognize my advisor Dr. Brian Woods, who, through his guidance and patience has helped me become a better student and person.

I would like to thank the faculty members in the Oregon State University Nuclear Engineering Department that have helped me with the core conversion analysis through their knowledge and opinion, in particular Dr. Mike Hartman, Dr. Steve Reese, Dr. Todd Palmer, and Todd Keller.

I would lastly like to acknowledge my dad, Scott; mom, Teeny; sister, Jena; and fiancé, Molly. Without their continual support I would have never found myself in this position.

TABLE OF CONTENTS

	<u>Page</u>
1. INTRODUCTION	1
1.1 RESEARCH OBJECTIVE	1
1.2 ANALYSIS ASSUMPTIONS	2
1.3 ANALYSIS LIMITATIONS	4
1.4 OVERVIEW OF FOLLOWING CHAPTERS	5
2. SURVEY OF LITERATURE	6
2.1 PREVIOUS TRIGA [®] REACTOR THERMAL HYDRAULIC ANALYSES	6
2.2 PREVIOUS RELAP5-3D THERMAL HYDRAULIC ANALYSES	6
2.3 PREVIOUS CHF STUDIES RELEVANT TO THE OSTR THERMAL HYDRAULIC ANALYSIS	7
2.3.1 Pool Boiling	7
2.3.2 Natural Convection Boiling	9
2.3.3 Forced Convection Boiling	10
3. OREGON STATE TRIGA [®] REACTOR	13
3.1 OSTR OVERVIEW	13
3.2 HEU/LEU CORE COMPONENTS	15
4. DESCRIPTION OF THE RELAP5-3D MODELS	27
4.1 THEORETICAL JUSTIFICATION FOR SINGLE CHANNEL MODEL	27
4.2 SINGLE CHANNEL MODEL DESCRIPTION	32
4.2.1 System	32
4.2.2 Coolant Source (100)	34
4.2.3 Cold Leg (101)	35
4.2.4 Horizontal Connector (102)	36
4.2.5 Hot Channel (103)	37
4.2.6 Coolant Sink (104)	42
4.2.7 General Volume Parameters	43
4.2.8 Hot Channel Heat Structure	43
4.3 TWO CHANNEL MODEL DESCRIPTION	48
4.4 EIGHT CHANNEL MODEL DESCRIPTION	50

TABLE OF CONTENTS (Continued)

	<u>Page</u>
5. STEADY STATE ANALYSIS	52
5.1 CRITICAL HEAT FLUX CORRELATION COMPARISON	52
5.2 1, 2, & 8 CHANNEL MODEL RESULTS COMPARISON	55
5.2.1 HEU Beginning of Life Normal Core	55
5.2.2 LEU Beginning of Life Normal Core	60
6. PULSE ANALYSIS	64
6.1 DISCUSSION	64
6.1.1 External Explicit Solution	65
6.1.2 External Numerical Solution	65
6.1.3 RELAP5-3D Numerical Solution	67
6.2 PULSE RESULTS	67
6.2.1 Power Trace Comparison	67
6.2.2 Maximum Fuel Temperature Comparison	69
6.2.3 Incorporating Moderator Feedback	72
7. CONCLUSION	74
7.1 STEADY STATE	74
7.2 PULSE	75
7.3 FUTURE WORK	75
BIBLIOGRAPHY	77
NOMENCLATURE	84
APPENDICES	86
A APPENDIX (SINGLE CHANNEL RESULTS)	87
A.1 POWER SUMMARY	87
A.1.1 HEU Power Summary	87
A.1.2 LEU Power Summary	90
A.2 STEADY STATE RESULTS	97
A.2.1 HEU Beginning of Life Normal Core	97
A.2.2 HEU Middle of Life Normal Core	102
A.2.3 HEU End of Life Normal Core	106

TABLE OF CONTENTS (Continued)

	<u>Page</u>
A.2.4 LEU Beginning of Life ICIT Core	108
A.2.5 LEU Middle of Life ICIT Core.....	112
A.2.6 LEU End of Life ICIT Core.....	115
A.3 PULSE RESULTS.....	119
A.3.1 HEU End of Life Normal Core.....	119
A.3.2 LEU Beginning of Life ICIT Core	124
A.3.3 LEU Middle of Life ICIT Core.....	128
A.3.4 LEU End of Life ICIT Core.....	131
B APPENDIX (PRKE DERIVATION).....	135
B.1 PRKE DERIVATION.....	135
B.2 MATLAB [®] CODE	140
C APPENDIX (OSTR EXPERIMENTAL TEMPERATURE MAPPING).....	143
C.1 INTRODUCTION.....	143
C.2 EQUIPMENT AND METHODS.....	143
C.2.1 Data Acquisition Equipment.....	143
C.2.2 Hardware Acquired for Experimental Assembly.....	143
C.2.3 Overview of Experimental Procedure.....	144
C.3 RESULTS.....	147

LIST OF FIGURES

<u>Figure</u>	<u>Page</u>
3.1: VERTICAL SECTIONAL VIEW OF OSTR	13
3.2: ISOMETRIC AND SECTIONAL ISOMETRIC VIEW OF THE OSTR.....	14
3.3: TOP VIEW OF UPPER GRID PLATE IN OSTR.....	15
3.4: SCHEMATIC OF THE OSTR CORE FOR THE HEU CORE IN NORMAL CONFIGURATION	16
3.5: SCHEMATIC OF THE OSTR CORE FOR THE LEU CORE IN NORMAL CONFIGURATION	16
3.6: TRIGA ^(R) FUEL ELEMENT DESIGN UTILIZED IN THE OSTR CORE.....	18
3.7: CORE POWER DISTRIBUTION (HEU BOL NORMAL CORE)	19
3.8: CORE POWER DISTRIBUTION (LEU BOL NORMAL CORE)	19
3.9: HOT CHANNEL FUEL POWER DISTRIBUTION (HEU-BOL NORMAL CORE).....	21
3.10: HOT CHANNEL FUEL POWER DISTRIBUTION (LEU-BOL NORMAL CORE)	21
3.11: HOT CHANNEL FUEL RADIAL POWER FACTOR PROFILE.....	23
3.12: HOT CHANNEL FUEL AXIAL POWER FACTOR PROFILE.....	23
3.13 CORE POWER, FUEL ELEMENT AXIAL POWER, FUEL ELEMENT RADIAL POWER PROFILE	25
4.1: SUBCHANNEL COMPARISON FOR CROSS FLOW JUSTIFICATION	28
4.2: EQUILIBRIUM QUALITY TO MASS FLUX SENSITIVITY COMPARISON.....	31
4.3: SINGLE CHANNEL RELAP5-3D MODEL SCHEMATIC	32
4.4: COMPARISON OF OSTR FUEL ROD AXIAL CHARACTERISTICS AND RELAP SUBCHANNEL	34
4.5: HEXAGONAL ARRAY AXIAL AVERAGE UNIT SUBCHANNEL DIMENSIONS	37
4.6: SUDDEN EXPANSION (A) AND SUDDEN CONTRACTION (B)	42
4.7: CROSS SECTIONAL VIEW OF FUEL ELEMENT	45
4.8: RADIAL NODAL BREAKDOWN OF FUEL ELEMENT	46
4.9: TWO CHANNEL RELAP5-3D MODEL SCHEMATIC	49
4.10: EIGHT CHANNEL RELAP5-3D MODEL SCHEMATIC	51
5.1: AXIAL CHFR DISTRIBUTION, CORRELATION COMPARISON	53
5.2: AXIAL CHFR DISTRIBUTION, CORRELATION COMPARISON	53
5.3: NODAL FUEL TEMPERATURE DISTRIBUTION FOR 1, 2, & 8 CHANNEL MODEL.....	55
5.4: RADIAL HOT CHANNEL FUEL TEMP. DISTRIBUTION FOR 1, 2, & 8 CHANNEL MODEL	56
5.5: AXIAL HOT CHANNEL FUEL TEMP. DISTRIBUTION FOR 1, 2, & 8 CHANNEL MODEL	57
5.6: AXIAL BULK COOLANT TEMPERATURE DISTRIBUTION FOR 1, 2, & 8 CHANNEL MODEL.....	57
5.7: MASS FLUX AND EQUILIBRIUM QUALITY DISTRIBUTION FOR 1, 2, & 8 CHANNEL MODEL.....	58
5.8: AXIAL CHFR DISTRIBUTION FOR 1, 2, & 8 CHANNEL MODEL	59
5.9: NODAL FUEL TEMPERATURE DISTRIBUTION FOR 1, 2, & 8 CHANNEL MODEL.....	60
5.10: RADIAL HOT CHANNEL FUEL TEMP. DISTRIBUTION FOR 1, 2, & 8 CHANNEL MODEL	61

LIST OF FIGURES (Continued)

<u>Figure</u>	<u>Page</u>
5.11: AXIAL HOT CHANNEL FUEL TEMP. DISTRIBUTION FOR 1, 2, & 8 CHANNEL MODEL	61
5.12: AXIAL BULK COOLANT TEMPERATURE DISTRIBUTION FOR 1, 2, & 8 CHANNEL MODEL	62
5.13: MASS FLUX AND EQUILIBRIUM QUALITY DISTRIBUTION FOR 1, 2, & 8 CHANNEL MODEL	62
5.14: AXIAL CHF DISTRIBUTION FOR 1, 2, & 8 CHANNEL MODEL	63
6.1: PULSE POWER TRACE COMPARISON (HEU BEGINNING OF LIFE CORE, \$2.00 INSERTION)	67
6.2: FUEL RADIAL TEMPERATURE AT MAXIMUM FUEL TEMPERATURE TIME	70
6.3: TRANSIENT MAXIMUM FUEL TEMPERATURE COMPARISON	71
6.4: TRANSIENT REACTIVITY COMPARISON	73
A.1: CORE POWER DISTRIBUTION (HEU BEGINNING OF LIFE NORMAL CORE)	87
A.2: CORE POWER DISTRIBUTION (HEU MIDDLE OF LIFE NORMAL CORE)	88
A.3: CORE POWER DISTRIBUTION (HEU END OF LIFE NORMAL CORE)	88
A.4: HEU NORMAL CORE - AXIAL POWER PROFILE VS. DISTANCE FROM FUEL CENTERLINE	89
A.5: HEU NORMAL CORE-RADIAL POWER PROFILE VS. DISTANCE FROM FUEL CENTERLINE	89
A.6: CORE POWER DISTRIBUTION (LEU BEGINNING OF LIFE NORMAL CORE)	90
A.7: CORE POWER DISTRIBUTION (LEU MIDDLE OF LIFE NORMAL CORE)	90
A.8: CORE POWER DISTRIBUTION (LEU END OF LIFE NORMAL CORE)	91
A.9: LEU NORMAL CORE-AXIAL POWER PROFILE VS. DISTANCE FROM FUEL CENTERLINE	91
A.10: LEU NORMAL CORE-RADIAL POWER PROFILE VS. DISTANCE FROM FUEL CENTERLINE	92
A.11: CORE POWER DISTRIBUTION (LEU BEGINNING OF LIFE ICIT CORE)	92
A.12: CORE POWER DISTRIBUTION (LEU MIDDLE OF LIFE ICIT CORE)	93
A.13: CORE POWER DISTRIBUTION (LEU END OF LIFE ICIT CORE)	93
A.14: AXIAL POWER FACTOR (LEU ICIT CORE)	94
A.15: RADIAL POWER FACTOR (LEU ICIT CORE)	94
A.16: CORE POWER DISTRIBUTION (LEU BEGINNING OF LIFE CLICIT CORE)	95
A.17: CORE POWER DISTRIBUTION (LEU MIDDLE OF LIFE CLICIT CORE)	95
A.18: CORE POWER DISTRIBUTION (LEU END OF LIFE CLICIT CORE)	96
A.19: AXIAL POWER FACTOR (LEU CLICIT CORE)	96
A.20: RADIAL POWER FACTOR (LEU CLICIT CORE)	97
A.21: HOT CHANNEL PROPERTIES (HEU BEGINNING OF LIFE NORMAL CORE)	98
A.22: HOT CHANNEL MDNBR (HEU BEGINNING OF LIFE NORMAL CORE)	98
A.23: AXIAL TEMP. DISTRIBUTION AT 18.02 kW (HEU BEGINNING OF LIFE NORMAL CORE)	99
A.24: AXIAL DNBR AT 18.02 kW (HEU BEGINNING OF LIFE NORMAL CORE)	99
A.25: IFE RADIAL TEMP. DIST. AT 15.81 kW (HEU BEGINNING OF LIFE NORMAL CORE)	100

LIST OF FIGURES (Continued)

<u>Figure</u>	<u>Page</u>
A.26: RADIAL FUEL TEMP. DIST. AT 18.02 kW (HEU BEGINNING OF LIFE NORMAL CORE).....	101
A.27: FUEL ELEMENT RADIAL TEMPERATURE DISTRIBUTION AT 1.1 MW _{TH}	101
A.28: HOT CHANNEL PROPERTIES (HEU MIDDLE OF LIFE NORMAL CORE).....	103
A.29: HOT CHANNEL MDNBR (HEU MIDDLE OF LIFE NORMAL CORE)	103
A.30: AXIAL TEMP. DISTRIBUTION AT 18.37 kW (HEU MIDDLE OF LIFE NORMAL CORE).....	104
A.31: HOT CHANNEL AXIAL DNBR AT 18.37 kW (HEU MIDDLE OF LIFE NORMAL CORE).....	104
A.32: RADIAL TEMP. DISTRIBUTION AT 18.37 kW (HEU MIDDLE OF LIFE NORMAL CORE).....	105
A.33: HOT CHANNEL PROPERTIES (HEU END OF LIFE NORMAL CORE).....	106
A.34: HOT CHANNEL MDNBR (HEU END OF LIFE NORMAL CORE)	106
A.35: AXIAL TEMP. DISTRIBUTION AT 16.48 kW (HEU END OF LIFE NORMAL CORE).....	107
A.36: HOT CHANNEL AXIAL DNBR AT 16.48 kW (HEU END OF LIFE NORMAL CORE).....	107
A.37: RADIAL TEMP. DISTRIBUTION AT 16.48 kW (HEU END OF LIFE NORMAL CORE).....	108
A.38: HOT CHANNEL PROPERTIES (LEU BEGINNING OF LIFE ICIT CORE)	109
A.39: HOT CHANNEL MDNBR (LEU BEGINNING OF LIFE ICIT CORE)	109
A.40: AXIAL TEMP. DISTRIBUTION AT 18.47 kW (LEU BEGINNING OF LIFE ICIT CORE).....	110
A.41: HOT CHANNEL AXIAL DNBR AT 18.47 kW (LEU BEGINNING OF LIFE ICIT CORE).....	110
A.42: RADIAL TEMP. DISTRIBUTION AT 18.47 kW (LEU BEGINNING OF LIFE ICIT CORE).....	111
A.43: HOT CHANNEL PROPERTIES (LEU MIDDLE OF LIFE ICIT CORE).....	112
A.44: HOT CHANNEL MDNBR (LEU MIDDLE OF LIFE ICIT CORE)	113
A.45: AXIAL TEMPERATURE DISTRIBUTION AT 18.52 kW (LEU MIDDLE OF LIFE ICIT CORE)	113
A.46: HOT CHANNEL AXIAL DNBR AT 18.52 kW (LEU MIDDLE OF LIFE ICIT CORE).....	114
A.47: RADIAL FUEL TEMP. DISTRIBUTION AT 18.52 kW (LEU MIDDLE OF LIFE ICIT CORE).....	114
A.48: HOT CHANNEL PROPERTIES (LEU END OF LIFE ICIT CORE).....	116
A.49: HOT CHANNEL MDNBR (LEU END OF LIFE ICIT CORE).	116
A.50: AXIAL TEMPERATURE DISTRIBUTION AT 17.61 kW (LEU END OF LIFE ICIT CORE)	117
A.51: HOT CHANNEL AXIAL DNBR AT 17.61 kW (LEU END OF LIFE ICIT CORE).....	117
A.52: RADIAL FUEL TEMP. DISTRIBUTION AT 17.61 kW (LEU END OF LIFE ICIT CORE).....	118
A.53: HEU END OF LIFE NORMAL CORE \$2.00 SHORT POWER/ENERGY TRACE.....	120
A.54: HEU END OF LIFE NORMAL CORE \$2.00 LONG POWER/ENERGY TRACE	120
A.55: PULSE RESULTS SUMMARY (HEU EOL NORMAL CORE).	121
A.56: HEU EOL, SHORT HOT CHANNEL PULSE FUEL TEMPERATURES (\$2.00 INSERTION)	122
A.57: HEU EOL, LONG HOT CHANNEL PULSE FUEL TEMPERATURES (\$2.00 INSERTION).....	122
A.58: FUEL TEMPERATURE DISTRIBUTION AT TIME OF PROMPT MAX FUEL TEMPERATURE.....	123

LIST OF FIGURES (Continued)

<u>Figure</u>	<u>Page</u>
A.59: FUEL TEMPERATURE DISTRIBUTION AT TIME OF DELAYED MAX FUEL TEMPERATURE	123
A.60: HEU END OF LIFE NORMAL, RADIAL TEMP. PROFILE AFTER PULSE.....	123
A.61: INTEGRAL CORE PULSE POWER TRACE (\$2.00 PULSE, LEU ICIT CORE)	125
A.62: PULSE SUMMARY (LEU BEGINNING OF LIFE ICIT CORE).	125
A.63: LEU BEGINNING OF LIFE ICIT, SHORT HOT CHANNEL FUEL TEMP. (\$2.00 PULSE)	126
A.64: LEU BEGINNING OF LIFE ICIT, LONG HOT CHANNEL FUEL TEMPE. (\$2.00 PULSE).....	126
A.65: FUEL TEMPERATURE DISTRIBUTION AT TIME OF PROMPT MAX FUEL TEMPERATURE.....	127
A.66: FUEL TEMPERATURE DISTRIBUTION AT TIME OF DELAYED MAX FUEL TEMPERATURE	127
A.67: HEU BEGINNING OF LIFE ICIT RADIAL TEMP. PROFILE AFTER PULSE.....	127
A.68: PULSE SUMMARY (LEU MIDDLE OF LIFE ICIT CORE)	128
A.69: LEU MIDDLE OF LIFE, SHORT HOT CHANNEL FUEL TEMPERATURES (\$2.00 PULSE)	129
A.70: LEU MIDDLE OF LIFE, LONG HOT CHANNEL FUEL TEMPERATURES (\$2.00 PULSE).....	129
A.71: FUEL TEMPERATURE DISTRIBUTION AT TIME OF PROMPT MAX FUEL TEMPERATURE.....	130
A.72: FUEL TEMPERATURE DISTRIBUTION AT TIME OF DELAYED MAX FUEL TEMPERATURE).....	130
A.73: LEU MIDDLE OF LIFE ICIT, RADIAL TEMP. PROFILE AFTER PULSE (\$2.00 INSERTION)	130
A.74: PULSE SUMMARY (LEU END OF LIFE ICIT CORE).	131
A.75: LEU END OF LIFE, SHORT HOT CHANNEL FUEL TEMPERATURES (\$2.00 PULSE)	132
A.76: LEU END OF LIFE, LONG HOT CHANNEL FUEL TEMPERATURES (\$2.00 PULSE).....	132
A.77: FUEL TEMPERATURE DISTRIBUTION AT TIME OF PROMPT MAX FUEL TEMPERATURE.....	133
A.78: FUEL TEMPERATURE DISTRIBUTION AT TIME OF PROMPT MAX FUEL TEMPERATURE.....	133
A.79: LEU END OF LIFE ICIT, RADIAL TEMP. PROFILE AFTER PULSE (\$2.00 INSERTION)	133
C.1: BLOCK DIAGRAM OF LABVIEW CODE LOGIC IMPLEMENTED DURING THE EXPERIMENT	144
C.2: THE ASSEMBLED CONFIGURATION OF THE DAQ BUCKET TO COMPUTER MODULE	145
C.3: BLOCK DIAGRAM OF THE METHODOLOGY USED TO CONDUCT THE SHUNT CALIBRATION.....	145
C.4: PICTURE OF THE THERMOCOUPLE IN THE OSTR CORE AT STEADY STATE OPERATION	146
C.5: COMPONENTS COMPRISING CURRENT OSTR CORE AND MEASUREMENT LOCATIONS	146
C.6: FIGURE OF CODE AND FRONT PANEL OF LABVIEW DEVELOPED FOR THE EXPERIMENT.....	147
C.7: AXIAL BULK COOLANT TEMPERATURE DISTRIBUTION AT LOCATION 1	147
C.8: AXIAL BULK COOLANT TEMPERATURE DISTRIBUTION AT LOCATION 2	148
C.9: AXIAL BULK COOLANT TEMPERATURE DISTRIBUTION AT LOCATION 3	149
C.10: AXIAL BULK COOLANT TEMPERATURE DISTRIBUTION AT LOCATION 4	149
C.11: AXIAL BULK COOLANT TEMPERATURE DISTRIBUTION AT LOCATION 5	150
C.12: AXIAL BULK COOLANT TEMPERATURE DISTRIBUTION AT LOCATION 6	150
C.13: AXIAL BULK COOLANT TEMPERATURE DISTRIBUTION SUMMARY	151

LIST OF TABLES

<u>Table</u>	<u>Page</u>
2.1: SUMMARY OF CHF LOOK-UP TABLES BOUNDING CONDITIONS.....	11
3.1: CORE COMPONENTS FOR HEU FLIP AND LEU 30/20 CORES.....	15
3.2: COMPARISON OF HEU FLIP AND LEU 30/20 FUEL DESIGNS	17
3.3: HOT CHANNEL POWER SUMMARY.....	24
4.1: TIME DEPENDENT VOLUME BOUNDARY CONDITIONS	35
4.2: VOLUME 100 & 104 GEOMETRIC PARAMETERS	35
4.3: VOLUME 101 GEOMETRIC PARAMETERS	36
4.4: VOLUME 102 GEOMETRIC PARAMETERS	37
4.5: CORE VOLUME NODAL LENGTHS	40
4.6: SINGLE CHANNEL MODEL GEOMETRIC THERMAL HYDRAULIC PROPERTIES SUMMARY	42
4.7: HEAT STRUCTURE RADIAL NODE LENGTHS	47
4.8: TWO CHANNEL MODEL GEOMETRIC THERMAL HYDRAULIC PROPERTIES SUMMARY	49
4.9: EIGHT CHANNEL MODEL GEOMETRIC THERMAL HYDRAULIC PROPERTIES SUMMARY	51
5.1: MCHFR COMPARISON FOR 1, 2, & 8 CHANNEL MODEL.....	59
5.2: MCHFR COMPARISON FOR 1, 2, & 8 CHANNEL MODEL.....	63
6.1: POWER TRACE RESULTS INITIAL CONDITIONS	69
6.2: MAXIMUM FUEL TEMPERATURE COMPARISON SUMMARY.....	72
A.1: STEADY STATE RESULTS OF OSU HEU BEGINNING OF LIFE NORMAL CORE.....	97
A.2: CALCULATED AND MEASURED FUEL TEMPERATURES, HEU BEGINNING OF LIFE CORE	102
A.3: STEADY STATE RESULTS OF OSU HEU MIDDLE OF LIFE NORMAL CORE	102
A.4: CALCULATED FUEL TEMP.'S AT POWERS IN THE HEU MIDDLE OF LIFE NORMAL CORE.....	105
A.5: CALCULATED FUEL TEMP.'S FOR POWERS IN THE HEU END OF LIFE NORMAL CORE	108
A.6: STEADY STATE RESULTS FOR LEU BEGINNING OF LIFE ICIT CORE AT 1.1 MW _{TH}	108
A.7: CALCULATED FUEL TEMP.'S FOR POWERS IN THE LEU BEGINNING OF LIFE ICIT CORE.....	111
A.8: STEADY STATE RESULTS FOR LEU MIDDLE OF LIFE ICIT CORE AT 1.1 MW _{TH}	112
A.9: CALCULATED FUEL TEMP.'S FOR POWERS IN THE LEU MIDDLE OF LIFE ICIT CORE.....	115
A.10: LEU END OF LIFE ICIT CORE AT 1.1 MW _{TH}	115
A.11: CALCULATED FUEL TEMP.'S FOR POWERS IN THE LEU END OF LIFE ICIT CORE	118
A.12: SUMMARY OF LEU BEGINNING OF LIFE ICIT CORE PULSE BEHAVIOR	128
A.13: SUMMARY OF LEU MOL ICIT PULSE BEHAVIOR	131
A.14: SUMMARY OF LEU END OF LIFE ICIT PULSE BEHAVIOR	134
B.1: SUMMARY OF FUEL FISSILE CHARACTERISTICS.....	139
B.2: U-235 DELAYED NEUTRON GROUP HALF-LIFE VALUES	140
B.3: U-235 DELAYED NEUTRON GROUP DECAY CONSTANT VALUES	140

LIST OF TABLES (Continued)

<u>Table</u>	<u>Page</u>
C.1: EQUIPMENT USED FOR TEMPERATURE MEASUREMENT	143
C.2: HARDWARE ACQUIRED FOR EXPERIMENTAL ASSEMBLY	143

Thermal Hydraulic Analysis of the Oregon State TRIGA[®] Reactor Using RELAP5-3D

1. INTRODUCTION

Oregon State University has recently conducted a complete core conversion analysis as part of the Reduced Enrichment for Research and Test Reactors (RERTR) program. In 1978, the international community established the RERTR program. The mission of the program is to develop substitute fuel of higher-density, low enriched uranium (LEU), which is not suitable for weapons [1]. During the program's existence, 44 research reactors have been converted from highly enriched uranium (HEU) to LEU fuels [2]. The Oregon State TRIGA[®] Reactor (OSTR) currently contains HEU fuel. Upon the completion of the core conversion project, all fuel elements in the OSTR will be converted from HEU to LEU. This nonproliferation project is scheduled for completion in September of 2008.

Safety analyses are a crucial part of the nuclear industry. Safety analyses are conducted by analyzing a reactor's characteristics under normal conditions as well as credible accident scenarios. As part of the core conversion analysis, the Nuclear Regulatory Commission (NRC) has required that a complete neutronic and thermal hydraulic analysis be conducted on the existing OSTR (HEU) and potential (LEU) core. These analyses include characteristics of the reactor under nominal operational conditions as well as credible contingency conditions. With regards to the thermal hydraulic analysis, the quantification of key system properties as identified below provide a thorough understanding of the OSTR under both nominal and contingent conditions.

1.1 Research Objective

The objective of this project is to conduct a thermal hydraulic investigation in support of the RERTR program. The thermal hydraulic characteristics in the OSTR are driven

by core power, local heat flux distributions, operating coolant temperatures, and core geometry. The goals of the thermal hydraulic analyses are to:

- Calculate natural circulation flow rates, coolant temperatures and fuel temperatures as a function of core power for both the current HEU and proposed LEU cores.
- For steady state and pulsed operation, calculate peak values of fuel temperature, cladding temperature, surface heat flux, as well as critical heat flux ratio (CHFR) and temperature profiles in the hot channel for both the HEU and LEU cores.
- Perform accident analyses for the accident scenarios identified in the OSTR Safety Analysis Report.

Specific focus during this investigation was directed toward the applicability of different methods for calculating critical heat flux (CHF) for TRIGA[®] reactor analyses by comparing the CHF from Groeneveld 1986 [3], 1995 [4], and 2006 [5] look up tables as well as the Bernath [6] and McAdams [7, 8] correlations. Methods for calculating TRIGA[®] pulse characteristics were also studied by comparing several explicit numerical solutions of the power transient to those calculated by RELAP5-3D. The result of these comparisons will produce a benchmark for standardizing thermal hydraulic analyses for TRIGA[®] reactors.

1.2 Analysis Assumptions

RELAP5-3D Version 2.4.2 is the code used for all computational modeling during the thermal hydraulic analysis. This is a lumped parameter code. A lumped parameter code is a simplified mathematical model where variables that are spatially distributed are represented as single scalars rather than vectors. As a result, the spatial resolution

of a lumped parameter code is limited however it is assumed that RELAP5-3D can sufficiently model the thermal hydraulic characteristics found in the OSTR. RELAP5-3D is implemented during this study in order to accurately capture the phenomena.

Form loss values in the OSTR cannot be definitively tabulated [9]. A study has recently been conducted by General Atomics on form loss; the results produced from this analysis are assumed to be the correct form losses associated with the OSTR [10]. It is particularly difficult to accurately model this under the operating conditions of the OSTR where a great deal of mixing (turbulent to laminar boundary layer mixing) occurs. The characteristics of form loss found in the OSTR are discussed further in Section 4.2.5.4.

The boundary conditions that are imposed on the physical system are critical to the results that the RELAP5-3D model produces. These boundary conditions include inlet bulk coolant temperature and the system absolute pressure. The inlet temperature is assumed to be equal to the coolant temperature technical specification limit of the OSTR while the pressure boundary condition assumes that the reactor operates at sea level atmospheric pressure along with a fixed water column height defined above the core.

A power boundary condition is imposed on the fuel elements modeled in RELAP5-3D. This power does not take into account thermal hydraulic feedback including moderator temperature and void reactivity coefficient as it is assumed that the OSTR is operated at its technical specifications limit, a constant power of $1.1 \text{ MW}_{\text{th}}$ steady state. Under pulse operation the moderator temperature and void coefficient are not taken into account in the power boundary condition that is input in the RELAP5-3D deck, but the prompt fuel temperature feedback is. These feedback mechanisms were neglected in the pulse simulation due to this transient's extremely short time frame. It is assumed that the fuel is adiabatic; therefore no heat is dissipated into the moderator.

This power boundary condition was constructed using a point reactor kinetics model given the OSTR fissile fuel characteristics.

The thermal hydraulic hot channel is assumed to be the channel with the smallest coolant flow area. This assumption yields the most conservative results (i.e. CHF, coolant exit temperature, etc.) provided the fuel element with the largest thermal power production is assumed to be located in this subchannel.

The applicability of the forced convection CHF correlations that were implemented during the analysis is assumed to be valid. Although the OSTR operates under natural convection conditions, two forced convection CHF correlations were chosen as part of the final results. The two forced convection correlations considered were developed experimentally under similar conditions as the OSTR's operational environment.

1.3 Analysis Limitations

By using a single computational program (RELAP5-3D) the study is limited to the number of thermal hydraulic correlations used within the code itself. When referring to the heat transfer coefficient, RELAP5-3D uses many correlations for the single phase regime; when in the subcooled nucleate boiling regime, RELAP5-3D uses the Chen [11] and Bergles-Rohsenow [12] Correlations. These correlations are widely used within industry [11]; the Chen Correlation produces the heat transfer coefficient that is subsequently used in the critical heat flux calculations during this analysis. The Bergles-Rohsenow Correlation, although having a larger associated error, typically produces values that are conservative to the Chen Correlation.

RELAP5-3D does not incorporate the onset of nucleate boiling specifically by using the Davis-Anderson [13] Correlation, but uses the Churchill-Chu [14] or McAdams [15] Correlations; the Davis-Anderson Correlation is more suitable for the OSTR geometry.

Because RELAP5-3D is a lumped parameter code, it is limited to the phenomena that are identified in its numerical solution. The limit to discretizing the model in RELAP5-3D prevents identification of properties that may be inherent to small thermal hydraulic systems such as the OSTR. For example, the OSTR's design promotes subchannel mixing in the lower region of the core; results that verify this mixing can not be produced accurately without implementing a CFD code.

The results of the thermal hydraulic analysis conducted as part of the core conversion project for the OSTR is limited to the OSTR. The technical specifications identified for the OSTR are unique from those of all other TRIGA[®] reactors.

1.4 Overview of Following Chapters

In chapter two, the results of a literature review will be presented providing a general understanding of past thermal hydraulics analyses conducted on TRIGA[®] reactors. A discussion of the implementation of RELAP5-3D during reactor analyses is also presented, followed by an overview of typical CHF correlations that have been implemented in similar reactor analyses.

In chapter three, a comprehensive description of the OSTR is presented and its relation to the one, two, and eight channel RELAP5-3D models developed for this analysis.

Chapter four presents a thorough report of the discretization of the single, two and eight channel RELAP5-3D models that were developed for this study.

The steady state thermal hydraulic results for the one, two, and eight channel model are presented in chapter five. These results include those outlined in Section 1.1 as well as a quantitative comparison of hot channel axial mass flux, axial equilibrium quality, and axial bulk coolant temperature distribution and how these parameters impact the CHF distribution.

The pulse results are presented in chapter six. These results include those computations identified in Section 1.1 as well as a quantitative comparison of several different methods for calculating the pulse characteristics for the OSTR.

2. SURVEY OF LITERATURE

2.1 Previous TRIGA[®] Reactor Thermal Hydraulic Analyses

Thermal hydraulic analyses are frequently performed on TRIGA[®] reactors. Studies are conducted in order to change core configurations, change fuel, or for conducting particular in-core experiments. Many thermal hydraulic codes have been implemented for conducting these types of analyses including but not limited to; ATHLET, CATHARE, 3D COBRA, COBRA IIIC, COBRA, NCTRIGA, PARET, RETRAN, RELAP, RELAP5, RELAP5-3D, NATCON, and PLTEMP [9, 16-18].

The objectives during recent studies conducted on TRIGA[®] reactors have been directed toward characterizing subcooled flow instability [19], parameterizing features of the TRIGA[®] Mark II including grid plate form losses and fuel element flux profiles [20], benchmarking coupled kinetic/thermal-hydraulic TRIGA[®] experiments [9], and design and safety parameter studies on the TRIGA[®] Mark II [21]. Similar difficulties arise during these studies when trying to quantify form losses, subchannel pressure drop, and subchannel coolant mixing.

2.2 Previous RELAP5-3D Thermal Hydraulic Analyses

RELAP5-3D, developed by Idaho National Laboratory (INL) is a best-estimate transient simulation code of light water reactor coolant systems during postulated accidents [22]. RELAP5-3D is one the most widely used thermal hydraulic analysis validated codes implemented in the nuclear industry today [18]. Typically, RELAP5-3D is used on a system scale when conducting reactor thermal hydraulic analyses, with COBRA utilized for subsequent subchannel analyses.

In recent development, INL has focused on implementing a more refined flow regime map in its newest release of RELAP. Due to these extensive efforts, RELAP5-3D has the most developed flow regime map of any public thermal hydraulic code in the world. As a result, extensive validation and assessment work has been performed involving power reactors at operating conditions as well as research reactors [23]. This validation has resulted in RELAP5-3D becoming the general benchmark for thermal hydraulic safety analyses of all reactor types.

2.3 Previous CHF Studies Relevant to the OSTR Thermal Hydraulic Analysis

One of the earliest referenced studies on boiling dates back as far back as 1756 when a German physicist, Johann Leidenfrost, published a manuscript describing the insulating vapor layer in water caused by rapid boiling [7]. Since this publication, studies have been conducted regarding pool boiling, natural convection boiling, and forced convection boiling under a countless number of boundary conditions. Within the past century, the theoretical and experimental focus has been directed toward the maximum evaporation rate of a given fluid under specified conditions and how this rate can be quantified.

The critical heat flux is the maximum heat flux a saturated fluid can absorb before acquiring more enthalpy than can be dissipated into its surroundings. Therefore the given conditions influence a fluid to undergo the process of departure from nucleate boiling (DNB). Recently, significant error reduction in CHF correlations has been the focus of many research studies in order to reduce the uncertainty margin applied when conducting safety analyses on thermal hydraulic systems, including reactors.

2.3.1 Pool Boiling

Heat transfer from a heated surface to liquid is done through several mechanisms during nucleate pool boiling as stated in Tong and Tang [11]:

- Heat transport by the latent heat of bubbles.

- Heat transport by continuous evaporation at the root of the bubble and condensation at the top of the bubble, while the bubble is still attached to the wall.
- Heat transfer by liquid-vapor exchange caused by bubble agitation of boundary layer.
- Heat transfer by single-phase convection between patches of bubbles.

Pool boiling has been studied rigorously. Some of the more significant theoretical and experimental researchers in the field of pool boiling include Lang [24], Nukiyama [25], Bonilla and Perry [26], Cichelli and Bonilla [27], Kutateladze [28, 29], Rohsenow and Griffith [30], Zuber [31], Costello and Frea [32], Gaertner [33, 34], Katto and Yokoya [35], Lienhard and Dhir [36], Haramura and Katto [37], Liaw and Dhir [38], Ramilison and Lienhard [39], Elkassabgi and Lienhard [40], Dhir and Liaw [41], Sakurai and Shiotsu [42]. The primary focus in the past regarding pool boiling has been directed toward experimental data collection in order to validate correlations and develop more refined data banks with reference to CHF under altered conditions.

Many of the theoretical studies, including Katto [37], Lienhard and Dhir [36], numerically correlate empirical data by applying corrective factors to more accurately model the enhancement of CHF under the appropriate working conditions. Although many of these early investigators reported CHF data, the majority of their models were much more conservative than that found in empirical data and had large associated error with them.

Three particular investigators specifically pursued the study of water as their working fluid when investigating a numerical correlation using existing experimental data banks; the error associated with this data when implementing the Kutateladze Correlation is [43]:

- Sakurai and Shiotsu [42]: 33.94 %

- Bonilla and Perry [26]: 46.60 %
- Lienhard and Dhir [36]: 88.78 %

After reviewing the existing models for pool boiling CHF, a need for contact angle, surface orientation, and subcooling effects in modelling is identified. There are several existing theoretical pool boiling correlations that implement these parameters into their calculation of CHF which greatly reduce the error associated with their prediction of DNB occurring under pool boiling conditions. Because RELAP5-3D does not produce information regarding bubble contact angle, these correlations can not be implemented into the analysis. Therefore, because the correlations that are able to be implemented by referring to the results produced from the RELAP5-3D models during this study have such large error associated with them, no pool boiling CHF correlations will be used for this study.

2.3.2 Natural Convection Boiling

The CHF phenomenon at low flow conditions is more complicated to predict than forced convection due to the effects of buoyancy and flow instabilities [44]. For CHF during natural convective boiling in vertical channels, many studies have been conducted for water and refrigerants under a broad range of pressures and a number of empirical CHF correlations have been reported in literature. Katto and Kawamura [45], Monde and Yamaji [46], and Monde and Mitsutake [47] conducted many experiments and proposed some empirical correlations for vertical round tubes. Katto [48], Unal et al. [49], Vishner [50], Fujita et al. [51], Xia et al. [52], and Monde et al. [53] carried out various experiments and proposed many empirical correlations for vertical channels including annular tubes, rectangular channels and vertical tube bundles. Chyu [54], Henry and Fauske [55], and Liu and Chen [56] performed theoretical analyses and experiments for predicting CHF in similar geometric configurations.

Nearly all of the correlations and studies regarding natural convection mentioned above produce results that are within the error that is expected to be found in this study, when they are used within the conditions that they were developed under. The OSTR is a research reactor that has very high power densities and gradients. Because these natural circulation models have been developed under low flow, low power density, and low pressure conditions they are not directly applicable to this study.

2.3.3 Forced Convection Boiling

Although a large number of CHF correlations are available for heated rods, most of these correlations are inappropriate in their prediction of CHF under low flow conditions because they were developed based primarily on high flow CHF data. However there are CHF data correlations available that are reliable and applicable to the low flow and intermediate pressure conditions.

It is very important to be selective of the CHF method that is being implemented during a given analysis because the effect of mass flux on the CHF is relatively large at low pressure conditions [44]. This is also the case for equilibrium quality or the working fluid's enthalpy. These properties are position dependent and are two of several state parameters that are used to predict CHF.

In 2005, Moon et al. [44] compared CHF correlations at low flow conditions in non-uniformly heated vertical rods. The study examined four correlations; the 1995 CHF look-up tables [4], EPRI [57] rod bundle correlation, Macbeth [58] correlation, and the KAERI correlation [44]. For CHF analyses within system codes and subchannel codes, it is important to predict the local CHF value using local conditions such as local quality. Since the look-up tables, EPRI and Macbeth correlations are based on local conditions, they can predict the CHF occurrence location and the local CHF value. From these three correlations, Moon et al. study showed that the look-up table and KAERI correlation predicts the average CHF reasonably well relative to other

forced convection correlations given the present data. From this study it is recommended to use the look-up tables and Macbeth correlation because they underestimate slightly the local CHF while the KAERI correlation overestimates slightly the average CHF.

Lee et al. [59] used the Macbeth [60] CHF correlation to estimate the safety margin of the Korean Standard Nuclear Power Plant; the justification for using this correlation in the analysis is that it is conservative relative to other accepted CHF correlations such as the Biasi [61] Correlation and the 1986 AECL-UO [3] CHF look-up tables [44]. The Macbeth correlation is not typically implemented under natural convection conditions. Although the 1986 AECL-UO CHF look-up tables do not prove to be the most conservative CHF method, they were at the time of their origination the most consistent with experimental observations. The 1986 tables spurred D.C. Groeneveld to continue and refine his CHF prediction method, resulting in updated tables being published in 1995 [4] and then again in 2006 [5]. These tables have become a general benchmark for most thermal hydraulic applications regarding CHF predictions within the conditions they bound. A summary of the Groeneveld bounding conditions is shown in Table 2.1.

Table 2.1: Summary of CHF look-up Tables Bounding Conditions

Summary of CHF Look-up Tables Bounding Conditions			
look-up Table	1986	1995	2006
Min. Pressure [kPa]	100.0	100.0	100.0
Max. Pressure [kPa]	20000.0	20000.0	21000.0
Min. Mass Flux [$\text{kg/m}^2\text{-s}$]	0.0	0.0	0.0
Max. Mass Flux [$\text{kg/m}^2\text{-s}$]	7500.0	8000.0	8000.0
Avg. Min. Quality	-0.5	-0.5	-0.5
Avg. Max Quality	0.9	1.0	1.0
Error* [%]	~33.47	~7.27	~5.81

General Atomics Corp. (GA) is the manufacturer of the OSTR. GA uses two specific correlations when conducting internal thermal hydraulic analyses on TRIGA[®]

* Error associated in region of concern during this study ($P \approx 2000$ [kPa], $G \approx 500$ [$\text{kg/m}^2\text{-s}$], $X_e \approx -0.2$)

reactors, the McAdams [7, 8] and Bernath [6] Correlations. Although these correlations were developed early in study when referring to CHF correlations, they generally produce very conservative results within the conditions that TRIGA[®] reactors operate under.

One of the first controlled investigations conducted on CHF under forced convection conditions was done by McAdams in 1949, he proposed the following correlation:

$$q_{cr} = A_{H.S.} (v)^{1/3} (400000 + 4800(T_{sat} - T_b)) \quad \text{Equation (2.1)}$$

Another study conducted by Bernath in 1961, produced the correlation seen below:

$$q_{cr} = h_{BO} (T_{w_{BO}} - T_b) \quad \text{Equation (2.2)}$$

$$h_{BO} = 10890 \left(\frac{D_h}{D_h + D_H} \right) + \Delta v \quad \text{Equation (2.3)}$$

$$\Delta = \begin{cases} \frac{48}{D_h^{0.6}} & \text{if } D_h \leq 0.1 \text{ ft} \\ \frac{10}{D_h} + 90 & \text{if } D_h \geq 0.1 \text{ ft} \end{cases} \quad \text{Equation (2.4)}$$

$$T_{w_{BO}} = 57 \ln(P_{abs}) - 54 \left(\frac{P_{abs}}{P_{abs} + 15} \right) - \frac{v}{4} \quad \text{Equation (2.5)}$$

The Bernath Correlation has been considered in several literature discussions as being more reliable, through consistency and relative associated error, than the McAdams Correlation.

Due to the significance of these two correlations along with the Groeneveld look-up tables (1986, 1995, 2006), these correlations will be quantitatively be compared during this analysis.

3. OREGON STATE TRIGA[®] REACTOR

3.1 OSTR Overview

The OSTR, which first went critical in 1976, is a Mark II TRIGA[®] reactor licensed for steady state operation up to 1.1 MW_{th} [62]. The Mark II is an open pool design and operates at atmospheric pressure. Its design allows for several unique capabilities, including pulse mode operation and in-core irradiation facilities. The OSTR's primary method for cooling is natural convection.

The core is centered near the bottom of the reactor pool, as seen in Figure 3.1. The top of the core is located approximately sixteen feet below the surface of the reactor pool. The OSTR pool is approximately six and a half feet in diameter and twenty feet deep [63]. The core is three and a half feet in diameter and two feet in height.

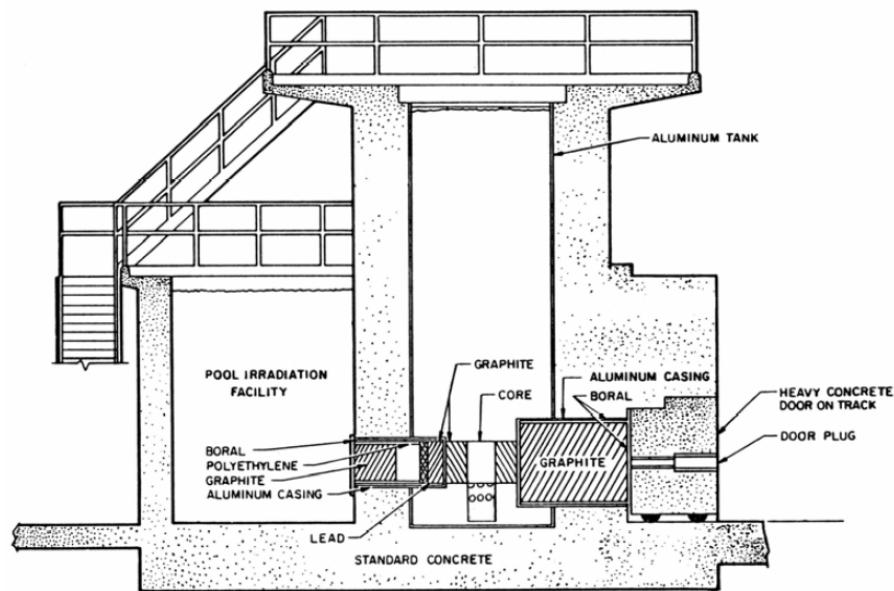


Figure 3.1: Vertical Sectional View of OSTR [62]

Figure 3.2 (a) and (b) are isometric rendered views of the OSTR. Figure 3.2 (c) gives a closer view of the reactor core providing identification to the location of control

elements, fuel elements, and upper and lower grid plate in the core. These figures are provided to give a comprehensive understanding of the entire OSTR and its core location within the reactor pool.

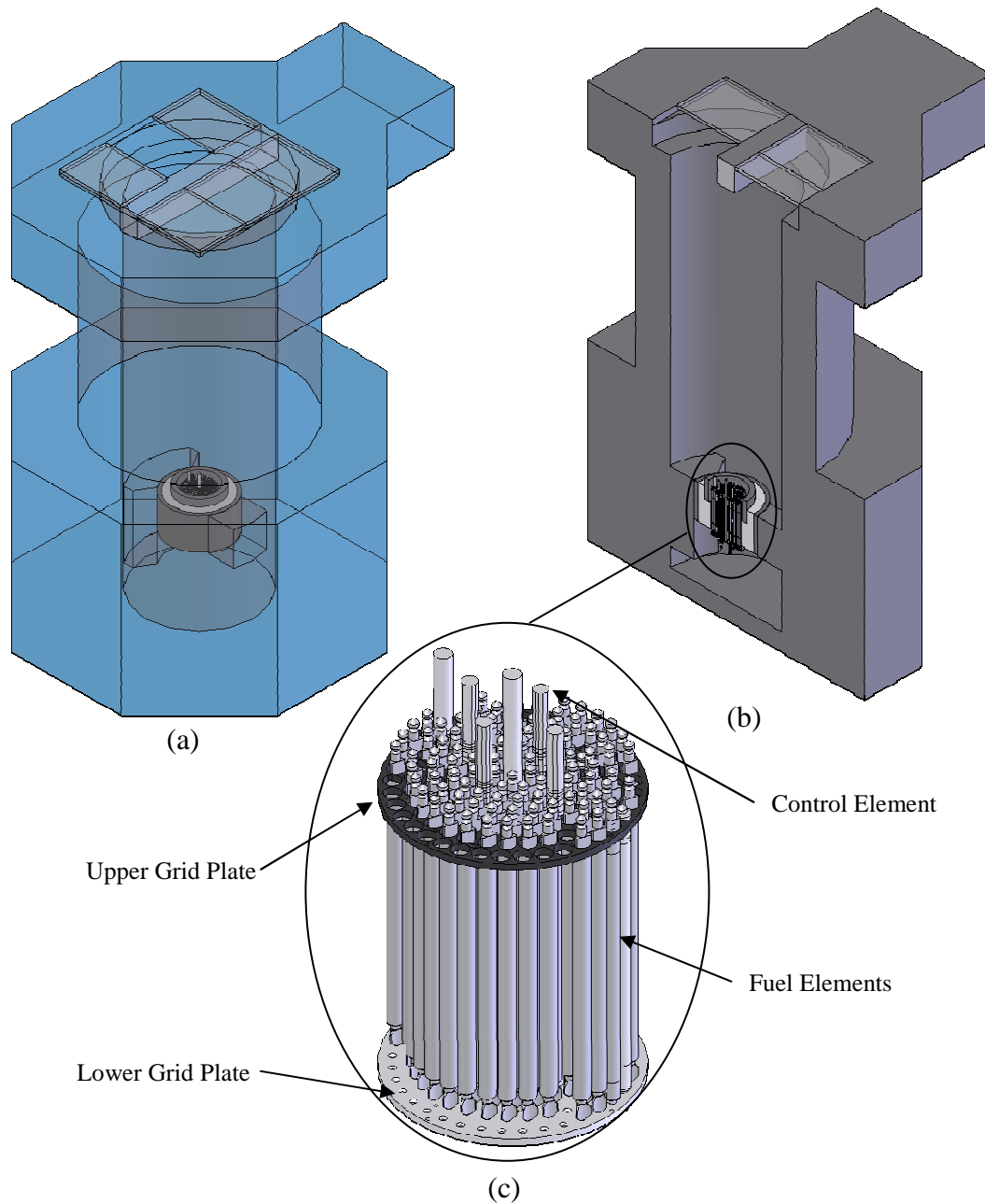


Figure 3.2: Isometric and Sectional Isometric View of the OSTR

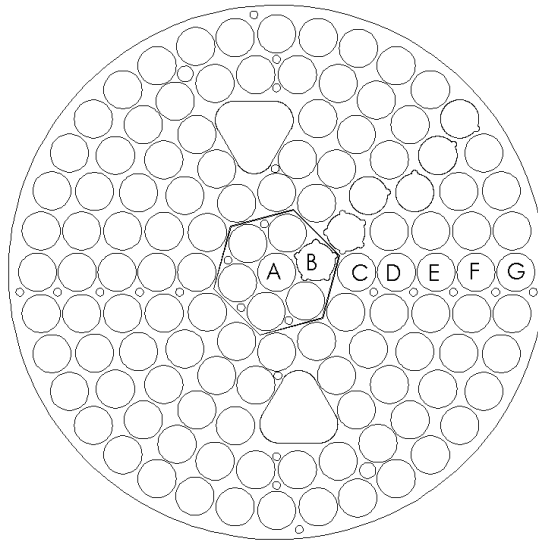


Figure 3.3: Top View of Upper Grid Plate in OSTR [64]

Seven rings make up the circular fuel element lattice configuration for the OSTR identified as Rings A through G as seen in Figure 3.3. Rings A and B contain triangular subchannels, but while moving outward radially on the grid plate the subchannel configurations become distorted and difficult to identify by ring and must be identified individually. All fuel pin locations in the core contain the same pitch (0.040568 m) [64]. Due to the lattice geometry, the subchannels found in the coolant volume adjacent to the A and B ring have the smallest flow area.

3.2 HEU/LEU Core Components

Table 3.1 provides a description of the components found in both the HEU and LEU cores.

Table 3.1: Core Components for HEU FLIP and LEU 30/20 Cores [65]

Core Configuration	HEU FLIP	LEU 30/20
Standard Fuel Elements	81	84
Instrumented Fuel Assemblies	1	1
Fuel-Followed Control Rod	3	3
Void-Followed Transient Rod	1	1
Aluminum Clad Reflector Elements	21	---
Stainless Steel Clad Reflector Elements	---	34

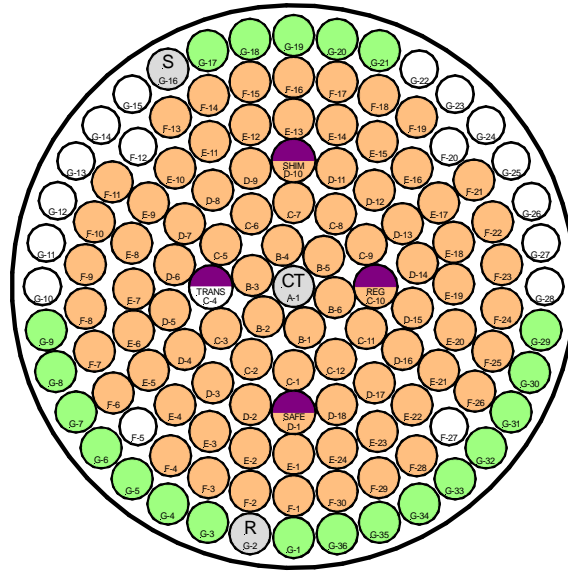


Figure 3.4: Schematic of the OSTR Core for the HEU Core in Normal Configuration [65]

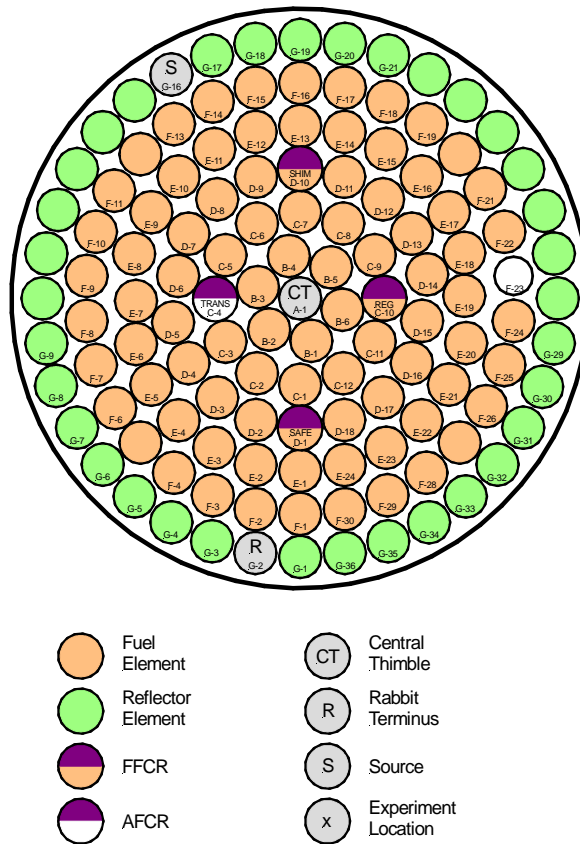


Figure 3.5: Schematic of the OSTR Core for the LEU Core in Normal Configuration [65]

Figure 3.4 and Figure 3.5 present the HEU Normal core configuration and LEU normal core configuration. The HEU core configuration contains Fuel Lifetime Improvement Plan (FLIP). FLIP fuel was developed by General Atomics in order to produce longer periods between required refueling. The number of fuel elements per ring as well as the arrangement of fuel elements within the integral core holds a significant impact on the results that are produced for the hot channel presented during this study.

There are four control rods in both the HEU FLIP and LEU 30/20 core. Three are fuel followed servo driven control rods and the fourth is a void followed hydraulic driven control rod commonly referred to as the “transient” rod. It is the fourth control rod that allows the OSTR to operate in pulse mode operation, and will be discussed later.

An exploded view of a single OSTR TRIGA[®] fuel element is presented in Figure 3.6 while a summary of both the HEU and projected LEU fuel design can be seen in Table 3.2. As seen in Table 3.2, the primary change during the core conversion project takes part within the fuel composition moving from 70% enriched and 1.6 % erbium content to 19.75 % enriched and 1.1 % erbium content. The fuel geometry is unchanged.

In 1976 General Atomics began investigating fuel compositions that allow the use of LEU to replace HEU fuels while maintaining long core life [66]. TRIGA[®] fuel composition and fission mechanisms will be discussed in Chapter 6.

Table 3.2: Comparison of HEU FLIP and LEU 30/20 Fuel Designs [65]

Fuel Type	HEU FLIP	LEU 30/20
Uranium content [mass %]	8.5	30
U-235 enrichment [mass % U]	70	19.75
Erbium content [mass %]	1.6	1.1
Fuel alloy inner diameter [mm]	6.35	6.35
Fuel alloy outer diameter [mm]	36.449	36.449
Fuel alloy length [mm]	381	381
Cladding material	Type 304 SS	Type 304 SS
Cladding thickness [mm]	0.508	0.508
Cladding outer diameter [mm]	37.465	37.465

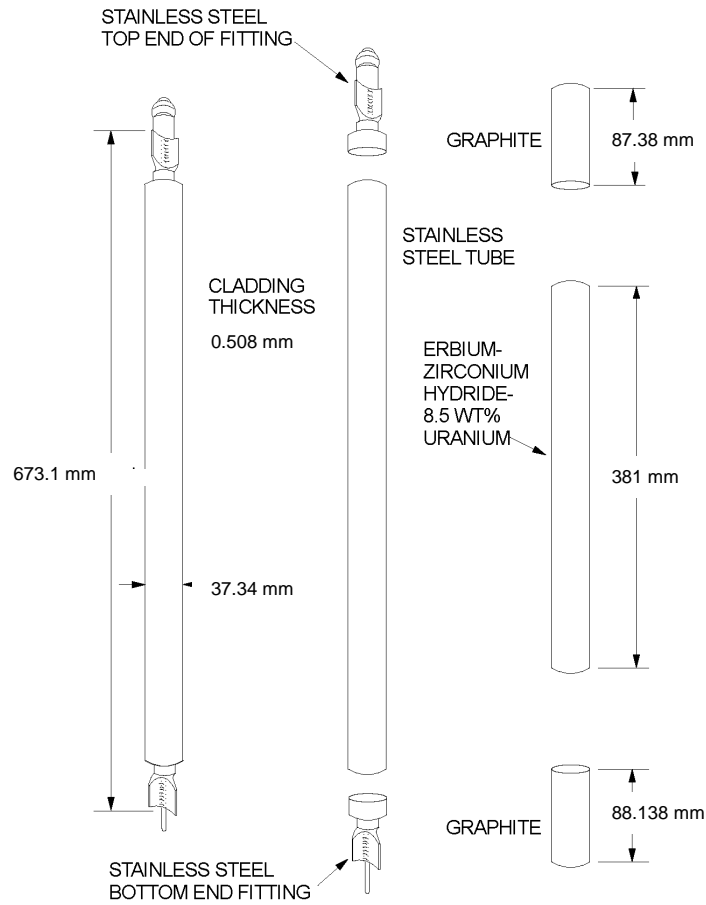


Figure 3.6: TRIGA^(R) Fuel Element Design Utilized in the OSTR Core [65]

The thermal hydraulic portion of the OSTR core conversion study required fuel element power values as well as hot channel intra-fuel rod power distributions in order to quantify the appropriate hot channel thermal hydraulic properties. MCNP5 was used to compute the relative contribution of each fuel element to the overall core power; Figure 3.7 and Figure 3.8 present these results. These diagrams present each fuel element's power contributed within a given core configuration as part of the integral core power ($1.1 \text{ MW}_{\text{th}}$).

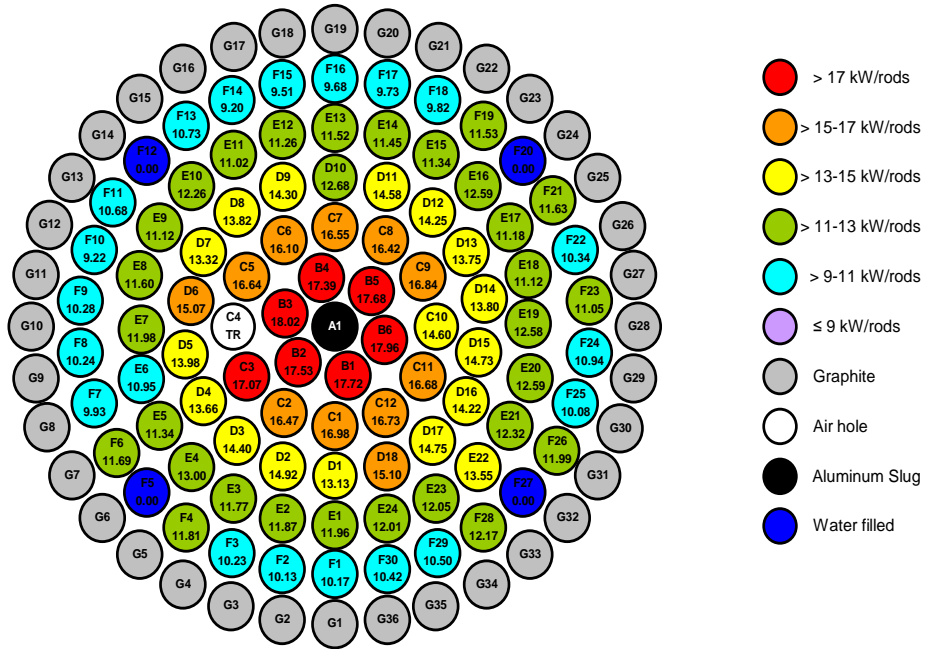


Figure 3.7: Core Power Distribution (HEU BOL Normal Core) [65]

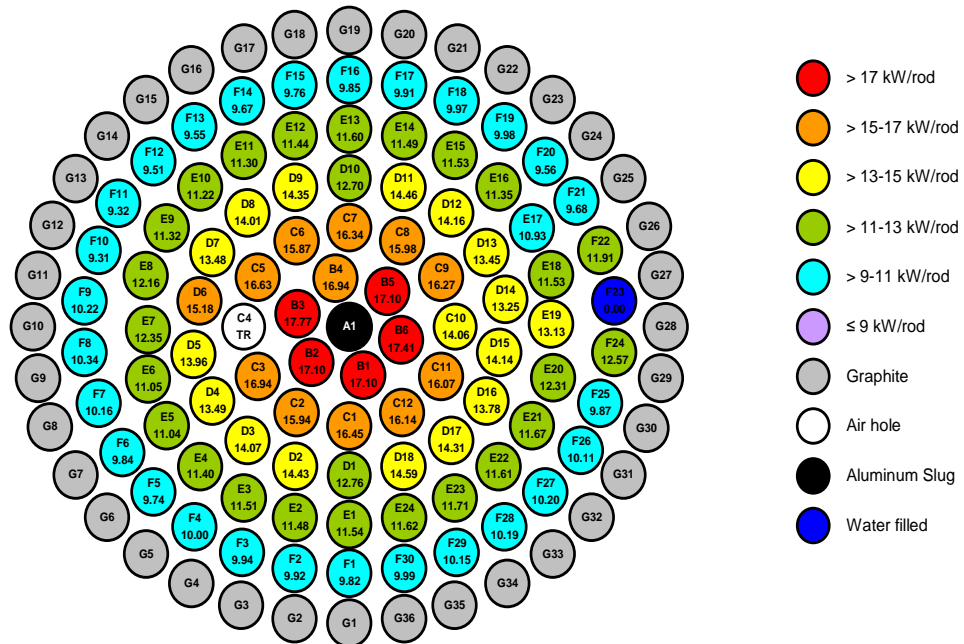


Figure 3.8: Core Power Distribution (LEU BOL Normal Core) [65]

The hottest fuel element (largest thermal power production) within the core provides the most limiting conditions for the thermal hydraulic study in each core configuration. This takes place in the B3 location (B Ring, number 3 fuel element) for both the HEU Beginning of Life (BOL) and LEU BOL Normal Core.

The location of the hot channel within the core is as one would expect, next to the void followed transient rod where the highest fission rate occurs. The burn-up rate in the fuel elements surrounding the transient rod is increased for several reasons. The transient rod is located near the center of the core therefore the relative flux at this location is larger than would be found farther away from the center. The transient rod is not fuel followed; therefore when it is adjusted such that it is partially removed from the core in order to maintain reactor steady state, no element takes its vacant place. As a result of this vacant location within the core, the fuel elements that surround the transient rod are exposed to a larger solid angle potential of fission neutrons than if there were an element in this location. This phenomenon is called shadowing, where a key element blocks surrounding elements from potential neutrons.

Figure 3.9 and Figure 3.10 display the intra-fuel power distribution for the HEU BOL and LEU BOL Normal Cores in the hot channel fuel element. Referring to Figure 3.9, moving from left to right one can view the radial power distribution in Watts, while moving from front to back the axial power distribution in Watts is presented. More fission occurs in the radial outer portion of the fuel element due to radial volume weighting (Equations (3.1) through (3.3)) and self moderation; while the axial power is contributed primarily in the axial center of the fuel element.

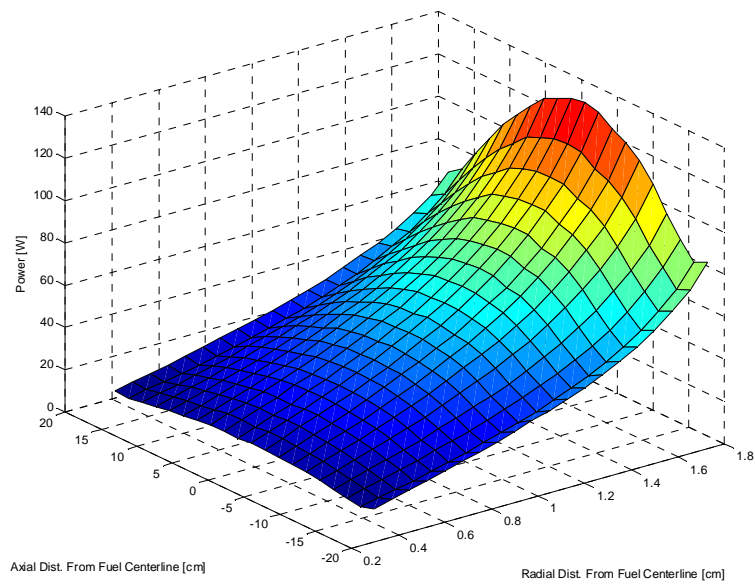


Figure 3.9: Hot Channel Fuel Power Distribution (HEU-BOL Normal Core)

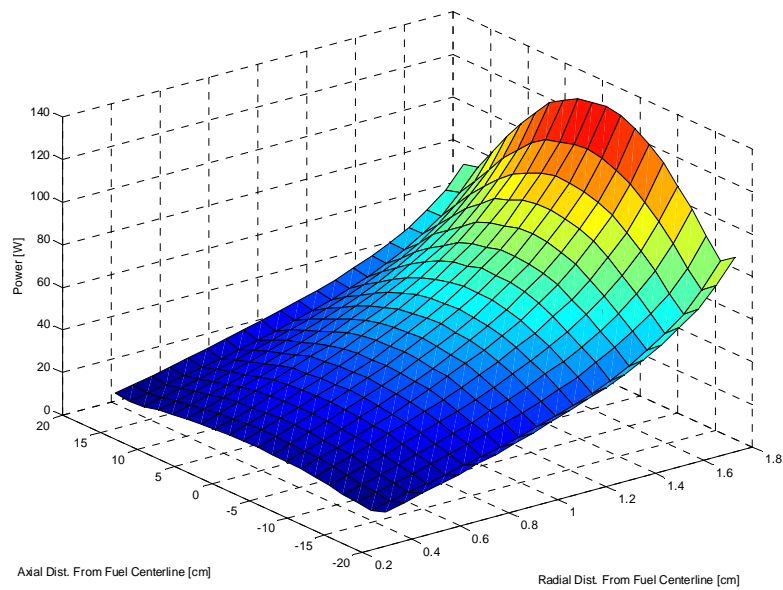


Figure 3.10: Hot Channel Fuel Power Distribution (LEU-BOL Normal Core)

In order to conduct the thermal hydraulic analysis using RELAP5-3D it is required to input fuel element or “heat structure” parameters. Rather than input the four hundred nodal power values presented in Figure 3.9 and Figure 3.10, RELAP5-3D requires that two normalized vectors be identified in its equivalent fuel element. These vectors are located in the radial and axial direction of the fuel element and can be seen for the HEU BOL and LEU BOL Normal Cores in Figure 3.11 and Figure 3.12; this will be discussed in further detail in the RELAP5-3D model description.

From Figure 3.11 it can be seen that the LEU BOL Normal Core radial power profile has a larger maximum power factor than that of the HEU BOL while the HEU BOL axial maximum power factor value bounds that of the LEU BOL; this is partially due to the change in erbium concentration from 1.1% to 1.6% in the LEU fuel, but primarily a product of the change in core configuration. It is important to note that the radial power shapes in Figure 3.11 are not representative of the input in the RELAP5-3D model. The power profile seen in Figure 3.11 is volume weighted in cylindrical coordinates, the numerical derivation for calculating the volume weighted radial fuel power is presented in Equations (3.1) through (3.4). RELAP5-3D requires that power densities be input in order to internally weight these power values by volume.

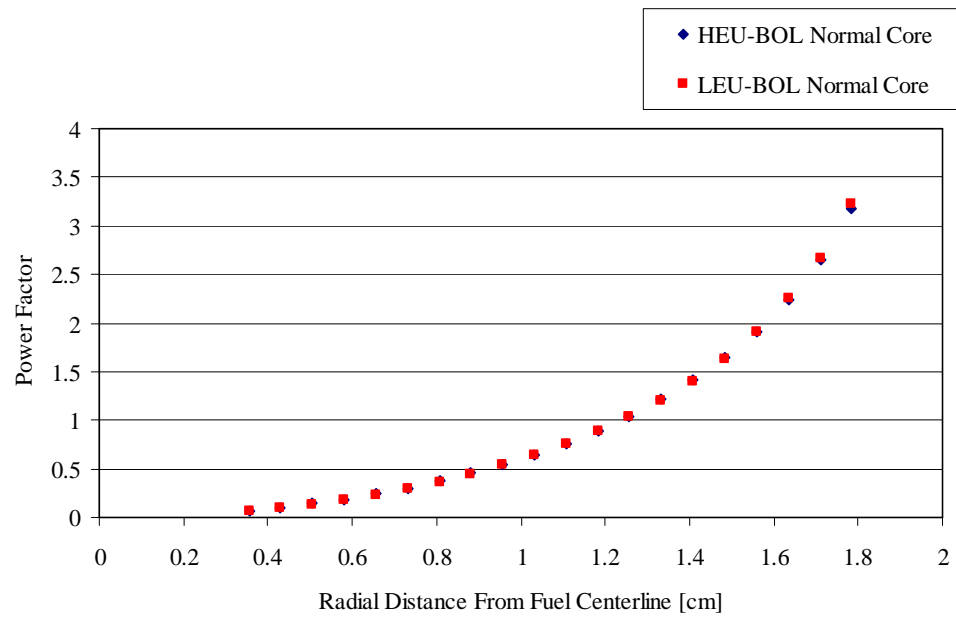


Figure 3.11: Hot Channel Fuel Radial Power Factor Profile

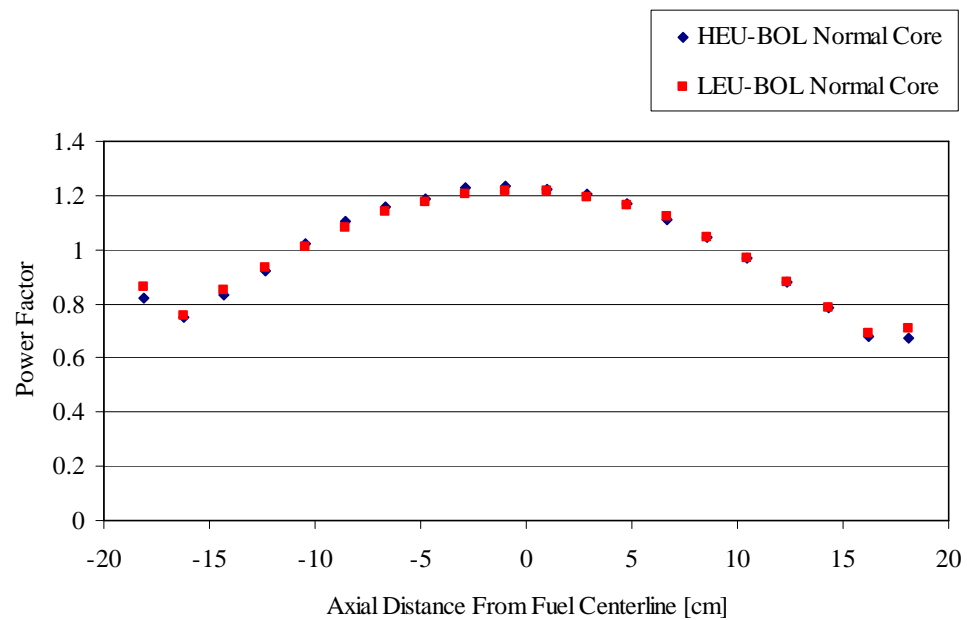


Figure 3.12: Hot Channel Fuel Axial Power Factor Profile

Table 3.3: Hot Channel Power Summary

Hot Channel Power Summary						
	Hot Channel Location	Hot Channel Thermal Power [kW]	Hot Channel Peak Factor $[P_{max}/P_{avg}]$	Hot Channel Fuel Axial Peak Factor $[P_{max}/P_{avg}]$	Hot Channel Fuel Radial Peak Factor $[P_{max}/P_{avg}]$	Effective Hot Channel Peak Factor $[P_{max}/P_{avg}]$
HEU-BOL Normal Core	B3	18.02	1.442	1.236	1.907	3.399
HEU-MOL Normal Core	B6	18.37	1.420	1.209	1.518	2.606
HEU-EOL Normal Core	B6	16.48	1.273	1.234	1.708	2.683
LEU-BOL ICIT Core	B6	18.47	1.477	1.221	1.963	3.540
LEU-BOL CLICIT Core	B3	17.03	1.362	1.221	1.943	3.231
LEU-BOL Normal Core	B3	17.77	1.422	1.219	1.945	3.371
LEU-MOL ICIT Core	B6	18.52	1.482	1.225	1.846	3.351
LEU-MOL CLICIT Core	B3	17.03	1.363	1.225	1.821	3.040
LEU-MOL Normal Core	B3	17.80	1.424	1.222	1.823	3.172
LEU-EOL ICIT Core	B6	17.61	1.409	1.181	1.699	2.827
LEU-EOL CLICIT Core	C7	16.35	1.308	1.212	1.732	2.746
LEU-EOL Normal Core	B3	17.02	1.362	1.178	1.707	2.739

For the core conversion project thermal hydraulic analysis it is required that the most bounding (limiting) conditions of the current (HEU) and proposed (LEU) cores be identified. The most limiting condition for the hot channel thermal power output can generally be summed up as the “Effective Hot Channel Peak Factor” presented in Table 3.3. The Effective Hot Channel Peak Factor is the product of the Hot Channel Peak Factor, Hot Channel Fuel Axial Peak Factor, and Hot Channel Fuel Radial Peak Factor.

The hot channel thermal power, axial and radial power profiles were obtained from the MCNP5 analysis. The hot channel power factor was obtained by taking the ratio of the hottest fuel element thermal power to the average fuel element thermal power in each core configuration. It is important to note that the hot channel thermal power found in Table 3.3 represents the thermal power after applying the hot channel peak factor. Similarly the axial peak factor was obtained from referring to the axial power distribution procured from the MCNP5 analysis by taking the ratio of the hottest axial nodalized thermal power value to the average axial nodalized thermal power value. The radial peak factor was calculated by normalizing the thermal power in cylindrical coordinates as follows; all three power profiles are graphically presented below in Figure 3.13.

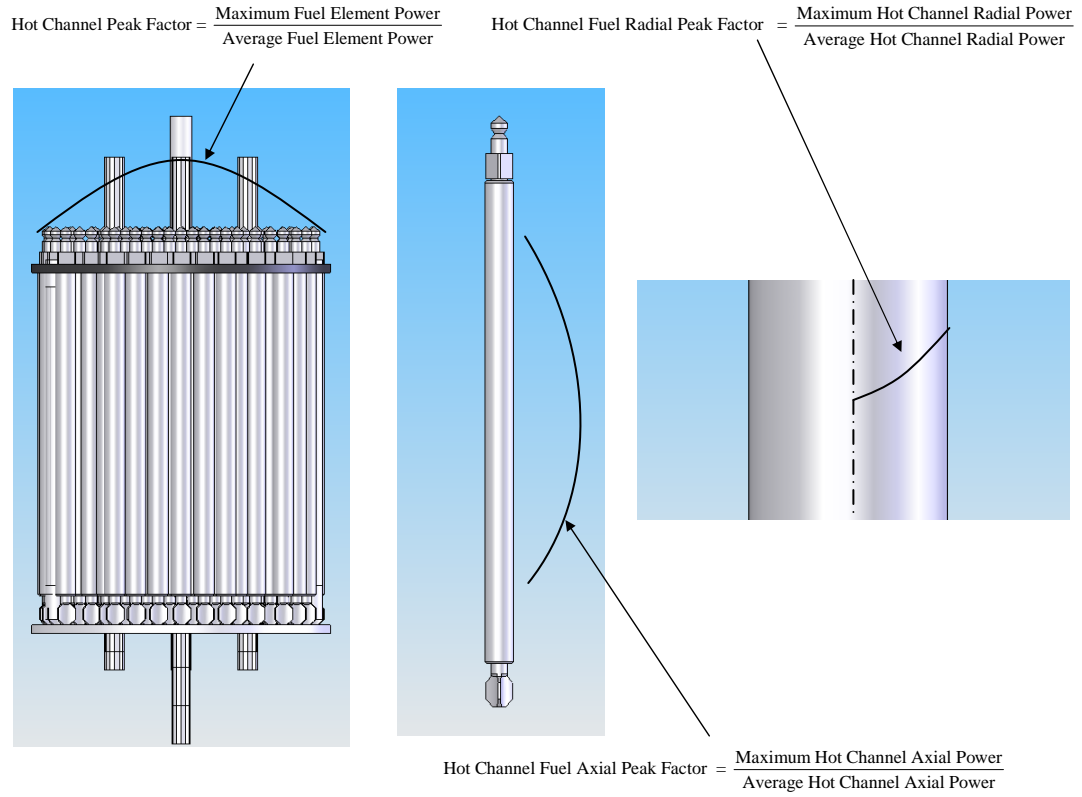


Figure 3.13 Core Power, Fuel Element Axial Power, Fuel Element Radial Power Profile

Consider the fission rate in a fuel element as $f(r,z)$, which is defined in cylindrical coordinates. The spatially average value of $f(r,z)$ at some given axial position (z_o) is given as:

$$\bar{f}(r, z_o) = \frac{2\pi \int f(r, z_o) r dr}{2\pi \int r dr} \quad \text{Equation (3.1)}$$

Where the integral ranges over the radial region of interest and 2π represents the azimuthal dependence of the function.

Now consider if $f(r,z)$ is to be discretized at some given axial location z_o . It can be done in a way that preserves the integral of $f(r, z_o)$ as follows:

$$f(r_i, z_o) = \frac{\int_{r_i}^{r_{i+1}} f(r_i, z_o) r dr}{\int_{r_i}^{r_{i+1}} r dr} \quad \text{Equation (3.2)}$$

In the case of a discretized function $f(r_i, z_o)$, we can change the discretized scheme by converting the integral in the numerator to a summation:

$$f(r_i, z_o) = \frac{\sum_i f(r_i, z_o) \pi(r_{i+1}^2 - r_i^2)}{\pi(r_{n+1}^2 - r_n^2)} \quad \text{Equation (3.3)}$$

Where the r_n and r_{n+1} correspond to the transformed nodal discretization and the summation runs over all cells (full or partial) that exist in the original discretization. In the case of a partial cell, only that portion that lies within the transformed nodal space is considered. Twenty radial nodal locations were defined within the fuel meat when calculating the radial peak factor. The radial peak factor was calculated using the methodology found in Equations (3.1) through (3.3) and applying them to Equation (3.4).

$$PF(z_o) = \frac{f(r, z_o)_{\max}}{f(r, z_o)} \quad \text{Equation (3.4)}$$

4. DESCRIPTION OF THE RELAP5-3D MODELS

Three models have been developed in RELAP5-3D, a single (hot channel) model, a two channel model, and an eight channel model. The intent of developing multiple models is to compare thermal hydraulic characteristics that result from building a more economical, less discretized model (hot channel model) to that of a more refined model (eight channel model) as well as comparing the effects of cross flow associated with the multichannel RELAP5-3D models. By conducting this comparison the objective is to validate the single channel model through a conservatism approach to thermal hydraulic safety analysis.

4.1 Theoretical Justification for Single Channel Model

The most significant assumption made during the development of the RELAP5-3D model is that the OSTR core can be conservatively modeled as a single channel (hot channel). This assumption most importantly affects the CHF result and its conservatism relative to that produced in a more spatially refined model. A qualitative comparison of the thermal hydraulic parameters that characterize critical heat flux can be made by comparing an isolated subchannel to one in which the working fluid can communicate freely between multiple subchannels. This comparison is done by considering both models under similar conditions as the OSTR.

The hot channel (Figure 4.1 (a)) assumes a location within the core containing the highest power density. It also is assumed that the flow area in the hot channel is the smallest found in the core. As a result of these two assumptions it can be stated that, with no diffusion to the surrounding subchannels, the fluid exiting the hot channel will therefore contain the highest coolant temperature within the core.

Now considering the two channel model, as seen in Figure 4.1 (b), adjacent subchannels are open to one another through the gap between two neighboring fuel

elements. It is assumed that cross flow between these subchannels is present and the fluid in the secondary subchannel (subchannel 2) diffuses into the hot channel. The assumption can then be made that subchannel 2 contains the second highest power density found in the core while the hot channel still contains the highest power density. As a result of diffusion of the working fluid between the subchannels in Figure 4.1 (b) under natural circulation flow rates where both subchannels are assumed to have the same mass flux, it can then be stated that through the diffusion of subchannel 2 into subchannel 1 the exit bulk coolant temperature during cross flow must be less than that with no cross flow [11, 67]:

$$T_{1,bulk(no-crossflow)} \geq T_{1,bulk(crossflow)}$$

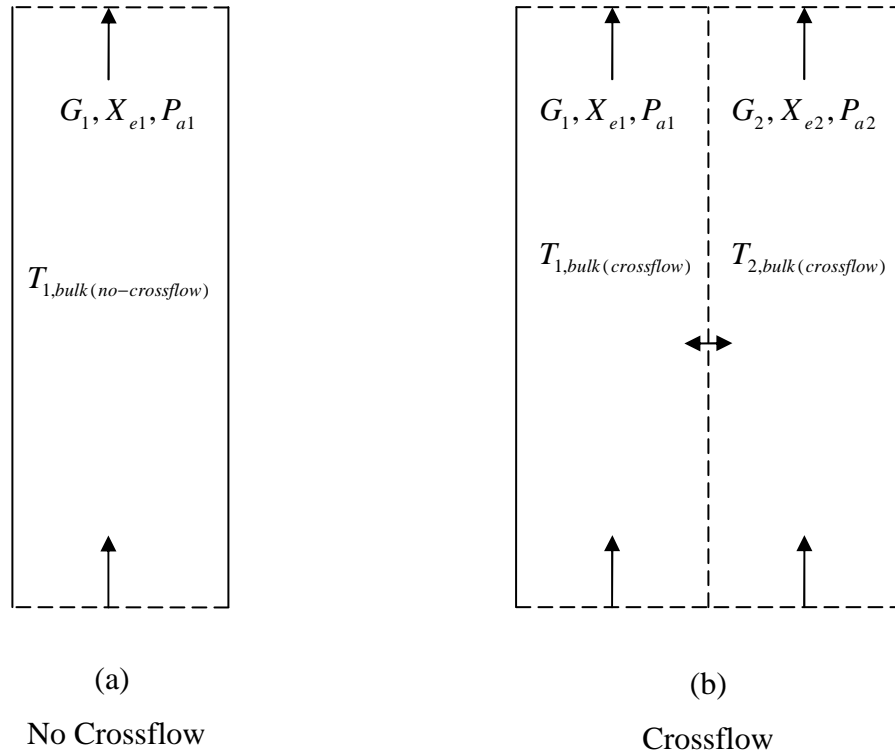


Figure 4.1: Subchannel comparison for cross flow justification

Six different critical heat flux methods are considered during this project as was discussed in Chapter 2:

- RELAP5-3D CHF
 - Adopted Groeneveld 1986 AECL-UO CHF
- Groeneveld 1986 AECL-UO CHF
- Groeneveld 1995 AECL-UO CHF
- Groeneveld 2006 AECL-UO CHF
- McAdams
- Bernath

All of these critical heat flux methods are primarily a function of three fluid parameters; mass flux (G), equilibrium quality (X_e), and absolute pressure (P_a) [3-5, 68]. If we make the assumption below, geometry and surface roughness are neglected when predicting CHF.

$$\text{CHF} = f(G, X_e, P_a)$$

The conservatism of the single channel model relative to a multi-channel model will be assessed by examining the relationship between bulk temperatures with and without cross flow. A subsequent comparison can then be made for each of these three independent fluid parameters that define the CHF.

The absolute pressure change due to the temperature difference between the single channel model and multi-channel model is not significant. This is because the absolute pressure is primarily dependent on the hydrostatic head that is created by the water column located above the core. It should be noted that near atmospheric pressure a one percent change in fluid temperature corresponds approximately a one percent change in pressure.

Equilibrium quality is defined as:

$$X_e = \frac{h - h_f}{h_{fg}}$$

Comparing equilibrium quality found at a given vertical location in the single channel model to that in a multi-channel model, from the definition of equilibrium quality, the single channel model will produce greater quality values. This greater equilibrium quality produces more conservative CHF values.

Comparing mass flux found at a given vertical location in the single channel model to that in a multi-channel model, as a result of an increase in equilibrium quality the mass flux in the will increase. This produces less conservative CHF values when with respect to an increase in mass flux.

Because equilibrium quality produces more conservative CHF values and mass flux produces less conservative CHF values in the single channel model a comparison can be made between the effect on CHF relative to a change in equilibrium quality versus a change in mass flux. By demonstrating that one of these two parameters more significantly affects the CHF it can then be stated whether a single channel model or multi-channel model produces more conservative results.

$$\frac{\partial(CHF)}{\partial(G)} \leftrightarrow \frac{\partial(CHF)}{\partial(X_e)}$$

This sensitivity study was conducted using mass flux range of 100 through 300 kg/m²sec, and an equilibrium quality of -0.2 through -0.1. These fluid property ranges correspond to the region in which the OSTR operates under at steady state. Figure 4.2 was created using the 2006 Groeneveld look-up tables as the subsequent benchmark

method for calculating critical heat flux dependence on a change in equilibrium quality and mass flux.

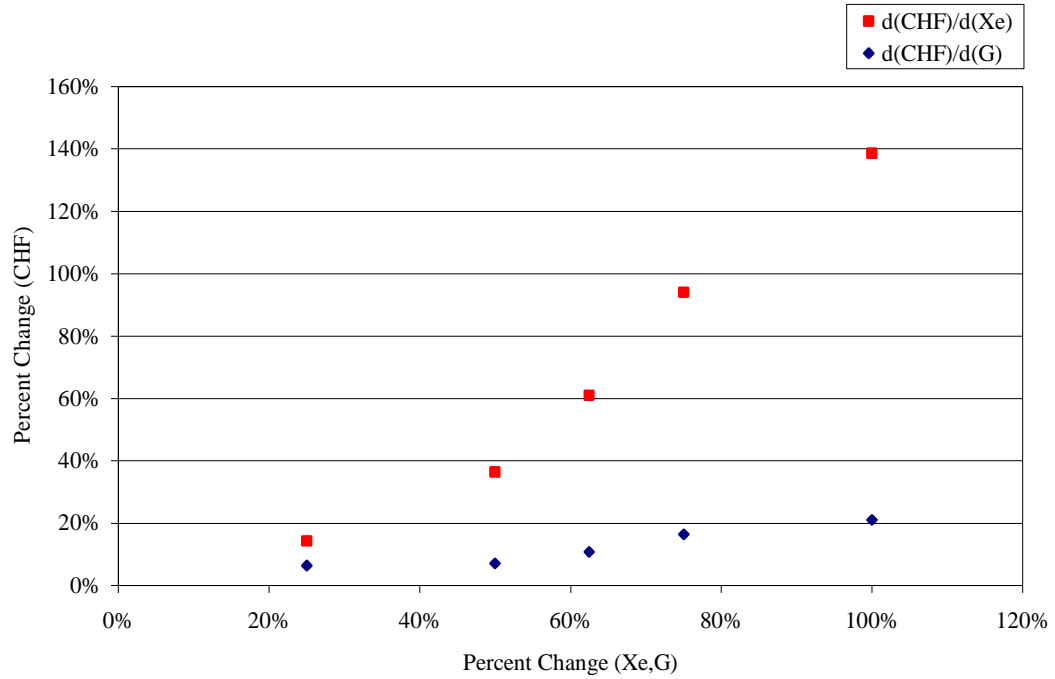


Figure 4.2: Equilibrium Quality to Mass Flux Sensitivity Comparison

Figure 4.2 represents the results produced during this comparison of CHF dependent properties. It can be seen from this figure that CHF is influenced much more by a change in equilibrium quality than by mass flux. The figure above provides evidence that a single channel model will more conservative results to that of a multi-channel model.

4.2 Single Channel Model Description

4.2.1 System

The RELAP5-3D model seen in Figure 4.3 consists of a coolant source, cold leg, horizontal connector, hot channel, and coolant sink. This model is representative of a single OSTR core hot channel.

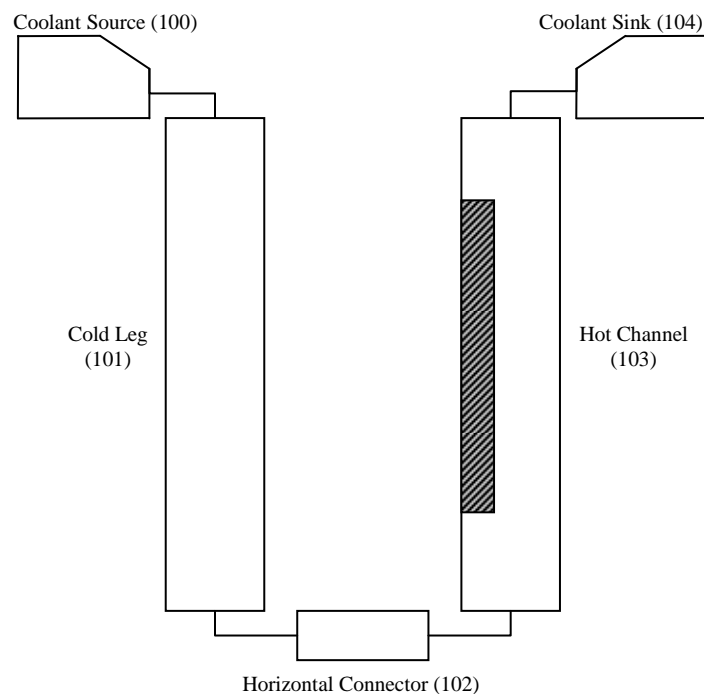


Figure 4.3: Single Channel RELAP5-3D Model Schematic

The coolant source is modeled as a time dependent volume in RELAP5-3D allowing for an inlet pressure and temperature boundary condition to be imposed on the system during the analysis. The cold leg is incorporated into the RELAP5-3D model in order to create a pressure differential between the cold coolant entering the subchannel and the heated coolant passing through the subchannel. This drives the natural circulation flow. The horizontal connector serves no physical purpose in the OSTR, but is rather a nonphysical connector between the cold leg and hot channel to allow for communication between Volumes 101 and 103 during the computational process.

The hot channel (Volume 103) is the volume which contains the fuel element of a single OSTR subchannel. In the RELAP5-3D model that the hot channel has the most conservative thermal hydraulic parameters found in the OSTR core and that it is located in the B Ring.

Referring to Figure 4.4, the 24 nodes that occupy the hot channel volume incorporate all geometric thermal hydraulic parameters into its axial nodalized locations. Node 01 represents the volume which is occupied by the lower grid plate in the OSTR. Node 02 denotes the lower reflector comprised of graphite material in the lower portion of the OSTR fuel element. Nodes 03 through 22 are comprised of the fissionable fuel element material (U-ZrH), and constitute the RELAP5-3 heat structure. In these 20 axial nodal locations a modified cosine axial heat distribution has been applied, based on the results produced from the MCNP5 model. Node 23 is the upper reflector, similar to the lower reflector it is also comprised of graphite. Node 24 is the upper grid plate location in the hot channel volume.

The coolant sink (Volume 104) exactly parallels the geometric input parameters in the coolant source (Volume 100) time dependent volume. These Volumes are incorporated in the RELAP5-3D model in order to impose boundary conditions on the subchannel.

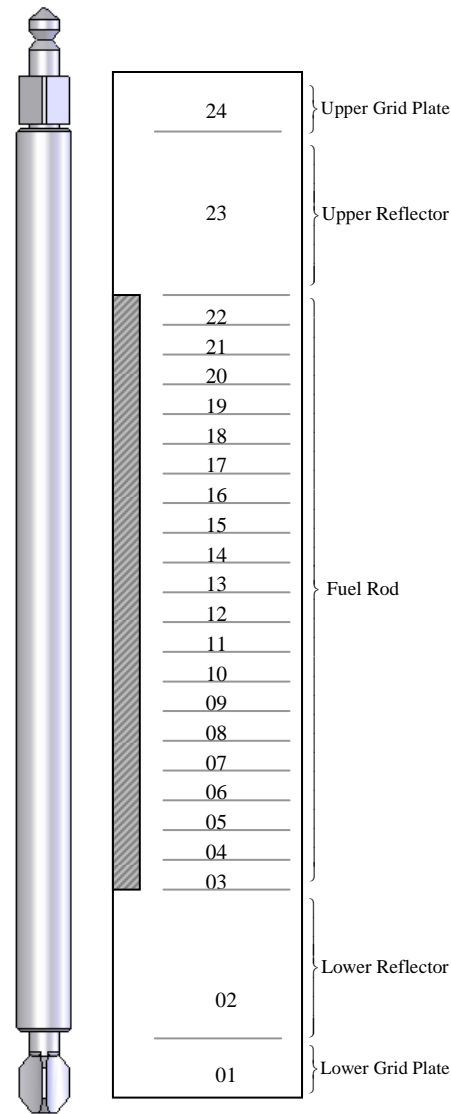


Figure 4.4: Comparison of OSTR Fuel Rod Axial Characteristics and RELAP subchannel

4.2.2 Coolant Source (100)

The coolant source models the coolant mass flux passing through the core hot channel in the OSTR. The coolant source is modeled in RELAP5-3D as a time dependent volume, which allows for temporal pressure and temperature boundary conditions to be imposed on the system. The coolant source is incorporated into the RELAP5-3D model for the sole purpose of implementing these two boundary conditions on the system.

By technical specifications the OSTR coolant may not exceed 49.0 °C (120.2 °F) in the reactor pool [69]. In order to force the maximum potential conservatism in the solution a bounding inlet temperature of 49.0 °C (120.2 °F) is used.

A constant pressure of $1.01 \cdot 10^5$ Pa (14.7 psia) is assumed to exist at the top of the reactor pool. The OSTR technical specification requires a minimum water column height above the top of the core to be 4.2672 m (168 inches or 14 feet), so this equivalent water column pressure boundary condition is used in the RELAP5-3D model for conservatism. RELAP5-3D requires that input pressure conditions be entered as absolute pressure, therefore the input RELAP5-3D pressure used in the model at the top of the core is $1.43 \cdot 10^5$ Pa (20.7717 psia). These boundary input parameters summarized in Table 4.1. The geometric parameters of the coolant source are summarized in Table 4.2.

Table 4.1: Time Dependent Volume Boundary Conditions

Time Dependent Volume 100 & 104 Boundary Conditions	
Description	Value
Pressure [Pa] (psia)	$1.43 \cdot 10^5$ (20.7717)
Temperature °C (°F)	49.0 (120.2)

Table 4.2: Volume 100 & 104 Geometric Parameters

Volume 100 & 104 Geometric Parameters	
Description	Value
Flow Area [m ²] (in ²)	1.0 (1550.0)
Length [m] (in)	1.0 (39.37)
Surface Roughness [m] (in)	0.0 (0.0)
Orientation	Horizontal
Friction Calculation	Not included in volume

4.2.3 Cold Leg (101)

The cold leg is geometrically congruent to the hot channel; it connects the coolant source to the horizontal connector volume. This volume is included into the RELAP5-3D model in order to allow for the boundary conditions imposed by the coolant source

to communicate correctly to the hot channel. The cold leg has the same height as the hot channel. This is important because it allows for an equilibration between the gravitational force imposed on the hot channel verses that imposed on the cold leg allowing for the sole method of cooling to be natural circulation. The geometric parameters of the cold leg volume are in summarized Table 4.3. For calculated justification of these values refer to Section 4.2.5.

Table 4.3: Volume 101 Geometric Parameters

Volume 101 Geometric Parameters	
Description	Value
Flow Area [m ²] (in ²)	$3.304 \cdot 10^{-4}$ (5.12)
Length [m] (in)	0.711 (28.0)
Surface Roughness [m] (in)	0.0 (0.0)
Orientation	Vertical
Friction Calculation	Not included in volume

4.2.4 Horizontal Connector (102)

The horizontal connector is a non-physical component of the OSTR and is simply incorporated into the RELAP5-3D model to allow for computational communication between Volume 101 and 103.

The horizontal connector is horizontally oriented, therefore no gravitational term is incorporated in the calculations within this volume, and thus it has no effect of the result produced in the hot channel. The geometric parameters for volume 102 are in Table 4.4. The flow area for the horizontal connector volume and cold leg volume do not affect the result produced in the hot channel, these volumes are input in the model to produce a pressure column of water that is equivalent to the hot channel pressure. This naturally imposes an equilibrium pressure boundary condition on the system. As a result of this boundary condition the only driving force for coolant flow through the hot channel is limited to natural circulation. All values in this volume are arbitrarily chosen.

Table 4.4: Volume 102 Geometric Parameters

Volume 102 Geometric Parameters	
Description	Value
Flow Area [m ²] (in ²)	1.0 (1550.0)
Length [m] (in)	1.0 (39.37)
Surface Roughness [m] (in)	0.0 (0.0)
Orientation	Horizontal
Friction Calculation	Not included in volume

4.2.5 Hot Channel (103)

4.2.5.1 Subchannel Flow Area

The B Ring pitch from fuel element centerline to centerline is 0.040568 meters, and it has a triangular subchannel geometry also containing the smallest subchannel flow area. It is for this reason that the subchannel flow area for the RELAP5-3D model is calculated with reference to the B Ring subchannel flow area.

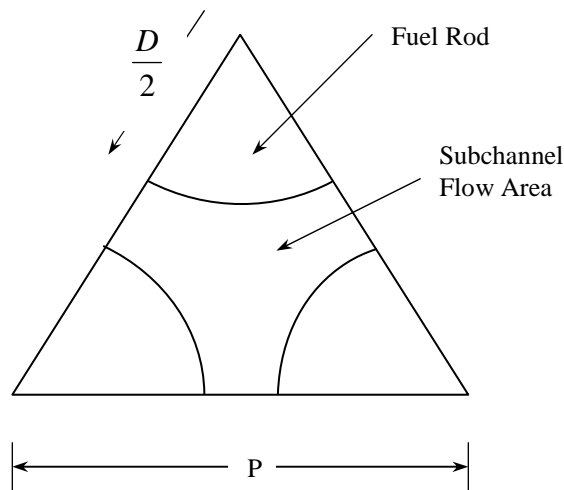


Figure 4.5: Hexagonal Array Axial Average unit subchannel dimensions

The pitch for the B Ring subchannel is 0.041 meters (1.60 in) [64]. Referring to Figure 3.6 the fuel element outer diameter for all OSTR core fuel elements is defined as 0.037

meters (1.47 in). Equation (4.1) defines the subchannel flow area for a hexagonal array [67] as:

$$A_{fi} = \frac{\sqrt{3}}{4} P^2 - \frac{\pi D^2}{8} \quad \text{Equation (4.1)}$$

Where P represents fuel element pitch, and D represents the fuel element outer diameter as shown in Figure 4.5. From Equation (4.1) the subchannel flow area is calculated to be $1.65 \cdot 10^{-4} \text{ meters}^2$ (0.26 in^2).

The wetted perimeter for the subchannel only occupies one half of an entire fuel element, therefore the total flow area for the subchannel input into the RELAP5-3D model is $3.30 \cdot 10^{-4} \text{ meters}^2$ (0.51 in^2).

4.2.5.2 Subchannel Length

Figure 4.4 compares an OSTR fuel element and the RELAP5-3D discretized subchannel volume. As previously discussed, Nodes 01 and 24 represent the lower and upper grid plates, both being 0.019 meters (0.75 in) thick; the upper grid plate is located exactly 0.67 meters (26.5 in) above the lower grid plate [70]. From Figure 3.6 the fuel element axial dimensions can be seen.

The total axial length in the fuel elements (lower graphite, fuel, upper graphite) is 0.56 meters (21.91 in). Because the sum of these defined segments is not equivalent to the required 0.673 meters (26.5 in) to span between the upper and lower grid plates and the lower graphite segment is approximately $7.62 \cdot 10^{-3} \text{ meters}$ (0.03 in) longer than the upper graphite segment it is assumed that the fuel portion of the fuel element is skewed up from the axial center of the core by $7.62 \cdot 10^{-3} \text{ meters}$ (0.03 in). Therefore the equation to calculate the length of Node 02 (lower unheated node) is:

$$L_{02} = \frac{(0.6731 - L_{fuel} - L_{Upper,graphite} - L_{Lower,graphite})}{2} + L_{Lower,graphite} \quad \text{Equation (4.2)}$$

L_{02} is the length of Node 02 and $L_{Upper,graphite}$ and $L_{Lower,graphite}$ are the upper and lower graphite lengths of the fuel element.

From Figure 3.6 the fuel nodal lengths must be discretized accordingly and can be done by referring to the following equation for Nodes 03 through 22:

$$L_{03 \rightarrow 22} = \frac{L_{fuel}}{n_u - (n_l - 1)} \quad \text{Equation (4.3)}$$

$L_{03 \rightarrow 22}$ refers to the nodal length for Nodes 03 through 22, n_u is the larger nodal number, n_l is the smaller nodal number.

To calculate the nodal length for Node 23 (upper unheated node) the following equation is used:

$$L_{23} = \frac{(0.6731 - L_{fuel} - L_{Upper,graphite} - L_{Lower,graphite})}{2} + L_{Upper,graphite} \quad \text{Equation (4.4)}$$

From Equations (4.2), (4.3), and (4.4), Table 4.5 is formulated. It is important to note that the nodal lengths stated in Table 4.5 apply to Volume 103 only.

Table 4.5: Core Volume Nodal Lengths

Core Volume Axial Nodal Lengths		
Nodal Description	Node Number	Nodal Length [m] (in)
Upper Grid Plate	24	0.01905 (0.75000)
Upper Graphite	23	0.14567 (5.73504)
Fuel	22	0.01905 (0.75000)
	21	0.01905 (0.75000)
	20	0.01905 (0.75000)
	19	0.01905 (0.75000)
	18	0.01905 (0.75000)
	17	0.01905 (0.75000)
	16	0.01905 (0.75000)
	15	0.01905 (0.75000)
	14	0.01905 (0.75000)
	13	0.01905 (0.75000)
	12	0.01905 (0.75000)
	11	0.01905 (0.75000)
	10	0.01905 (0.75000)
	09	0.01905 (0.75000)
	08	0.01905 (0.75000)
	07	0.01905 (0.75000)
	06	0.01905 (0.75000)
	05	0.01905 (0.75000)
	04	0.01905 (0.75000)
	03	0.01905 (0.75000)
Lower Graphite	02	0.14643 (5.76504)
Lower Grid Plate	01	0.01905 (0.75000)

4.2.5.3 Material Roughness

A value of $2.134 \cdot 10^{-6}$ meters ($8.4 \cdot 10^{-5}$ in) has been estimated for the fuel clad roughness due to its wide range of possible fabrication methods, it is also the most likely roughness given the fabrication methods used for this particular application [71].

4.2.5.4 Form Loss

The inlet and outlet form loss coefficients represent the form losses of the rod bottom and top rod fixtures. The form loss coefficient is a localized geometric parameter that quantifies fluid flow resistance due to a local change in geometry. Form loss is a dimensionless parameter and is given as [72]:

$$K = \frac{2\Delta P}{\rho v^2} \quad \text{Equation (4.5)}$$

Past studies have been performed toward quantifying TRIGA[®] core form losses of different lattice configurations, the results from these studies represented large variance in their results, and were not able to correlate a definite form loss value for each lattice configuration [9]. A study conducted by General Atomics for the OSTR developed a methodology for calculating each effective subchannel form loss rather than local form losses within the core [10]. These coefficients as well as a summary of the thermal hydraulic parameters found in the OSTR core hot channel are presented in Table 4.6. A brief description of how these form loss were calculated in the General Atomics study follows.

Equation (4.5) is not easily quantified with reference to the OSTR lower and upper grid plate geometry, for this reason it is assumed that the form losses are comprised of either sudden expansions or sudden contractions Equations (4.6) and (4.7).

$$K_{SE} = \left(1 - \frac{d^2}{D^2}\right)^2 \quad \text{Equation (4.6)}$$

$$K_{SC} \approx 0.42 \left(1 - \frac{d^2}{D^2}\right) \quad \text{Equation (4.7)}$$

Sudden expansion form losses typically result in a form loss less than a value of 1.0. For low flow, low pressure systems the resulting form loss is approximately 0.3. A visual of a sudden expansion is presented in Figure 4.6 (a).

Sudden contraction form losses are nominally ~1.3 at low pressures and low flow rates (i.e. natural circulation) [73]. A visual of a sudden contraction is presented in Figure 4.6 (b).

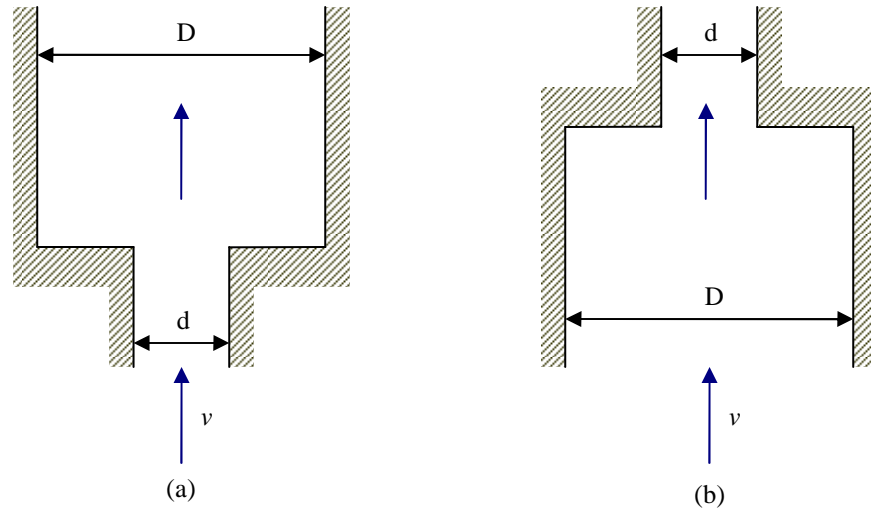


Figure 4.6: Sudden Expansion (a) and Sudden Contraction (b)

Table 4.6: Single Channel Model Geometric Thermal Hydraulic Properties Summary

Parameter	Value
Flow area [m ²]	$3.80 \cdot 10^{-4}$
Fuel Element Pitch [m]	0.04064
Wetted perimeter [m]	0.117
Hydraulic diameter [m]	$1.301 \cdot 10^{-2}$
Heated diameter [m]	$3.734 \cdot 10^{-2}$
Fuel element heated length [m]	0.381
Fuel element surface area [m ²]	$4.469 \cdot 10^{-2}$
Fuel element surface roughness [m]	$2.134 \cdot 10^{-6}$
Inlet pressure loss coefficient	2.26
Exit pressure loss coefficient	0.63
Absolute pressure at the top of the core [Pa]	$1.43 \cdot 10^5$

4.2.6 Coolant Sink (104)

The coolant sink models the coolant mass flux leaving the hot channel in the OSTR. The coolant sink is modeled in RELAP5-3D as a time dependent volume and is identical in geometry and orientation to the coolant source.

As discussed in section 4.2.2 the initial outlet coolant temperature and absolute pressure are defined respectively as 49.0 °C (120.2 °F) and $1.43 \cdot 10^5$ Pa (20.7404 psia). These boundary input parameters can be seen in Table 4.1. The geometric

parameters for volume 104 are presented in Table 4.2. It is important to note that the boundary conditions in the coolant sink do not convect back into the solution domain.

4.2.7 General Volume Parameters

The RELAP5-3D model, excluding core volumes, contains filler volumes (i.e. non-physical volumes that are required for the model to function correctly). These volumes, including the coolant source, cold leg, horizontal connector, and coolant sink, contain parameters that are similar to one another throughout the system and do not influence the hot channel solution.

4.2.7.1 *Material Roughness*

All volumes, excluding the hot channel volume, neglect material roughness calculations entirely as they are non-physical geometries in the RELAP5-3D model.

4.2.7.2 *Form Loss*

All volumes, excluding the hot channel volume, neglect form loss calculations entirely as they are non-physical geometries in the RELAP5-3D model.

4.2.8 Hot Channel Heat Structure

All heat generation takes place within the heat structure. This heat structure is defined by material composition, heat transfer surface area, geometric orientation, and power density. A heat structure cannot be implemented in a system without tying it to a subsequent hydraulic volume; volumes produce the boundary conditions that allow heat structures to complete their calculations correctly. The OSTR RELAP5-3D model is comprised of a single heat structure volume (hot channel fuel element). This volume represents the core power generation of the hot channel in the OSTR.

The OSTR is licensed for steady state operation at 1.1 MW_{th} and has the potential of running at full power load. Although Oregon State chooses to impose a 1.0 MW_{th} limit all thermal hydraulic steady state analyses were conducted at its licensed power level.

The MCNP5 core neutronic analysis identified that the hot channel was located in the B3 fuel element location for the OSTR at 1.1 MW_{th}. A power table was developed in the RELAP5-3D model to simulate the thermal output of the core.

All thermal hydraulic results are dependent on the power distribution found in the single channel heat structure (301). From the same neutronic analysis the axial fuel element power distribution and radial fuel element power distribution were calculated.

As mentioned, the hot channel contains a single heat structure (301). Figure 4.4 represents the hot channel heat structure and the subsequent nodes that it parallels. Three core configurations were analyzed during this project for the HEU core and the LEU core respectively: Beginning of Life, Middle of Life (MOL), and End of Life (EOL). The development of these different thermal models is described in the following sections.

4.2.8.1 Heat Structure Discretization

As discussed in Chapter 3, heat structures are two dimensional elements in RELAP5-3D. Therefore, both a radial and axial power profile must be input into the RELAP5-3D model. The neutronic analysis conducted in MCNP5 resulted in an output of thermal power for each fuel element in the OSTR for a core thermal output of 1.1 MW_{th}.

A single fuel element is comprised of a pure zirconium pin located in the radial center of a fuel element, U-ZrH fuel press fit around the zirconium pin, a small hydrogen filled gap created by contact resistance, and finally a stainless steel cladding as the outer casing for the fuel element, this configuration are presented in Figure 4.7.

The fuel to clad contact gap that is created by material surface roughness is originally hydrided during manufacturing of TRIGA[®] fuel [74]. As the U-ZrH fuel is burnt through its lifetime fission product gasses are released and migrate from the fuel lattice structure into the gap. These inert fission product gasses are an order of magnitude more heat resistant than the hydrogen that originally filled the gap. As a result of this increase in resistance the fuel temperature increases. It is therefore assumed that these fission product gasses are found in the fuel to clad gap during the study in order maintain a conservative approach to the thermal hydraulic safety analysis.

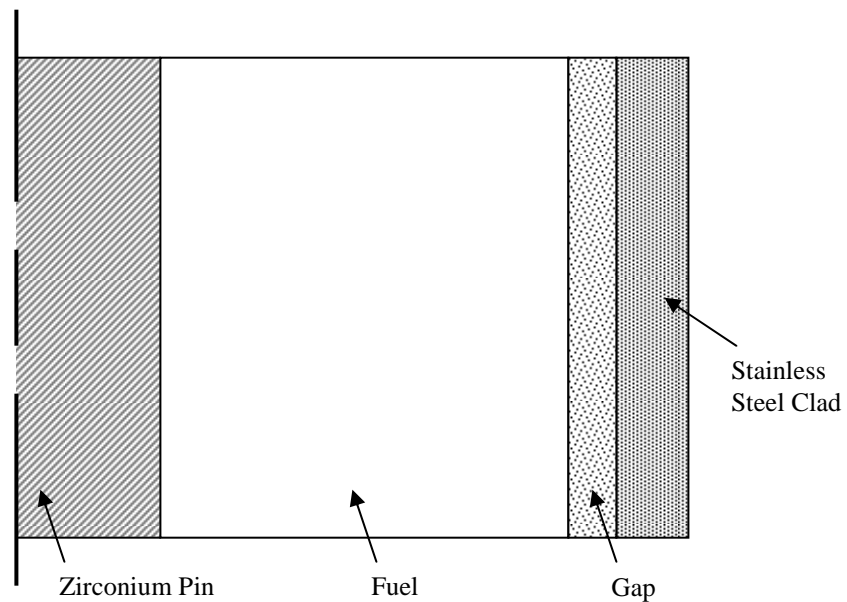


Figure 4.7: Cross Sectional View of Fuel Element

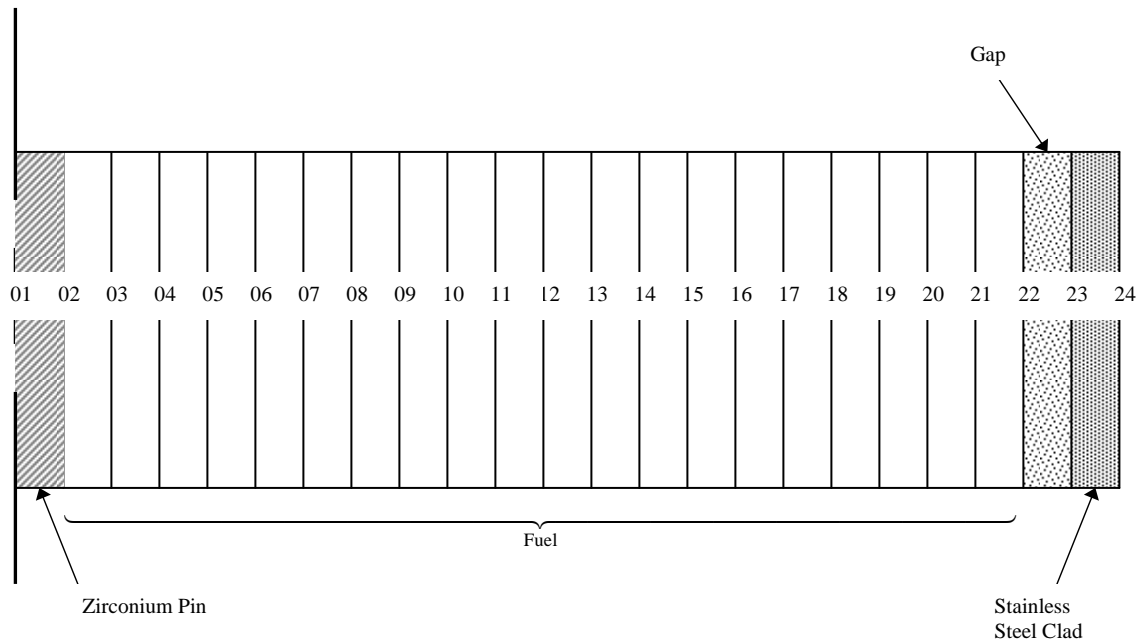


Figure 4.8: Radial Nodal Breakdown of Fuel Element

Because fission only occurs in the fuel region, it is the only radial region where a power profile must be defined in the RELAP5-3D model. The mesh points within the fuel region used in the RELAP5-3D model correspond to the results produced at given coordinate points in the MCNP5 analysis. As seen in Table 4.7, the radial distance for each material is identified. The outer gap coordinate (Node 22) is varied during this study.

The fuel to clad gap is due to surface roughness, and this roughness has the potential to vary due to the fuel manufacturing process. Because the gap has the highest thermal resistance found in a TRIGA[®] fuel element and all heat removal is radially conducted through the gap into the cladding and finally out to its ultimate heat sink (bulk coolant) it is important to acquire the accurate thickness of the gap so that the correct thermal resistance is used. Several references for TRIGA[®] fuel identify that the fuel to clad gap can vary from .05 to 0.4 mils [66, 75]. The effect of varying the fuel to clad gap was investigated using the single channel model and the results can be seen in Figure A.27 in Appendix A.

Table 4.7: Heat Structure Radial Node Lengths

Heat Structure Radial Node Lengths		
Nodal Description	Node Number	Node Coordinate [m] (in)
Outer Zirconium Pin	01	0.00000 (0.00000)
	02	0.00318 (0.12500)
Fuel	03	0.00355 (0.13976)
	04	0.00430 (0.16929)
	05	0.00506 (0.19921)
	06	0.00581 (0.22874)
	07	0.00656 (0.25827)
	08	0.00731 (0.28779)
	09	0.00807 (0.31772)
	10	0.00882 (0.34724)
	11	0.00957 (0.37677)
	12	0.01032 (0.40630)
	13	0.01108 (0.43622)
	14	0.01183 (0.46575)
	15	0.01258 (0.49527)
	16	0.01333 (0.52480)
	17	0.01409 (0.55472)
	18	0.01484 (0.58425)
	19	0.01559 (0.61378)
	20	0.01634 (0.64331)
	21	0.01710 (0.67323)
	22	0.01785 (0.70275)
Outer Gap	23	0.01785-0.01786 (0.70285-0.70305)
Outer Stainless Steel Clad	24	0.01873 (0.73750)

4.2.8.2 Heat Structure Thermo-physical Properties

Data from thermal diffusivity measurements taken by General Atomics along with the best available data for density and specific heat showed that the thermal conductivity is both independent of temperature and uranium content and can be seen below in Equation (4.8) [66].

$$K(T)_{HEU,LEU-FUEL} = 0.18 \pm 0.009 \quad [\text{W/cm-}^\circ\text{C}] \quad \text{Equation (4.8)}$$

TRIGA[®] FLIP fuel has a defined volumetric heat capacity as presented in Equation (4.9) [74, 75].

$$\rho C_P(T)_{HEU,LEU-FUEL} = 2.04 + 4.17 \cdot 10^{-3}(T) \quad [\text{W-sec/cm}^3\text{-}^\circ\text{C}] \quad \text{Equation (4.9)}$$

Since the Uranium to Zirconium Hydride concentration is very similar between the HEU and LEU TRIGA[®] fuel, and the only primary change in fuel alloy content is the uranium isotope concentration, it can be assumed that the LEU volumetric heat capacity found in the LEU fuel is similar to that in the HEU fuel [74].

4.3 Two Channel Model Description

A two channel model has been constructed in parallel with the single channel model to quantify the thermal hydraulic differences that are found during steady state operation. Figure 4.9 presents the schematic of the two channel model constructed for this quantitative comparison.

The two channel model is very similar to the single channel model, but incorporates a single volume adjacent to the hot subchannel. This single volume (102 in Figure 4.9) incorporates the remaining fuel elements in the core. 88 fuel elements including all fuel followed control rods and the instrumented fuel element can be found in both the HEU and LEU Beginning of Life Normal Cores. It is assumed that all hot channel geometric characteristics carry into the remaining 87 fuel elements that make up the core. These 87 fuel elements are represented by a single channel in the RELAP5-3D model. In order to maintain the hot channel power factor produced from the MCNP analysis a core averaging method was used to acquire the equivalent core power that produces a resultant 1.1 MW_{th} .

Cross flow is represented by junctions in RELAP5-3D that connect to adjacent subchannel volumes at every axial node in the core. No friction calculations were implemented in the RELAP5-3D cross-flow junctions.

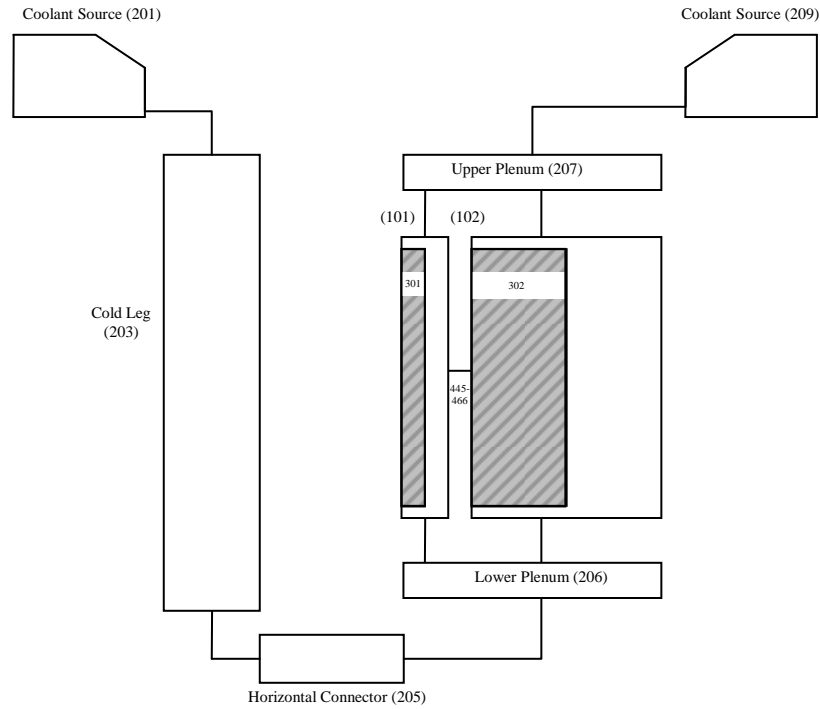


Figure 4.9: Two Channel RELAP5-3D Model Schematic

Table 4.8: Two Channel Model Geometric Thermal Hydraulic Properties Summary

Parameter	Hot Channel Volume (101)	Lumped Core Volume (102)
Flow area [m ²]	$3.80 \cdot 10^{-4}$	$3.306 \cdot 10^{-2}$
Hydraulic diameter [m]	$1.301 \cdot 10^{-2}$	1.1319
Fuel element surface area [m ²]	$4.469 \cdot 10^{-2}$	3.888
Subchannel Volume Thermal Power [kW] (HEU, LEU)	18.02, 17.77	1081.98, 1082.23

RELAP5-3D requires that two additional volumes be added to the two channel model as a result of incorporating the lumped core volume, the upper and lower plenum. These volumes do not play a role in the results produced during the analysis, but are a requirement for the RELAP5-3D input deck. All other volumes in the model remain similar to that found in the single channel model.

4.4 Eight Channel Model Description

Similar to the methodology used when constructing the two channel model, the eight channel model is further discretized into more refined subchannel volumes (100 through 107 in Figure 4.10). Each volume represents a corresponding location in the core lattice. In the eight channel model, two subchannels do not have heat structures incorporated in them (100 and 107). These volumes represent the A Ring where a single Aluminum slug is found and the G ring which is comprised of only graphite reflector elements.

Volume 101 represents the hot channel located in the B ring; in the eight channel model, cross flow is taken into account by providing junctions between the A ring, B Ring Hot Channel and the B Ring remaining fuel elements (102). Volumes 103 through 106 represent Rings C through F respectively. Similar to the two channel model, all other volumes are proportional to the hot channel geometry by the number of fuel elements that are represented in that subchannel. A summary of the subchannel properties is presented in Table 4.9.

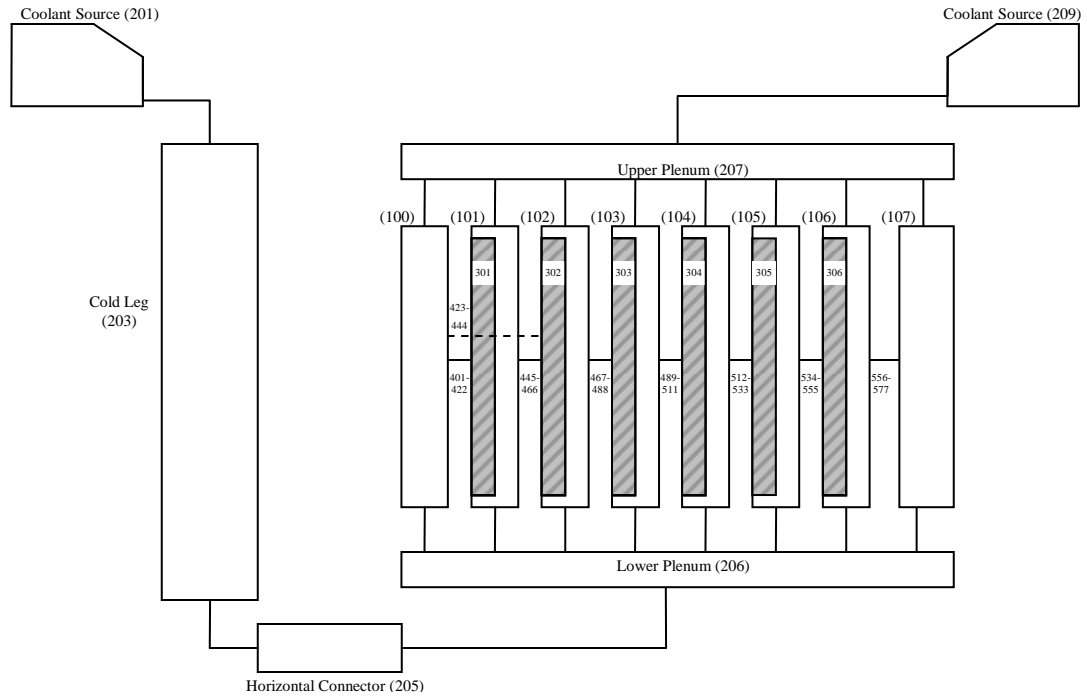


Figure 4.10: Eight Channel RELAP5-3D Model Schematic

Table 4.9: Eight Channel Model Geometric Thermal Hydraulic Properties Summary

Parameter	A Ring (100)	B Ring Hot Channel (101)	B Ring Remaining Elements (102)	C Ring (103)	D Ring (104)	E Ring (105)	F Ring (106)	G Ring (107)
Flow area [m ²]	$3.80 \cdot 10^{-4}$	$3.80 \cdot 10^{-4}$	$1.90 \cdot 10^{-3}$	$4.18 \cdot 10^{-3}$	$6.48 \cdot 10^{-3}$	$9.12 \cdot 10^{-3}$	$9.88 \cdot 10^{-3}$	$1.37 \cdot 10^{-2}$
Hydraulic diameter [m]	$1.30 \cdot 10^{-2}$	$1.30 \cdot 10^{-2}$	$6.55 \cdot 10^{-2}$	$1.44 \cdot 10^{-1}$	$2.36 \cdot 10^{-1}$	$3.14 \cdot 10^{-1}$	$3.41 \cdot 10^{-1}$	$4.716 \cdot 10^{-1}$
Fuel element surface area [m ²]	0.0	$4.46 \cdot 10^{-2}$	$2.23 \cdot 10^{-1}$	$4.91 \cdot 10^{-1}$	$8.03 \cdot 10^{-1}$	1.07	1.16	0.0
Subchannel Volume Thermal Power [kW] (HEU, LEU)	0.0	18.02, 17.77	88.28, 85.66	181.09, 176.68	254.46, 250.57	284.43, 278.29	273.72, 291.03	0.0

5. STEADY STATE ANALYSIS

5.1 Critical Heat Flux Correlation Comparison

As presented in Chapter 2, six different methods for calculating critical heat flux with reference to the core conversion project are considered. In order to quantitatively compare the relationship of these correlations, the HEU Beginning of Life Normal core was chosen to be analysed.

RELAP5-3D internally calculates the critical heat flux with reference to the 1986 AECL Groeneveld look-up tables. All other correlations were calculated externally using the thermal hydraulic properties resulting from the RELAP5-3D model. In order to verify that these external calculations were being completed in the correct manner, the critical heat flux was calculated externally with reference to the 1986 AECL Groeneveld look-up tables. The result of this comparison is shown in Figure 5.1. The external calculations produced values that deviated from those conducted in RELAP5-3D by ~1.0% on the conservative side. The deviation was potentially caused by round off error. Qualitatively, this deviation was estimated to be within an acceptable margin. The axial CHFR distribution for the RELAP5-3D internally calculated values as well as all external calculated values are presented in Figure 5.1 and Figure 5.2.

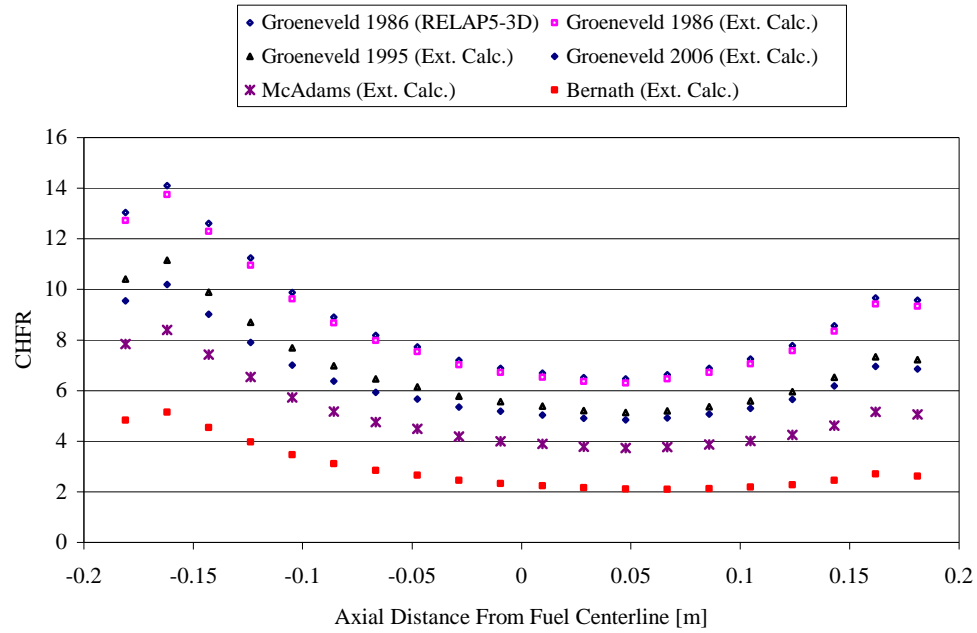


Figure 5.1: Axial CHFR Distribution, Correlation Comparison
(HEU Beginning of Life Normal Core using the single channel model)

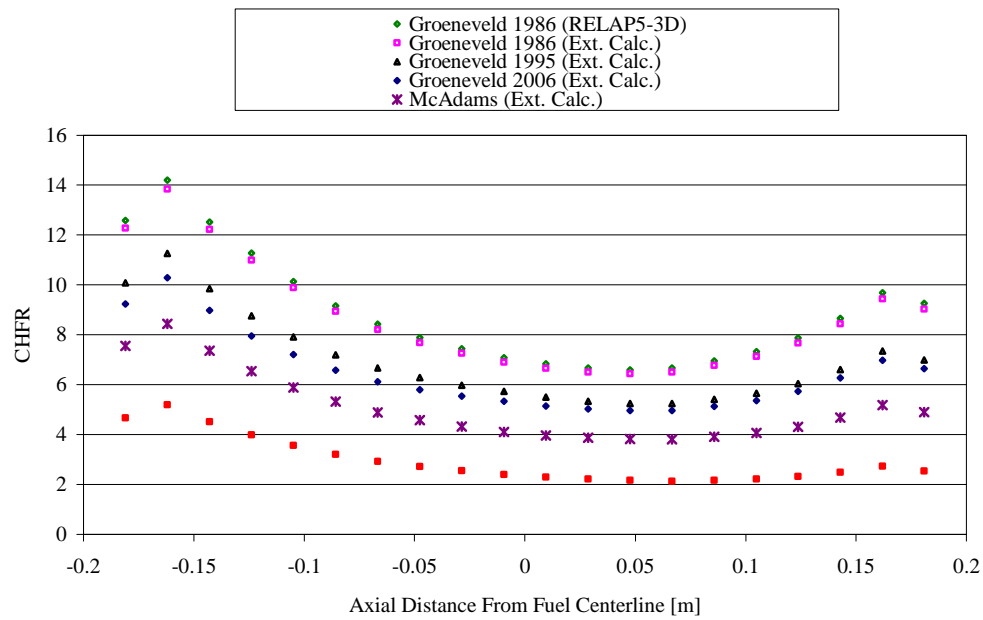


Figure 5.2: Axial CHFR Distribution, Correlation Comparison
(LEU Beginning of Life Normal Core Configuration using the single channel model)

As presented in Figure 5.1, the 1986 AECL Groeneveld look-up tables produce the least conservative CHFR distribution values, followed by the 1995 and 2006 Tables. The McAdams correlation and Bernath correlation, although having the largest error associated with them, produce the most conservative CHFR distribution values.

General Atomics, the manufacturer of the OSTR, conducted its original safety analysis of the design using the McAdams and Bernath Correlations to calculate the CHFR. Therefore, these are traditionally regarded as the more reliable CHFR correlations with regard to the OSTR. Table 2.1, presented in Chapter 2, identifies the approximate error associated with the look-up tables within the operating region of the OSTR. From this table it can be seen that the 2006 tables present a smaller error than the 1986 or 1995 tables.

Based on the results presented in Figure 5.1, the 2006 Groeneveld look-up tables and the Bernath correlation were used in the final version of the core conversion project. They were chosen for the following reasons:

- Bernath -
 - It is traditionally used as a supplement in research reactor SARs with respect to the RERTR program including the recent submission of the Washington State University Research Reactor [76], the University of Massachusetts Lowell Research Reactor [23], and the South African MNSR [77].
 - The correlation produces the most limiting CHFR values over all other correlations considered during this study.
- 2006 AECL Groeneveld look-up Tables -
 - The correlation is the most accurate method for calculating CHF values over all others considered during this study.

5.2 1, 2, & 8 Channel Model Results Comparison

5.2.1 HEU Beginning of Life Normal Core

Figure 5.3 presents the two dimensional (axial and radial) fuel element temperature distribution for the steady state solution of the HEU Beginning of Life Normal Core. This profile can be broken into two individual vectors as seen in Figure 5.4 and Figure 5.5.

The peak fuel temperature is located in the axial and radial center of the fuel portion of the fuel element and is found to be 447.5 °C while the outer clad temperature at the same corresponding axial position is 131.1 °C. The 0.1 mil fuel to clad contact gap produces a temperature drop of 87.02 °C, and verifies that the gap has the largest thermal resistance in the OSTR TRIGA[®] fuel element. When observing the axial fuel centreline temperature distribution, the peaks in fuel temperature at each fuel element end are due to the increase in neutron flux as a result of thermal reflection in the moderator (coolant).

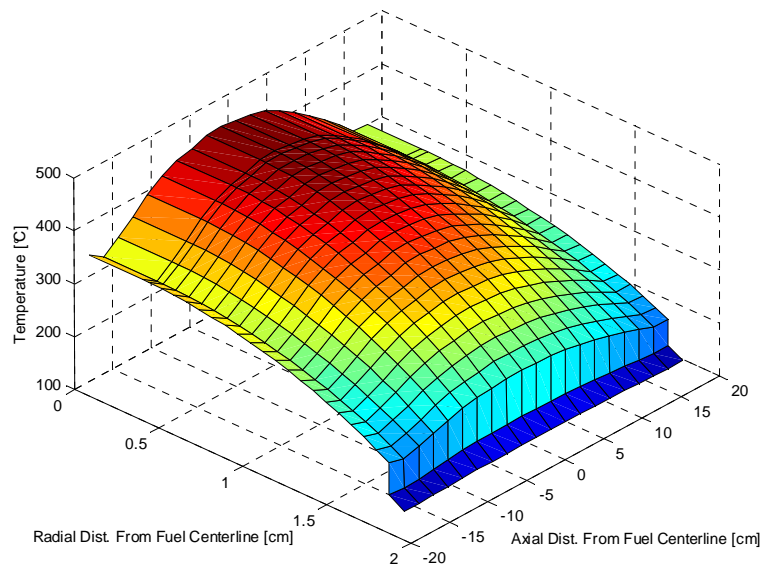


Figure 5.3: Nodal Fuel Temperature Distribution for 1, 2, & 8 Channel Model (HEU Beginning of Life Normal Core Configuration)

A single fuel temperature profile is presented in Figure 5.3 through Figure 5.5 that represents the one, two, and eight channel model. This is because the hot channel fuel elements in each model produces the same internal heat generation rate, are made of the same material, and have the same geometry, therefore their temperature distributions are the same. Moving outward from the radial center of the fuel element the temperature, $T(r=0)$, at the center of the fuel element pertains to the center of the zirconium pin that runs the axial length of the fuel element. Moving outward, the three outermost temperature positions represent the temperature drop across the fuel element gap and the fuel element clad.

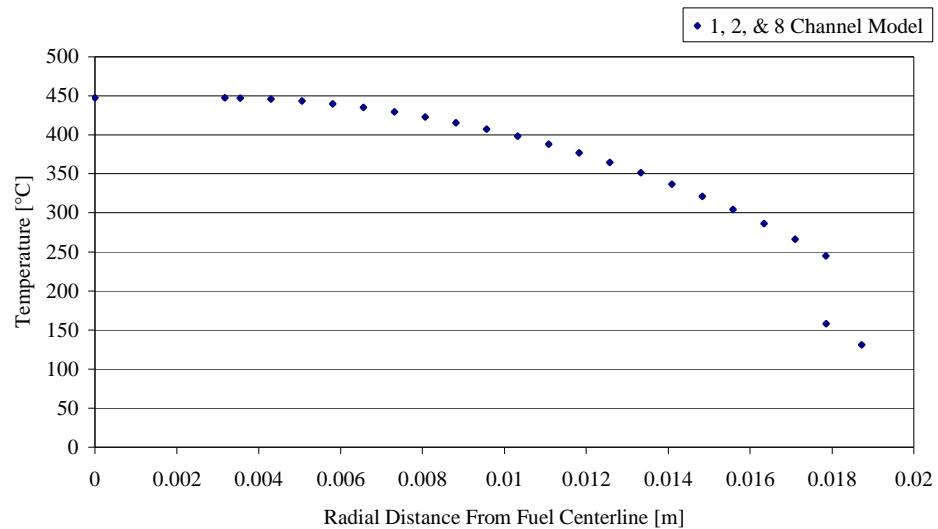


Figure 5.4: Radial Hot Channel Fuel Temp. Distribution for 1, 2, & 8 Channel Model (HEU Beginning of Life Normal Core)

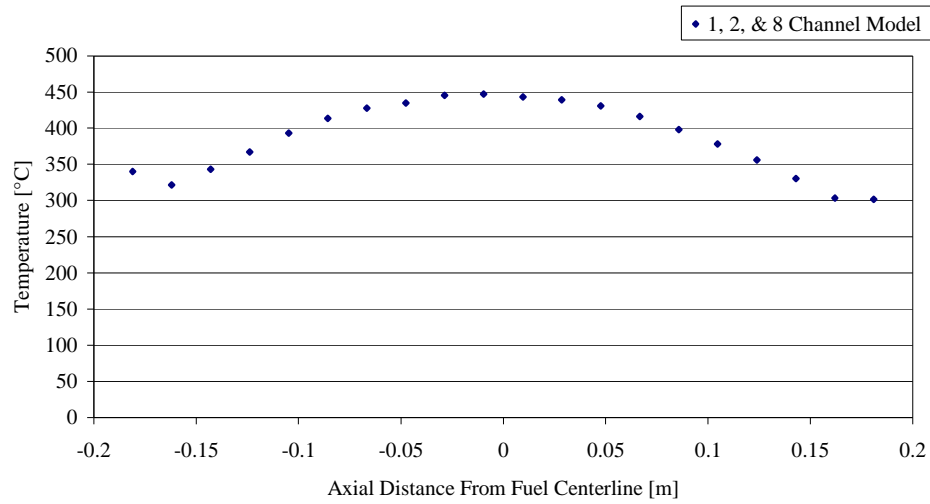


Figure 5.5: Axial Hot Channel Fuel Temp. Distribution for 1, 2, & 8 Channel Model (HEU Beginning of Life Normal Core)

Figure 5.6 provides a quantitative comparison of the bulk coolant temperature distribution found in the one, two and eight channel model. This comparison provides evidence that with an increase in number of subchannels a corresponding decrease in exit bulk coolant temperature will result as expected.

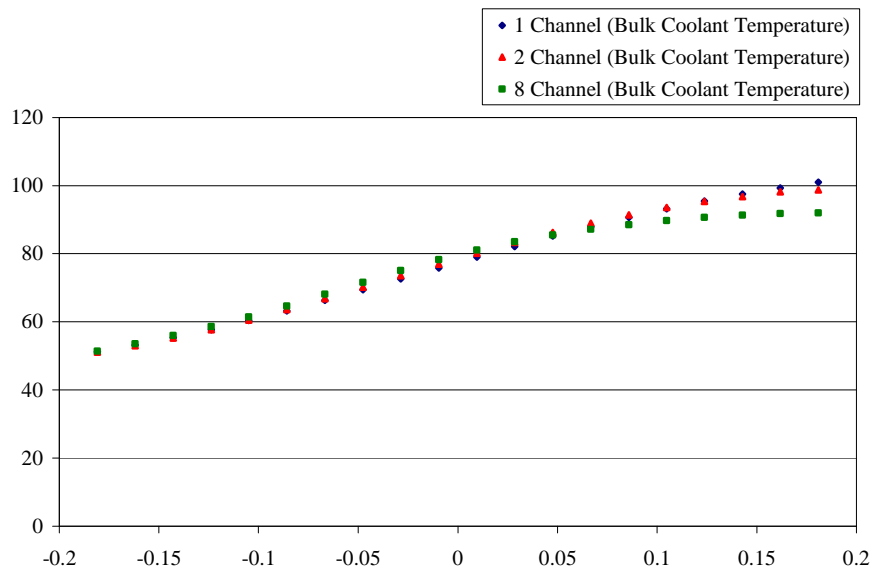


Figure 5.6: Axial Bulk Coolant Temperature Distribution for 1, 2, & 8 Channel Model (HEU Beginning of Life Normal Core)

The coolant equilibrium quality and subchannel mass flux are presented in Figure 5.7 as a function of axial position. These properties, along with system pressure, are the primary parameters for CHF. With an increase in subchannels the mass flux is perturbed greater due to cross flow in the lower axial portion of the core.

The equilibrium quality for the single, two, and eight channel model remain similar though the majority of the axial length of the core. As a result of the increased mass flux in the eight channel model near the exit of the subchannel, less energy is deposited into the fluid producing lower equilibrium quality values for the eight channel model relative to the two and one channel models.

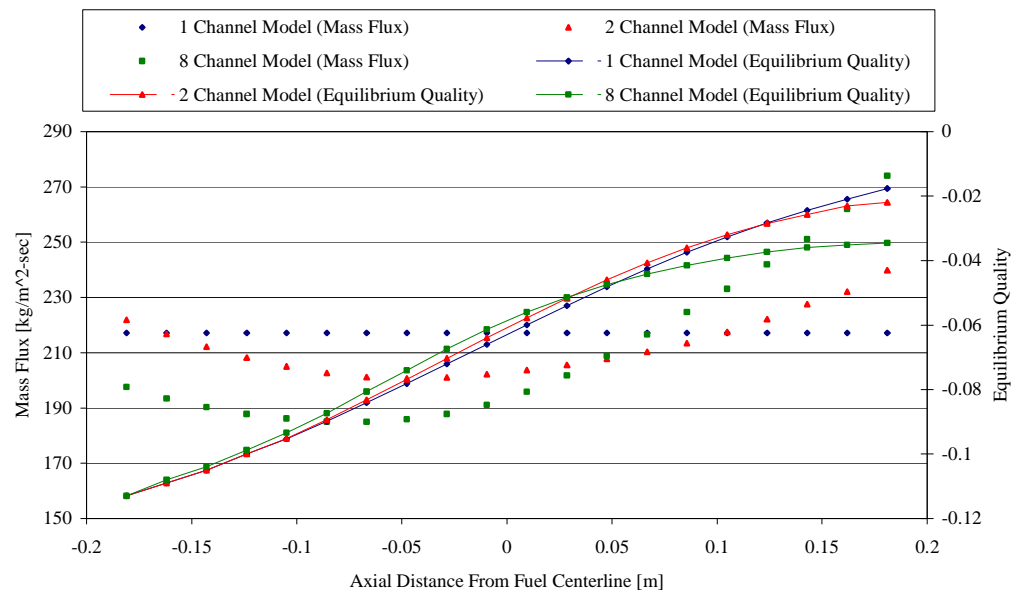


Figure 5.7: Mass Flux and Equilibrium Quality Distribution for 1, 2, & 8 Channel Model (HEU Beginning of Life Normal Core)

Figure 5.8 presents the CHFR determined using the 2006 Groeneveld AECL look-up tables and Bernath correlation for the one, two, and eight channel models. Small

differences in the CHF values for the different models compared can be accounted for by the observations made above. The exit CHF value for the eight channel model is larger than the two channel, which is larger than the one channel model. This is due to a decrease in equilibrium quality near the exit of the subchannel. Although there are small deviations in the CHF axial distributions it is important to note that the minimum critical heat flux ratio (MCHFR) as presented in Table 5.1 differs by only 0.3% on average for the look-up tables and 0.6 % for the Bernath correlation. This is well within the error margin associated with each CHF method of calculation.

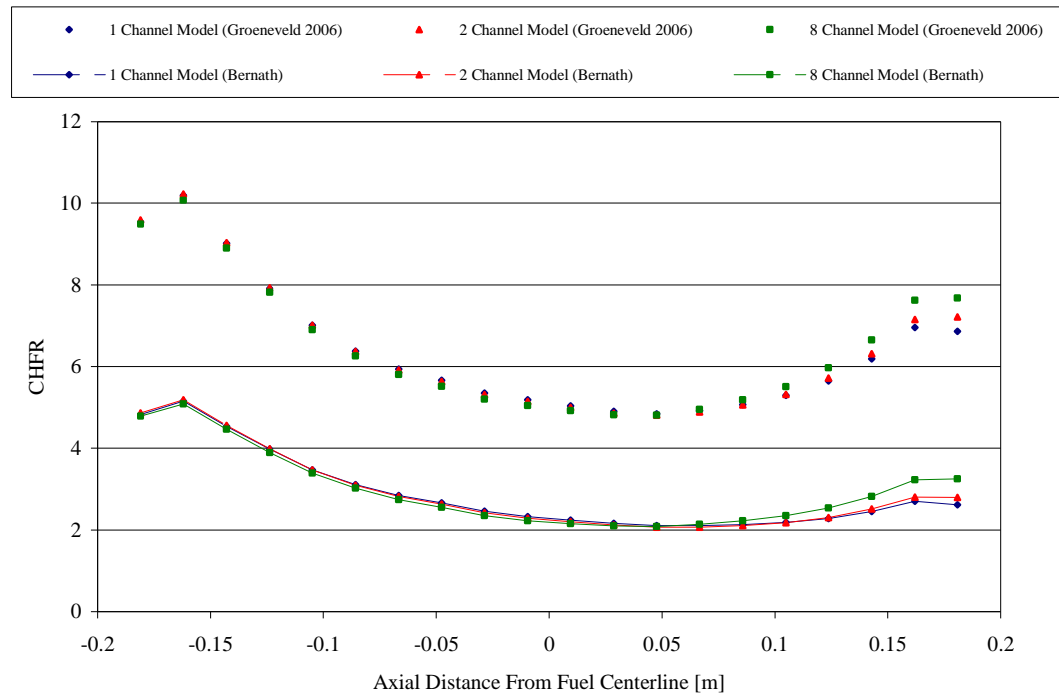


Figure 5.8: Axial CHF Distribution for 1, 2, & 8 Channel Model
(HEU Beginning of Life Normal Core)

Table 5.1: MCHFR Comparison for 1, 2, & 8 Channel Model
(HEU Beginning of Life Normal Core)

MCHFR Comparison		
	Groeneveld 2006	Bernath
1 Channel Model	4.844	2.104
2 Channel Model	4.806	2.067
8 Channel Model	4.813	2.087

5.2.2 LEU Beginning of Life Normal Core

The following results are produced for the LEU Beginning of Life Normal Core. The trends found for all thermal hydraulic properties in the LEU core are similar to those found in the HEU core.

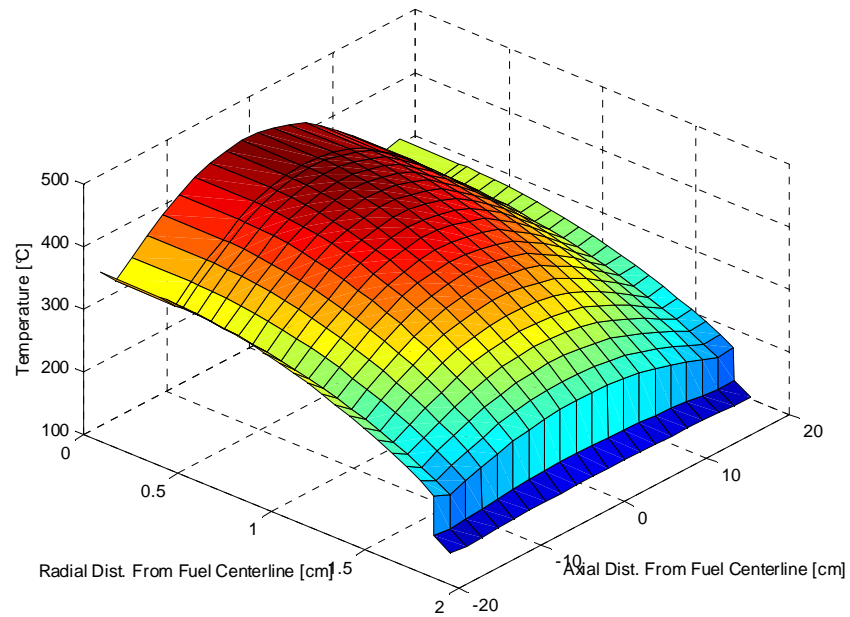


Figure 5.9: Nodal Fuel Temperature Distribution for 1, 2, & 8 Channel Model (LEU Beginning of Life Normal Core Configuration)

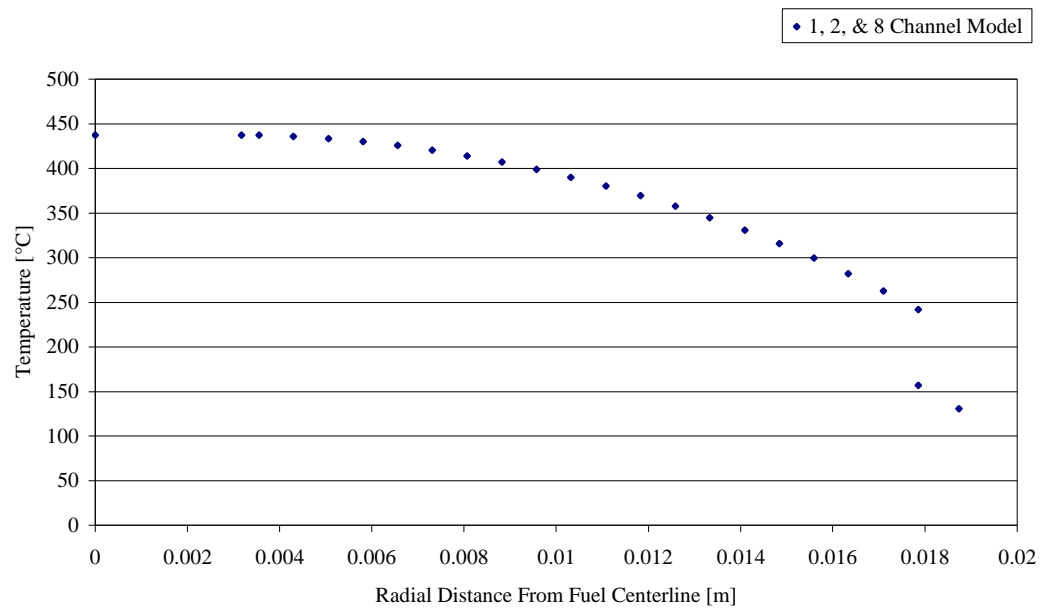


Figure 5.10: Radial Hot Channel Fuel Temp. Distribution for 1, 2, & 8 Channel Model (LEU Beginning of Life Normal Core)

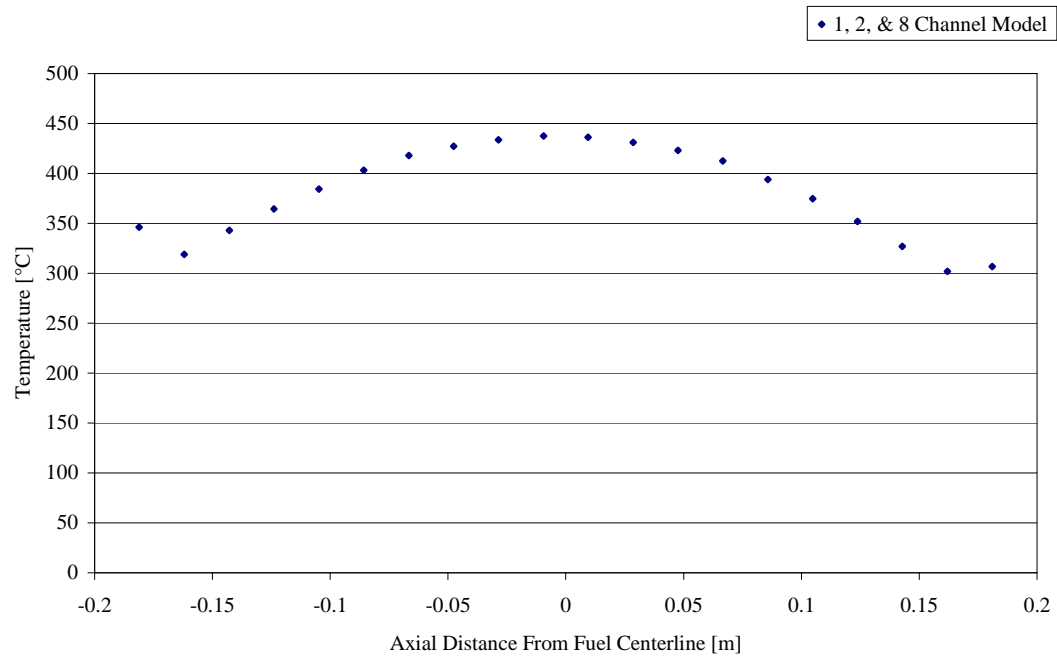


Figure 5.11: Axial Hot Channel Fuel Temp. Distribution for 1, 2, & 8 Channel Model (LEU Beginning of Life Normal Core)

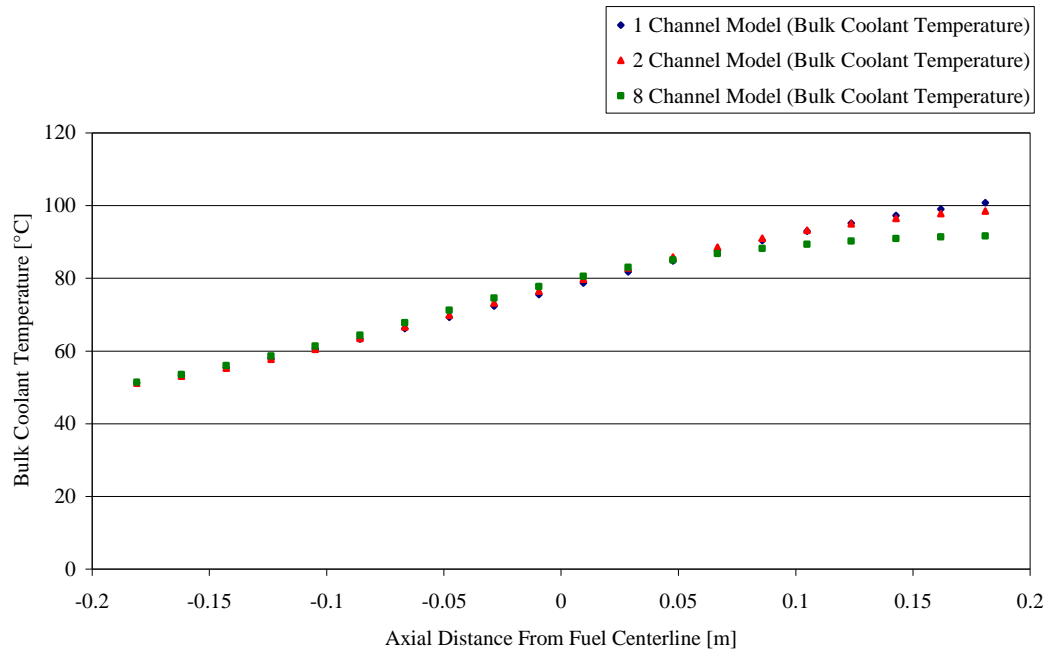


Figure 5.12: Axial Bulk Coolant Temperature Distribution for 1, 2, & 8 Channel Model (LEU Beginning of Life Normal Core)

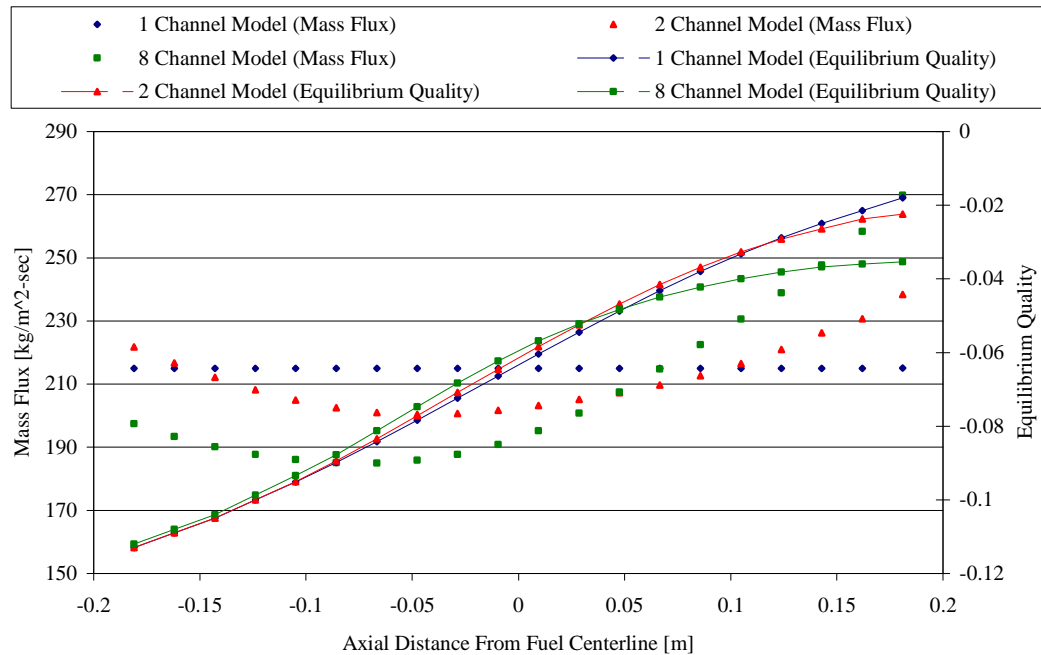


Figure 5.13: Mass Flux and Equilibrium Quality Distribution for 1, 2, & 8 Channel Model (LEU Beginning of Life Normal Core)

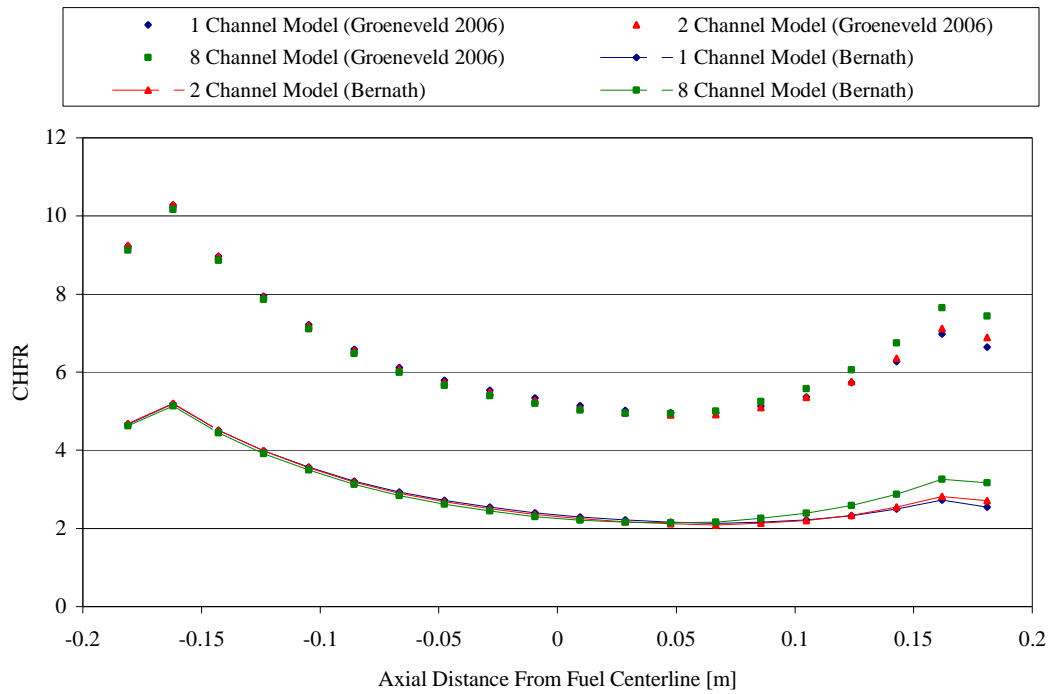


Figure 5.14: Axial CHFR Distribution for 1, 2, & 8 Channel Model
(LEU Beginning of Life Normal Core)

Table 5.2: MCHFR Comparison for 1, 2, & 8 Channel Model
(LEU Beginning of Life Normal Core)

MCHFR Comparison		
	Groeneveld 2006	Bernath
1 Channel Model	4.957	2.128
2 Channel Model	4.900	2.090
8 Channel Model	4.932	2.147

6. PULSE ANALYSIS

6.1 Discussion

As mentioned in Chapter 3 the OSTR has a pulse capability. Several mechanisms within the U-ZrH OSTR fuel allow for a large rapid positive reactivity insertion in the core to occur. In the event of a power increase the molecular structure provides for a strong negative temperature dependent prompt fuel temperature coefficient in the U-ZrH. The U-ZrH fuel also contains a burnable poison, erbium. Erbium is the primary contributor to the OSTR's ability to sustain large positive reactivity insertions. Erbium's absorption cross section has a characteristic resonance peak that is large in magnitude and wide in energy range found at a very low energy level (~0.2 eV to 1.0 eV) [75]. As the fuel temperature increases as a result of a large positive reactivity insertion, the thermal neutrons in the core are excited to a higher energy level. As they increase in energy they move into the resonance absorption peak of the erbium. This increases the neutrons' probability of absorption in the erbium prior to fission and inherently shuts down the reactor which in turn allows for the TRIGA[®] to be safely pulsed to a high short term power level [75].

The current SAR limits the OSTR to a maximum insertion of \$2.55. This reactivity insertion is limited by the maximum fuel temperature that is produced as a result of the rapid insertion of energy deposited into the hot channel fuel element. Table 3.3 describes individual fuel element peak factors associated with each core configuration evaluated during the core conversion project. These peak factors inherently effect the maximum fuel temperature produced in a fuel rod for a given reactivity insertion.

Three different methods for calculating the peak fuel temperature for the HEU Beginning of Life Normal Core and LEU Beginning of Life Normal Core hot channel fuel element are taken into consideration during this study. The three methods considered are:

- Explicitly solving for fuel maximum fuel temperature assuming an adiabatic system.
- Externally calculating the power trace during a pulse for the OSTR using a point reactor kinetics model and then applying it to RELAP5-3D as a time dependent power table.
- Implementing the Point Reactor Kinetics Model (PRKM) in RELAP5-3D for the two, and eight channel model.

6.1.1 External Explicit Solution

The maximum fuel temperature for a hot channel fuel element can be solved explicitly when assuming an adiabatic system using the energy equation below:

$$C_p(T) \frac{dT}{dt} = P(t) \quad \text{Equation (6.1)}$$

where P is the power as a function of change in time (dt) to result in a change in temperature (dT). The temperature dependence of specific heat in the fuel element (C_p) is handled explicitly with the change in fuel temperature (Refer to Equation (4.9) for specific heat implemented during this calculation). By implementing a given power profile produced from a point reactor kinetics model and incorporating the effective peak factor for a given core configuration (Table 3.3) the maximum fuel temperature can be solved.

6.1.2 External Numerical Solution

The behavior of the reactor during a pulse was analyzed using a point reactor kinetics model. The model is a coupled set of nine first-order differential equations given by the following equations [65]:

$$\frac{dP(t)}{dt} = \frac{\rho(t) - \beta}{\Lambda(t)} P(t) + \sum_{i=1}^6 \lambda_i C_i(t) \quad \text{Equation (6.2)}$$

$$\frac{dC_i(t)}{dt} = -\lambda_i C_i(t) + \frac{\beta_i}{\Lambda(t)} P(t), \quad i = 1 \dots 6 \quad \text{Equation (6.3)}$$

$$C_p(T) \frac{dT(t)}{dt} = P(t) \quad \text{Equation (6.1)}$$

The evolution of reactivity during the pulse is given by:

$$\int d\rho = \int \alpha_r(T) dT \quad \text{Equation (6.4)}$$

A complete derivation of the integral factor method used to solve the nine coupled equations explicitly is provided in Appendix B.

As can be seen in Equations (6.2) through (6.4), no moderator feedback characteristics are taken into account in this model. This assumption is justified because during a pulse the reactor operates under prompt supercritical conditions, and heat transfer into the bulk coolant (moderator) is negligible during the primary portion of the pulse power trace. It is important to note that there is no position dependence incorporated in Equations (6.2) through (6.4), therefore the solution of the above equations resulting from a given reactivity insertion is representative of the integral OSTR core. A resultant maximum fuel temperature for a given reactivity insertion is found by implementing the power trace solution from the point reactor kinetics model directly into the RELAP5-3D model.

The fissile fuel characteristics implemented in the point reactor kinetics model including the fuel temperature coefficient, effective delayed neutron fraction, and mean generation time were produced from the MCNP analysis conducted as part of the core conversion project as a function of core lifetime.

6.1.3 RELAP5-3D Numerical Solution

RELAP5-3D has the potential for the implementation of the point reactor kinetics model as previously discussed. It is postulated that Idaho National Laboratory based code has potential for producing more accurate results through the coupling of neutronic and thermal hydraulics models in a single code. By incorporating heat transfer in the model there is potential for changes in core power, specific heat, fuel temperature coefficient, and reactivity as a function of time. The maximum fuel temperature has potential to vary by altering these parameters in the RELAP5-3D model. It is also possible to incorporate moderator feedback when using RELAP5-3D. This too has the potential for changing the maximum fuel temperature of the hot channel fuel element for a given reactivity insertion.

6.2 Pulse Results

6.2.1 Power Trace Comparison

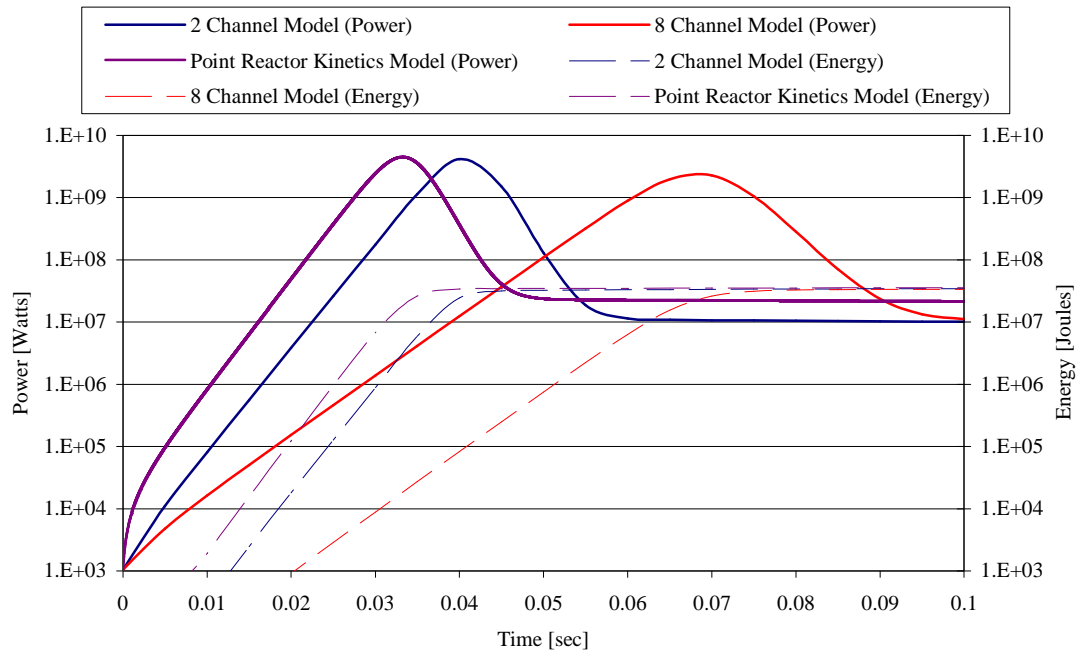


Figure 6.1: Pulse Power Trace Comparison (HEU Beginning of Life Core, \$2.00 Insertion)

The pulse power trace results presented in Figure 6.1 allow for the comparison of integrated energy deposited into the core as a function of time. Referring to Equation (6.1), the maximum fuel temperature for an assumed adiabatic system is inherently a function of energy. Therefore as a result of Figure 6.1 it could be assumed that if no heat transfer were to be considered, the power trace produced from the point reactor kinetics model (external numerical solution) produces a larger maximum fuel temperature than that produced in the two or eight channel RELAP5-3D model.

Figure 6.1 presents a deviation in rise time associated with the power trace for all four cases. The point reactor kinetics equations that govern the inherent system transient are dependent upon reactivity, prompt temperature coefficient, fuel temperature, and power. Because the initial conditions imposed on all four cases were the same as seen in Table 6.1 it can then be stated that the numerical solution is different for all four cases due to several possibilities:

- Iteration Time Step Differences
 - Due to the extremely short numerical value of the prompt neutron lifetime relative to all other terms defined within the point reactor kinetics model including effective delayed neutron fraction, reactivity, prompt temperature coefficient, power, and temperature the PRKM is inherently an extremely stiff set of coupled differential equations. Due to the explicit method (Integration Factor Method) in which these equations are solved there is potential for the solution to converge with different results as the time step is varied.
- Spatial Differences
 - Although the external numerical solution has no spatial dependence, there are spatial dependent terms found in the solution of the point reactor kinetic equations within RELAP5-3D. As a result of this, there

is a potential for variation in the numerical solution as a result of the number of nodal volumes found in the two and eight channel model.

- Variable Treatment Differences
 - The external numerical solution uses in-line linear polynomials for prompt temperature coefficient and specific heat to solve the PRKM. RELAP5-3D requires a piecewise table of prompt temperature coefficient and specific heat to be input as a function of temperature. This method for inputting these values has potential for round off error when RELAP5-3D linearly interpolates between the piecewise values. This difference in variable treatment for solving the point reactor kinetics equations has the potential to change the results between the external numerical solution and RELAP5-3D solution.

Table 6.1: Power Trace Results Initial Conditions

Initial Conditions	
Initial Temperature °C	50
Initial Power [W]	1000
Reactivity Insertion [\$]	2.00

6.2.2 Maximum Fuel Temperature Comparison

Fuel failure associated with maximum fuel temperature during a TRIGA[®] pulse is the driving motivation behind a pulse analysis. The maximum fuel temperature provides the limiting reactivity insertion that the OSTR will have legal authority to implement. The license limit for the OSTR is 1150 °C [74].

During a pulse the fuel thermo-physical properties inherently dominate the tendency for peak fuel temperature over heat removal capability of the system. This is due to the extremely short time period which a pulse occurs. In order to quantitatively compare the numerical methods for simulating an OSTR pulse, no thermo-physical properties were changed. Figure 6.2 presents the radial fuel temperature at the time that

maximum fuel temperature occurs during a pulse from the two RELAP5-3D Numerical Solutions considered during this study. It can be observed that the two and eight channel model have similar temperature values at the time of maximum fuel temperature.

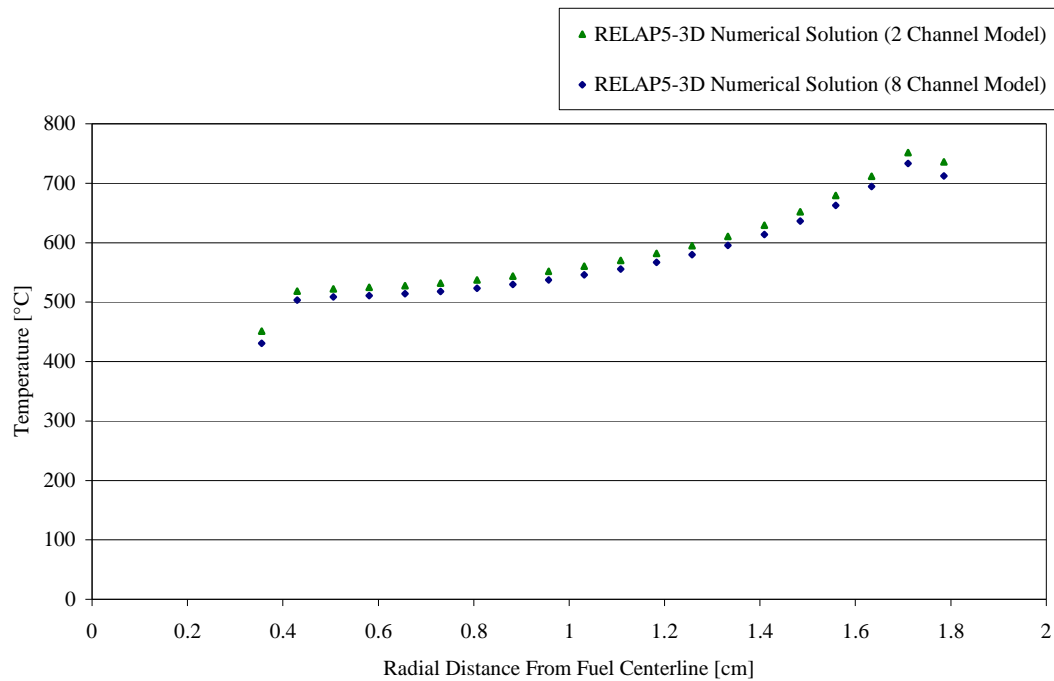


Figure 6.2: Fuel Radial Temperature at Maximum Fuel Temperature Time (HEU Beginning of Life Normal Core)

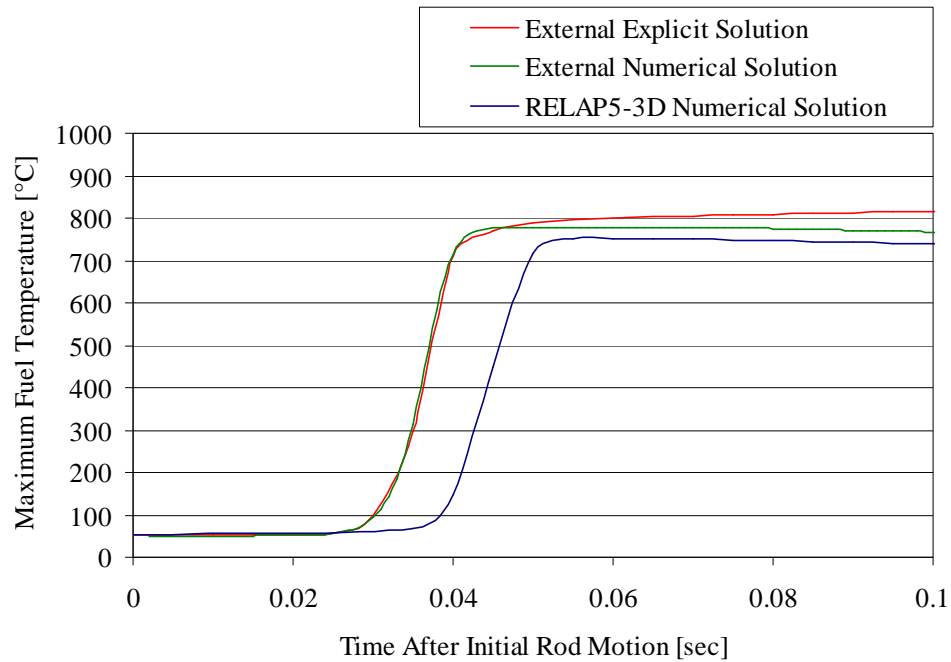


Figure 6.3: Transient Maximum Fuel Temperature Comparison
(HEU Beginning of Life Normal Core)

Figure 6.3 presents an example of the transient maximum fuel temperature for each solution method considered during this study.

The external explicit solution was produced by applying the power trace produced from the point reactor kinetics equations for the HEU Beginning of Life and applying that power trace to Equation (6.1). It can be seen that the maximum fuel temperature continually increases through the entire figure because the External Explicit Solution is assumed to be adiabatic and a function of energy deposited in the fuel.

The External Numerical Solution input the same power trace which was used in the External Explicit Solution and into the RELAP5-3D model. As a result a maximum fuel temperature of 779.23 °C at a time of 0.081 sec was calculated by RELAP5-3D.

In order to quantify a maximum fuel temperature for the external explicit solution it is assumed that the time that the maximum fuel temperature occurs is the same as that

produced from the external numerical solution. This assumption is justified because both solutions use the same power trace.

The RELAP5-3D numerical solution for the two channel model is presented in Figure 6.3 as well. By inserting the fissile fuel characteristics of the HEU Beginning of Life Core into the RELAP5-3D model a maximum fuel temperature of 751.65 °C at a time of 0.055 sec was calculated.

Table 6.2: Maximum Fuel Temperature Comparison Summary

Maximum Fuel Temperature Comparison Summary		
Solution Method	Time of Maximum Temperature sec	Maximum Fuel Temperature °C
Explicit Numerical	0.081*	792.32
External Numerical (1 Channel Model)	0.064	695.51
External Numerical (2 Channel Model)	0.081	779.23
External Numerical (8 Channel Model)	0.123	761.47
RELAP5-3D Numerical (2 Channel Model)	0.055	751.65
RELAP5-3D Numerical (8 Channel Model)	0.085	733.15

Table 6.2 provides a summary of the results produced from the HEU Beginning of Life Normal Core for all solution methods considered. As a result of these solutions an average maximum fuel temperature of 738.86 °C at an average time of 0.076 sec, having standard deviations respectively of 47.43 °C and 0.025 sec is obtained.

6.2.3 Incorporating Moderator Feedback

By incorporating moderator feedback into the RELAP5-3D Numerical Solution there is potential for the maximum fuel temperature associated with a given reactivity insertion to be reduced from that without moderator feedback. Moderator feedback occurs as a result of having a negative moderator temperature coefficient and

* The External Numerical power trace was used to produce the External Explicit Solution therefore it is assumed that the time of maximum fuel temperature for the External Explicit Solution is the same as that of the External Numerical Solution.

moderator void coefficient. As a moderator increases in temperature, it decreases its efficiency in thermalizing neutrons by reducing their energy level from the fast or resonance energy spectrum down into the thermal energy spectrum where there is a greater probability that they will induce fission. Similar to moderator temperature coefficient, the moderator void coefficient is a result of a reduction in moderator density. As the density of the moderator decreases into a saturated state its scattering cross section greatly decreases, therefore decreasing the interaction probability of neutron to moderator and again decreasing the moderator's efficiency to thermalize neutrons.

Figure 6.4 presents the results of the change in reactivity as a function of time after incorporating moderator feedback into the RELAP5-3D model. The reactivity is identical for the case with and without moderator feedback. This is because there is not enough heat that is transferred into the moderator to affect its temperature or density within the extremely short time frame.

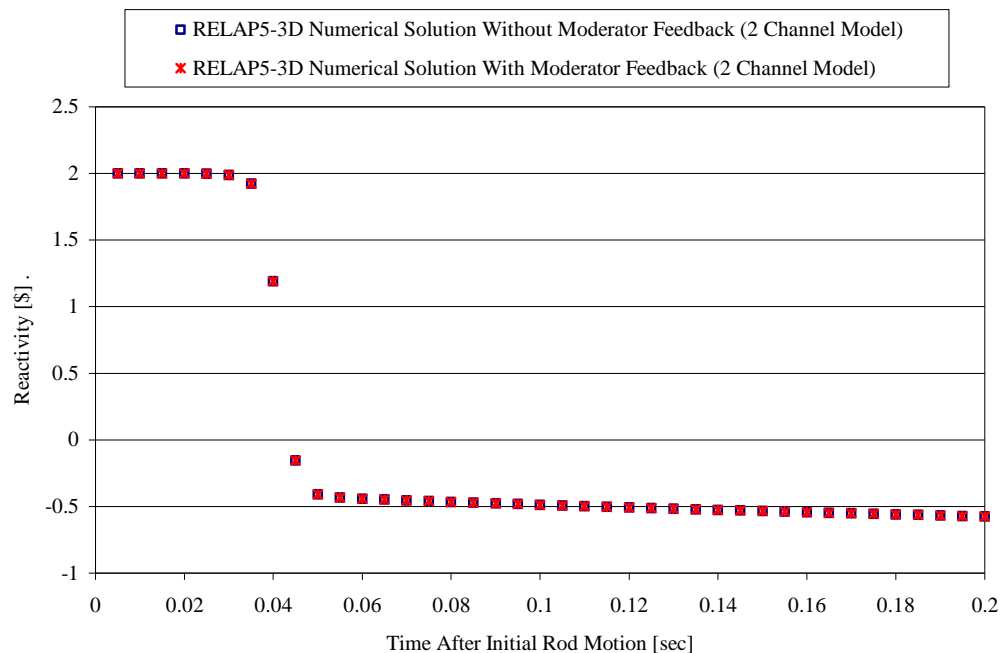


Figure 6.4: Transient Reactivity Comparison
(HEU Beginning of Life Normal Core)

7. CONCLUSION

Conducting a thermal hydraulic subchannel analysis can be done in many ways as discussed in Todreas & Kazimi [67] including:

- Isolated cell method (Single subchannel Analysis)
- Direct analytical solution of the multicell problem (Multichannel Analysis)
- Direct numerical solution of the multicell problem (Multichannel Analysis)
- Utilization of single-cell results by iterative or superposition procedures (Multichannel Analysis)

The two methods above analysed during this study include the direct numerical solution of the multicell problem and isolated cell method. As a result of this quantitative comparison using a single, two, and eight channel model developed in RELAP5-3D several conclusions can be drawn.

7.1 Steady State

Based on a conservative method for safety analysis, the single channel model provides critical heat flux results using the 2006 Groeneveld look-up tables within ~1.0 % of those produced from the eight channel model. The single channel model produced the most conservative results relative to the two and eight channel models.

The natural circulation flow rate, fuel temperature distribution, fuel element heat flux, and CHF were determined as a result of this thermal hydraulic analysis. The values produced for all parameters have been shown to be consistent with those from previous analyses of the OSTR found in the current SAR.

Although many parameters used in the single, two and eight channel model, including inlet and exit form losses and fuel/clad gap thickness are not definitively known parameters, it can be confidently stated that the result produced from all three models provides conservative realistic values consistent with observed OSTR operating data.

As a result of this quantitative steady state comparison of the single, two and eight channel model; the single channel model has been chosen and is used during the core conversion analysis of the Oregon State TRIGA[®] Reactor. The results presented in the Safety Analysis Report as part of the core conversion project are presented in Appendix A.

7.2 Pulse

Conclusions that can be drawn from the pulse study presented in Chapter 6 are:

- In order to calculate prompt maximum fuel temperature for a given reactivity insertion during a pulse no moderator feedback is necessary to be incorporated in the solution.
- Although a pulse transient is extremely stiff, a maximum fuel temperature for all seven cases considered (Table 6.2) produced a standard deviation of 47.43 °C. Considering that a single fuel element has ~220 MW-sec of energy being deposited in it over a period of ~0.05 sec the ability to define a maximum fuel temperature with a standard deviation of less than 50 °C is reasonable margin of error.

7.3 Future Work

The analysis presented herein supports the core conversion project and demonstrates that the OSTR with LEU core will continue to safely operate within existing specification limits.

More detailed studies should be undertaken to better quantify operating parameters, particularly for pulsed operation which may lead to reduced uncertainty and a

corresponding reduction in required margins to specification limits. These follow on studies could include:

- Using CFD code to identify subchannel cross flow
- Identifying the form loss coefficients associated with the lower and upper grid plate using a more refined method than was conducted during this study.
- Investigation toward an optimal pulse simulation methodology in order to economize resources during thermal hydraulic analyses.

BIBLIOGRAPHY

1. Leventhal, P. and A. Kuperman (1995) *RERTR At The Crossroads: Success or Demise*. Nuclear Control Institute Volume,
2. Argonne National Laboratory, *Reduced Enrichment for Research and Test Reactors*. 2007, Nuclear Engineering Division at Argonne.
3. Groeneveld, D.C., S.C.Cheng, and T. Doan, 1986 *AECL-UO Critical Heat Flux Lookup Table*. Heat Transfer Engineering, 1986. 7(1-2): p. 46-62.
4. Groeneveld, D.C., et al., *The 1995 look-up tables for critical heat flux in tubes*. Nuclear Engineering and Design, 1996. 1(23): p. 1-23.
5. Groeneveld, D.C., et al., *The 2006 CHF look-up table*. Nuclear Engineering and Design, 2007: p. 1-24.
6. Bernath, L., *A Theory of Local Boiling Burnout and Its Application to Existing Data*. Chem. Eng. Prog., Symp. Ser, 1960. 30(56): p. 95-116.
7. McAdams, W.H., *Heat Transmission*. 3 ed, ed. 3. 1954, New York: McGraw-Hill. 532.
8. McAdams, W.H., et al., *Heat Transfer at High Rates to Water with Surface Boiling*. Industrial and Engineering Chemistry, 1949. 41(9): p. 1945-1953.
9. Feltus, M.A. and W.S. Miller, *Three-dimensional coupled kinetics/thermal-hydraulic benchmark TRIGA experiments*. Annals of Nuclear Energy, 2000. 27: p. 771-790.
10. Bene, D., *Appendix A: Evaluation of Inlet/Outlet Loss Coefficients*. 2007, General Atomics.
11. Tong, L.S. and Y.S. Tang, *Boiling heat transfer and two-phase flow*. 2 ed. Chemical and Mechanical Engineering, ed. G.F. Hewitt and C.L. Tien. 1997, Washington D.C.: Taylor & Francis.
12. Bergles, A.E. and W.M. Rohsenow, *The Determination of Forced Convection Surface Boiling Heat Transfer*. Trans. ASME, J. Heat Transfer, 1964. 4(86): p. 365-372.
13. Davis, E.J. and G.H. Anderson, *The Incipience of Nucleate Boiling in Forced Convection Flow*. AIChE J., 1966. 4(12): p. 774-780.

14. Churchill, S.W. and H.H.S. Chu, *Correlating Equations for Laminar and Turbulent Free Convection From a Vertical Plate*. International Journal of Heat and Mass Transfer, 1975. 18: p. 1323-1329.
15. McAdams, W.H., W.H. Woods, and R.L. Bryan, *VapORIZATION Inside Horizontal Tubes*. Trans. ASME, 1941. 63(1): p. 545-552.
16. Grigoriadis, D., et al. *Thermal Hydraulic Calculations for the Conversion to LEU of a Research Reactor Core*. in *2007 RERTR International meeting on Reduced Enrichment For Research and Test Reactors*. 2007. Prague, Czech Republic: Argonne National Laboratory.
17. Nelson, R.C., et al. *Thermal-Hydraulic Transient Analysis of the Missouri University Research Reactor*. in *Test, Research & Training Reactors 2007 Conference*. 2007. Newport Oregon.
18. Weaver, W., et al., *A Generic Semi-Implicit Coupling Methodology for use in RELAP5-3D*. Nuclear Engineering and Design, 2002. 211: p. 13-26.
19. Hainoun, A. and A. Schaffrath, *Simulation of Subcooled Flow Instability for High Flux Research Reactors Using the Extended Code ATHLET*. Nuclear Engineering and Design, 2000. 207: p. 163-180.
20. Huda, M.Q. and S.I. Bhuiyan, *Investigation of Thermohydraulic Parameters During Natural Convection Cooling of TRIGA Reactor*. Annals of Nuclear Energy, 2006. 33: p. 1079-1086.
21. Huda, M.Q. and M. Rahman, *Thermo-Hydrodynamic Design and Safety Parameter Studies of the TRIGA MARK II*. Annals of Nuclear Energy, 2004. 31: p. 1101-1118.
22. RELAP5-3D Team., *Volume I: code structure, system models, and solution methods*, in *RELAP5-3D code manual*. 2005, Idaho National Laboratory: Idaho Falls, Idaho. p. 600.
23. Bousbia-Salah, A., et al., *Assessment of RELAP5 Model for the University of Massachusetts Lowell Research Reactor*. Nuclear Technology & Radiation Protection, 2006. 21: p. 3-12.
24. Lang, C., *Transactions of Institute of Engineers and Shipbuilders*. Scotland, 1888. 32: p. 279-295.
25. Nukiyama, S., *The maximum and minimum values of the heat Q transmitted from metal to boiling water under atmospheric pressure*. International Journal of Heat and Mass Transfer, 1966. 9: p. 1419-1433.

26. Bonilla, C.F. and C.W. Perry, *Heat transmission to boiling binary liquid mixtures*. Transactions of American Society of Chemical Engineers, 1941. 37: p. 685-705.
27. Cichelli, M.T. and C.F. Bonilla, *Heat transfer to liquids boiling under pressure*. Transactions of American Society of Chemical Engineers, 1945. 41: p. 755-787.
28. Kutateladze, S.S., *A hydrodynamic theory of changes in a boiling process under free convection*. Izvestia Akademia Nauk, S.S.S.R., Otdelenie Tekhnicheskii Nauk, 1951. 4: p. 529.
29. Kutateladze, S.S., *On the transition to film boiling under natural convection*. Kotloturbostroenie, 1948. 3: p. 10-12.
30. Rohsenow, W.M. and P. Griffith, *Coorelation of maximum heat transfer data for boiling of satuurated liquids*. Chem. Eng. Prog., Symp. Ser, 1956. 52: p. 47.
31. Zuber, N., *Hydrodynamic aspects of boiling heat transfer*, in *Research Laboratory*. 1959, University of California: Los Angeles, CA.
32. Costello, C.P. and W.J. Frea, *A salient non-hydrodynamic effect on pool boiling burnout of small semi-cylindrical heters*. AIChE Chemical Engineering Progress Symposium Series, 1963. 61(57): p. 258-268.
33. Gaertner, G.F., *Effect of heater surface chemistry on the level of burnout heat flux in pool boiling*, in *Technical Information Serie*. 1963, General Electric Research Laboratory: Schenectady, New York.
34. Gaertner, R.F., *Photographic study of nucleate pool boiling on a horizontal surface*. ASME J. Heat Transfer, 1965. 87: p. 17-29.
35. Katto, Y. and S. Yokoya, *Principal mechanism of boiling crisis in pool boiling*. International Journal of Heat and Mass Transfer, 1968. 11: p. 993-1002.
36. Lienhard, L.H. and V.K. Dhir, *Extended hydrodynamic theory of peak and minimum pool boiling heat fluxes*, in *NASA CR-2270*. 1973, NASA.
37. Haramura, Y. and Y. Katto, *New hydrodynamic model of critical heat flux applicable widely to both pool and forced convection boiling on submerged bodies in saturated liquids*. International Journal of Heat and Mass Transfer, 1983. 26: p. 379-399.

38. Liaw, S.P. and V.K. Dhir. *Effect of surface wettability on transition boiling heat transfer from a vertical surface*. in *Proceedings of the Eighth International Heat Transfer Conference*. 1986. Sanfransisco, CA.
39. Ramilison, J.M. and J.H. Lienhard, *Transition boiling heat transfer and the film transition regime*. ASME J. Heat Transfer, 1987. 109: p. 746-752.
40. Elkassabgi, Y. and J.H. Lienhard, *Influence of subcooling on burnout of horizontal cylindrical heaters*. ASME J. Heat Transfer, 1988. 110: p. 479-486.
41. Dhir, V.K. and S.P. Liaw, *Framework for a unified model for nucleate and transition pool boiling*. ASME J. Heat Transfer, 1989. 111: p. 3739-3746.
42. Sakurai, A. and M. Shiotsu. *Temperature-controlled pool-boiling heat transfer*. in *Proceedings of the Fifth International Heat Transfer Conference*. 1974.
43. Kandlikar, S.G., *A theoretical model to predict pool boiling CHF incorporating effects of contact angle and orientation*. Journal of Heat Transfer, 2001. 123: p. 1071-1079.
44. Moon, S., et al., *An experimental study on the critical heat flux for low flow of water in a non-uniformly heated vertical rod bundle over a wide range of pressure conditions*. Nuclear Engineering and Design, 2005. 235: p. 2295-2309.
45. Katto, Y. and S. Kawamura, *Critical heat flux during natural convective boiling in vertical uniformly heated tubes submerged in saturated liquid*. Trans. JSME, B Ser., 1981. 47: p. 2186-2190.
46. Monde, M. and K. Yamaji, *Critical heat flux during natural convective boiling in a vertical uniformly heated tubes submerged in saturated liquid*. Heat Transfer, 1990. 112: p. 111-116.
47. Monde, M. and Y. Mitsutake, *Critical heat flux during natural convective boiling in a vertical tube: effect of oscillation and circulation on CHF*. International Journal of Heat and Mass Transfer, 2002. 45: p. 4133-4139.
48. Katto, Y., *Correlations for critical heat flux of natural convective boiling in confined channels*. Trans. JSME, B Ser., 1978. 44: p. 3908-3911.
49. Unal, C., K. Tuzla, and O. Badr, *Parametric trends for post CHF heat transfer in rod bundles*. Journal of Heat Transfer, 1988. 110: p. 728-734.
50. Vishner, I.P., *Nucleate boiling in criticals of helium in vertical channels with natural convection boiling*. Heat Transfer Soviet Res., 1974. 6: p. 170-176.

51. Fujita, Y., H. Ohta, and S. Uchida, *Nucleate boiling heat transfer and critical heat flux in narrow space between rectangular surfaces*. International Journal of Heat and Mass Transfer, 1988. 31: p. 229-239.
52. Xia, C., W. Hu, and Z.Y. Guo, *Natural convection boiling in vertical rectangular narrow channels*. Exp. Therm. Fluid Sci., 1996. 12: p. 313-324.
53. Monde, M., Y. Mitsutake, and M. Hayashi, *Critical heat flux during natural circulation boiling on uniformly heat outer tube in vertical annular tubes submered in saturated liquid*. International Journal of Heat and Mass Transfer, 1999. 42: p. 3189-3194.
54. Chyu, M.C., *Prediction of boiling dry out flux for restricted annular crevice*. International Journal of Heat and Mass Transfer, 1998. 31: p. 1993-1998.
55. Henry, R.E. and H.K. Fauske, *External cooling of a reactor vessel under severe accident conditions*. Nuclear Engineering and Design, 1993. 139: p. 3-43.
56. Liu, Z.H. and Y.M. Chen, *Study of critical heat flux during natural convective boiling in vertical annular tubes submerged in saturated liquids*. JSME Int. J. Fluids Therm. Eng. Des., 1999. 199: p. 41-48.
57. Reddy, D.G. and C.F. Fighetti, *Parametric study of CHF data, vol. 2. A generalized subchannel CHF correlation for PWR and BWR fuel assemblies*, in EPRI Report. 1983.
58. Macbeth, R.V., *Burn-out analysis. Part 4. Application of a local condition hypothesis to world data for uniformly heated round tubes and rectangular channels*, in UKAEA Report. 1963: Winfrith.
59. Lee, C.S., et al., *A feasibility study on the extended cycle from the point of view of non-LOCA safety analysis*, in KAERI Report. 1996.
60. V., R., *Burn-out analysis. Part 4. Application of local condition hypothesis to world data for uniformly heated round tubes and rectangular channels*, in UKAEA Report. 1963: Winfrith.
61. Biasi, L., et al., *Studies on burnout. part 3 - a new correlation for round ducts and uniform heating and its comparison with world data*. Energia Nucl., 1967. 14: p. 530-537.
62. Anderson, T.V., *Oregon State TRIGA Reactor Training Manual*. 1990.
63. General Atomics Corp., *Reactor Tank Details, TRIGA Mark III*, General Atomics. p. Dwg #: S-6.

64. General Atomics Corp., *Top Grid Plate, TRIGA Mark III*, General Atomics. p. Dwg #: T13S210J106s.
65. Oregon State University, *SAFETY ANALYSIS REPORT FOR THE CONVERSION OF THE OREGON STATE TRIGA® REACTOR FROM HEU TO LEU FUEL*. 2007, Oregon State University.
66. Simnad, M., *The U-ZRHx Alloy: ITS PROPERTIES AND USE IN TRIGA FUEL*. Nuclear Engineering and Design, 1980. 64(November): p. 403-422.
67. Todreas, N.E. and M.S. Kazimi, *Nuclear systems II: Elements of Thermal Hydraulic Design*. Vol. 2. 2001, New York: Taylor & Francis Group, LLC. 506.
68. RELAP5-3D Team, *Volume IV: Models and Correlations*, in *Code Manual*, R.-D.C. Team, Editor. 2004, Idaho National Laboratory: Idaho Falls, Idaho.
69. *Oregon State University TRIGA Training Manual*. 2004.
70. General Atomics Corp., *Reflector Assembly, Oregon*: General Atomics. p. Dwg # T2D210J110-A.
71. *Guide to the selection of the surface finish of stainless steel on fabricated items*, in *SHAPA Technical Bulliten No. 1*. 2000.
72. White, F., *Fluid Mechanics*. Fifth ed. 2003: McGraw-Hill Higher Education.
73. Todreas, N.E. and M.S. Kazimi, *Nuclear systems I: Thermal Hydraulic Fundamentals*. Vol. 1. 1990, New York: Taylor & Francis Group, LLC. 705.
74. General Atomics Corp., *Safety Evaluation Report on High-Uranium Content, Low-Enriched Uranium-Zirconium Hydride Fuels for TRIGA Reactors*, in *NUREG-1282*. 1987, U.S. Nuclear Regulatory Commission.
75. Simnad, M., F. Foushee, and G. West, *Fuel elements for pulsed TRIGA Research Reactors*. 1975, General Atomics: Sandiego, CA.
76. General Atomics Corp., *Safety Analysis for the HEU to LEU Core Conversion of the Washington State University Reactor*, N.R. Commission, Editor. 2007, General Atomics: TRIGA Reactors Division of General Atomics-ESI. p. 1-112.
77. Dunn, F.E., et al. *MNSR Transient Analyses and Thermal Hydraulic Safety Margins for HEU and LEU Cores Using RELAP5-3D Code*. in *2007 International Meeting on Reduced Enrichment for Research and Test Reactors*. 2007. Prague, Czech Republic.

78. Duderstadt, J.J. and L.J. Hamilton, *Nuclear Reactor Analysis*. 1976, Ann Arbor, Michigan: Wiley-Interscience. 650.

NOMENCLATURE

α_T	Prompt fuel temperature coefficient	q_{cr}	Critical heat flux
β	Delayed neutron fraction	r	Radial position
Δ	“slope”	T	Fuel temperature
ΔP	Pressure difference	T_b	Fluid bulk temperature
λ	Decay constant	T_{bulk}	Fluid bulk temperature
Λ	Mean neutron generation	T_{sat}	Fluid saturation temperature
ρ	Fluid Density, Reactivity	$T_{w_{BO}}$	Wall temperature at CHF
σ	Liquid-gas interface tension	v	Fluid velocity
A_{fi}	Subchannel flow area	X_e	Equilibrium Quality
$A_{H.S.}$	Heated Surface Area	z	Axial Position
C	Neutron precursor concentration	AFCR	Air Followed Control Rod
C_p	Specific heat	CHF	Critical heat flux
D	Fuel element outer diameter	CHFR	Critical Heat Flux Ratio
D_h	Hydraulic Diameter	CLICIT	Cadmium Lined In Core Irradiation Tube
D_H	Heated Diameter	DNB	Departure from nucleate boiling
f	Power distribution function	FFCR	Fuel Followed Control Rod
G	Mass flux	FLIP	Fuel Lifetime Improvement Plan
h	Enthalpy	HEU	Highly enriched uranium
h_{BO}	Film coefficient of heat transfer	ICIT	In Core Irradiation Tube
h_f	Subcooled enthalpy	INL	Idaho National Laboratory
h_g	Superheated enthalpy	LEU	Low enriched uranium
h_{fg}	Latent heat	MCHFR	Minimum Critical Heat Flux Ratio
K	Form loss, Thermal Conductivity	NRC	Nuclear Regulatory Commission
L	Axial nodal length	OSTR	Oregon State TRIGA [®] Reactor
L_h	Heated Length	RERTR	Reduced Enrichment for Research and Test Reactors
n_l	Lower nodal number	PRKE	Point Reactor Kinetics Equations
n_u	Upper nodal number	PRKM	Point Reactor Kinetics Model

P	Fuel element pitch, Thermal Power	SAR	Safety Analysis Report
P_a	Pressure, absolute	TRIGA	Transient Research Isotope General Atomics
P_{abs}	Pressure, absolute		
PF	Power factor		

APPENDICES

A APPENDIX (Single Channel Results)

A.1 Power Summary

A.1.1 HEU Power Summary

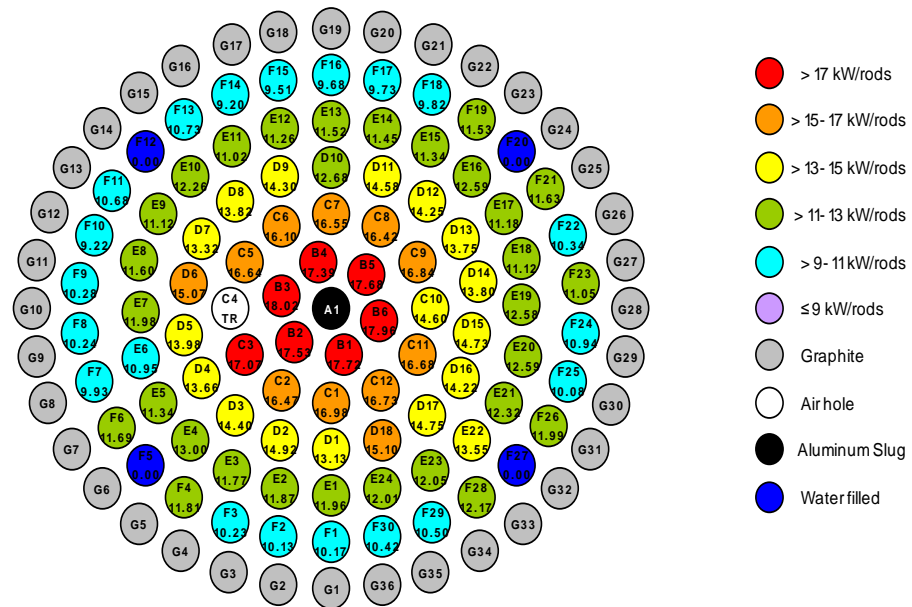


Figure A.1: Core Power Distribution (HEU Beginning of Life Normal Core) [65]

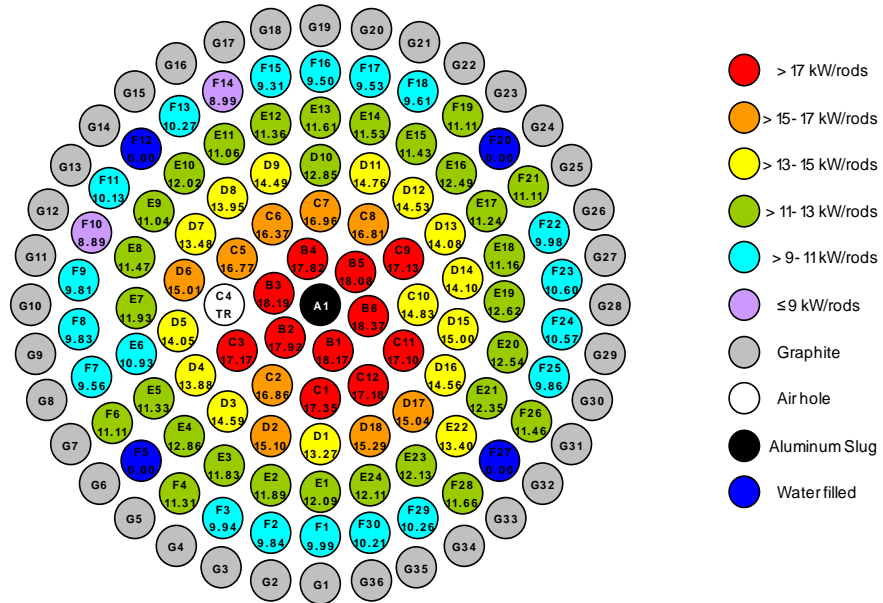


Figure A.2: Core Power Distribution (HEU Middle of Life Normal Core) [65]

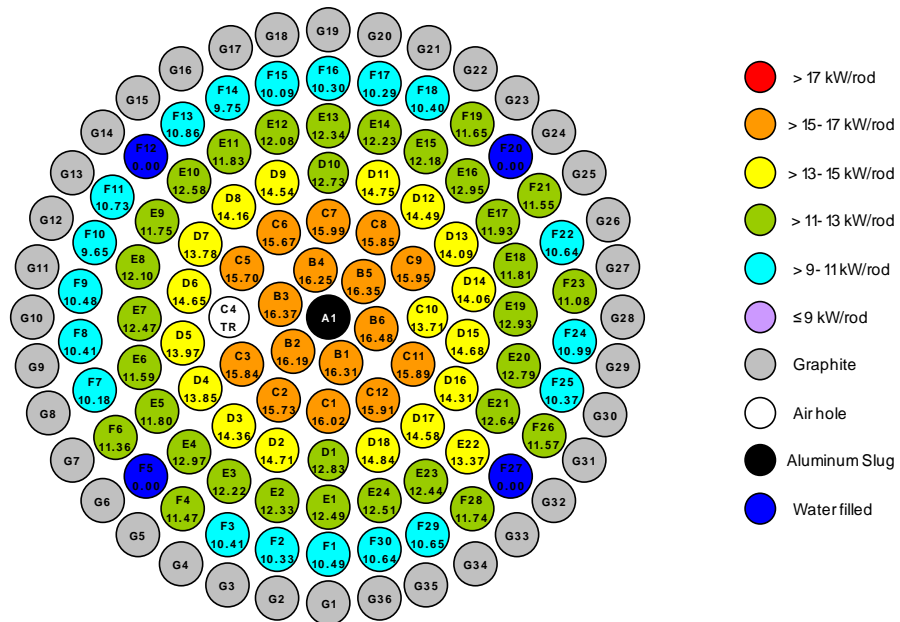


Figure A.3: Core Power Distribution (HEU End of Life Normal Core) [65]

All intra-fuel rod power profiles in the conversion analysis are representative of the hottest rod in the core for the given core configuration. There are 84 FLIP fuel Elements in the initial HEU core including the three control rod fuelled followers. The hot-rod peak factor is 1.376 which corresponds to a hot rod power of 18.02 kW (see Table 3.3) in the 1.1 MW_{th} steady state HEU Beginning of Life Normal Core.

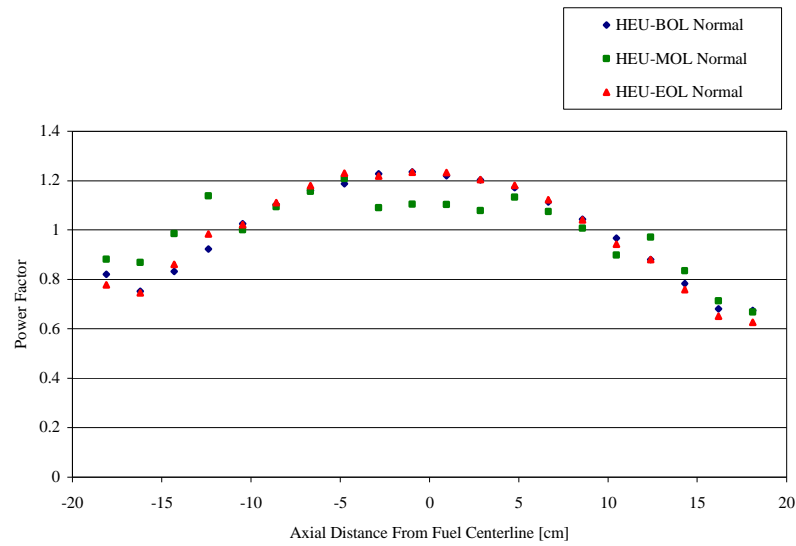


Figure A.4: HEU Normal Core - Axial Power Profile vs. Distance from Fuel Centerline

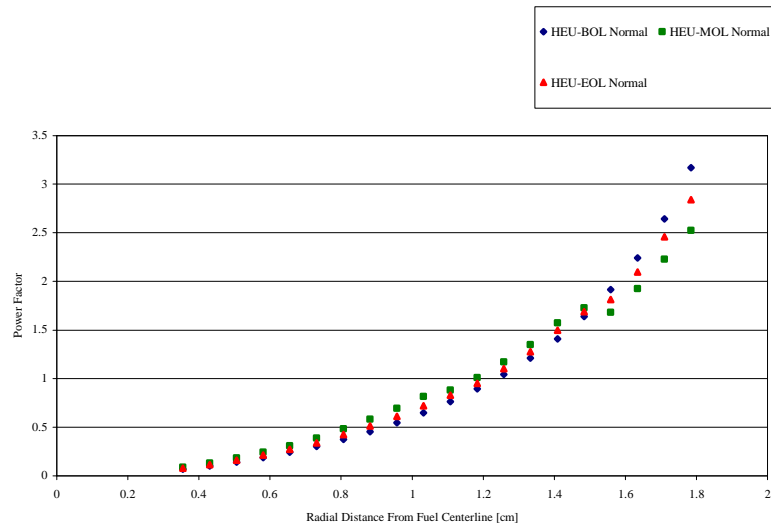


Figure A.5: HEU Normal Core-Radial Power Profile vs. Distance from Fuel Centerline

A.1.2 LEU Power Summary

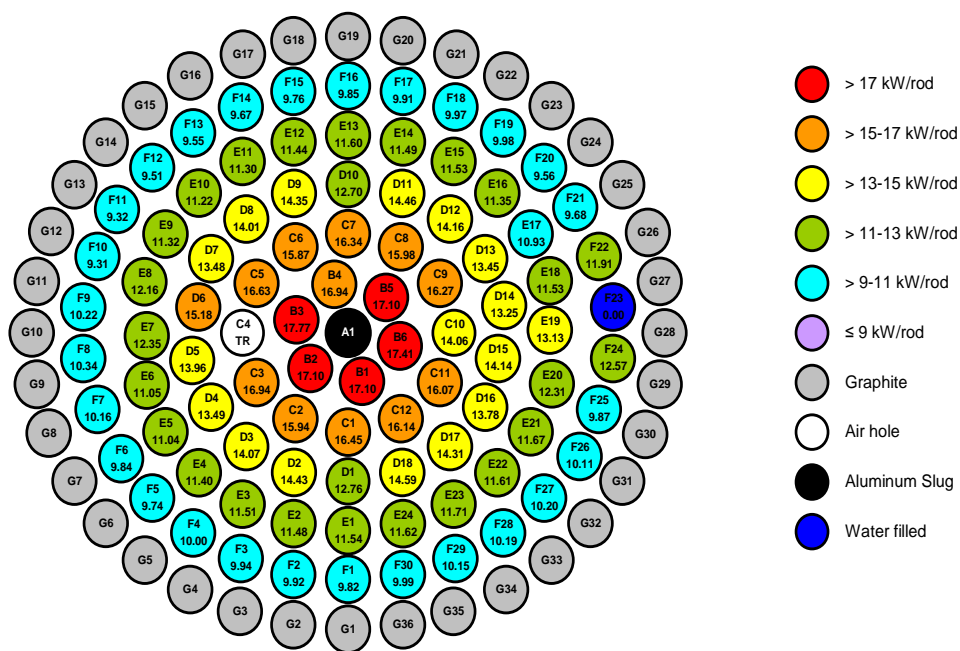


Figure A.6: Core Power Distribution (LEU Beginning of Life Normal Core) [65]

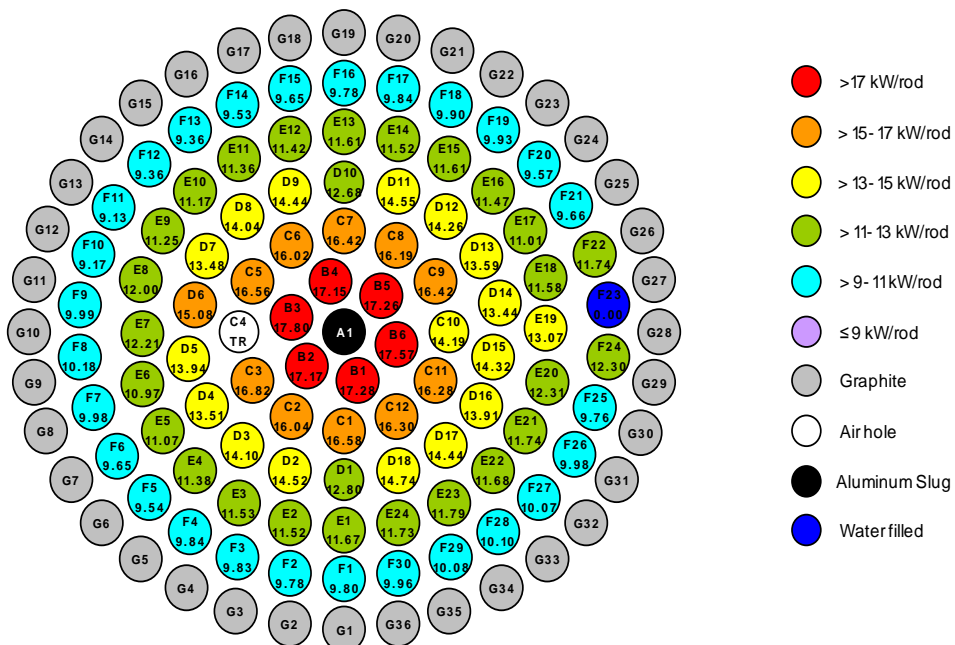


Figure A.7: Core Power Distribution (LEU Middle of Life Normal Core) [65]

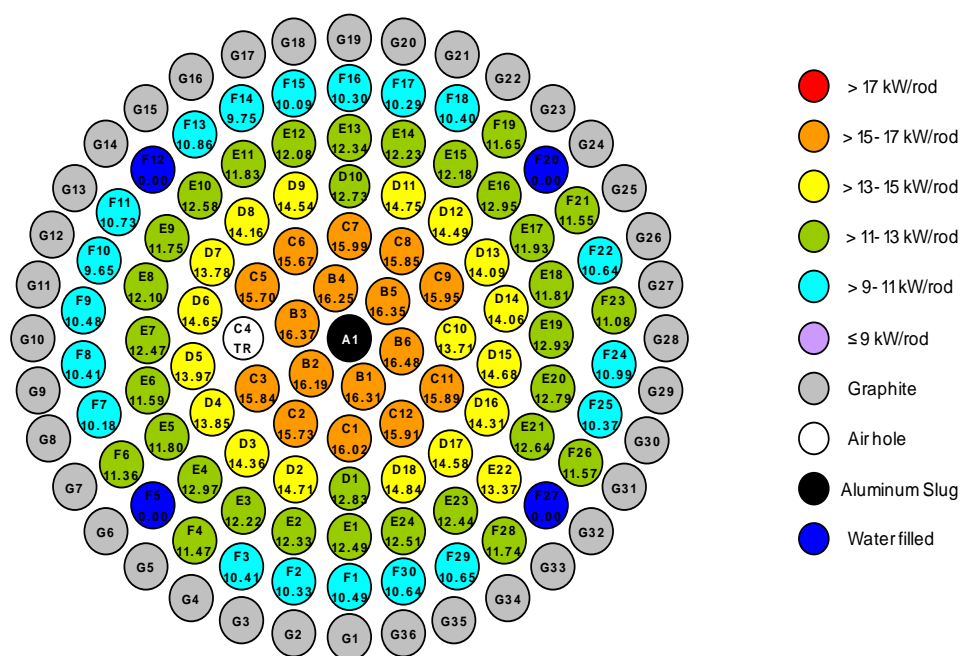


Figure A.8: Core Power Distribution (LEU End of Life Normal Core) [65]

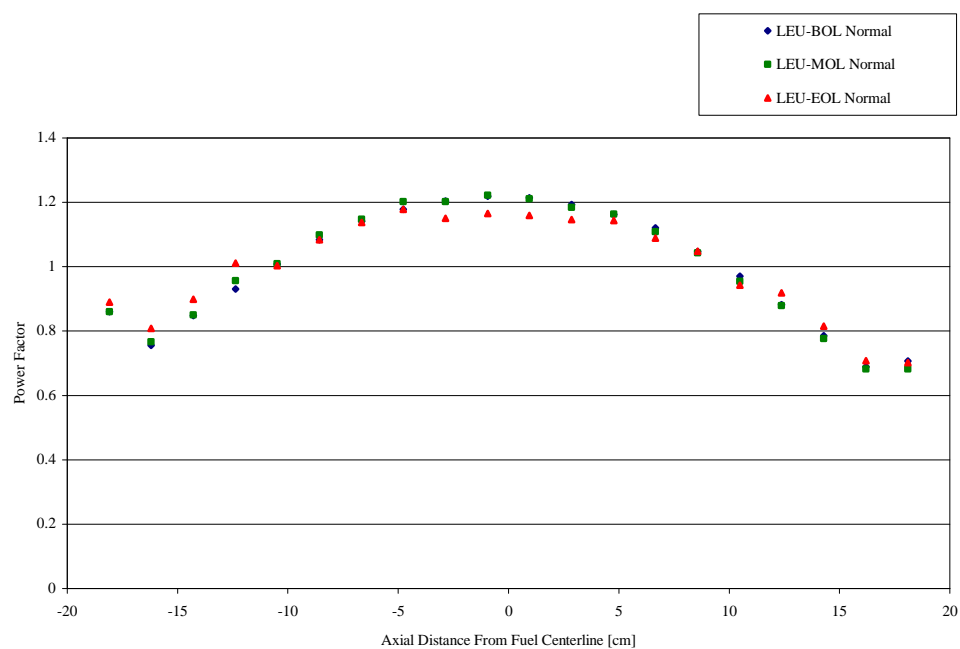


Figure A.9: LEU Normal Core-Axial Power Profile vs. Distance from Fuel Centerline

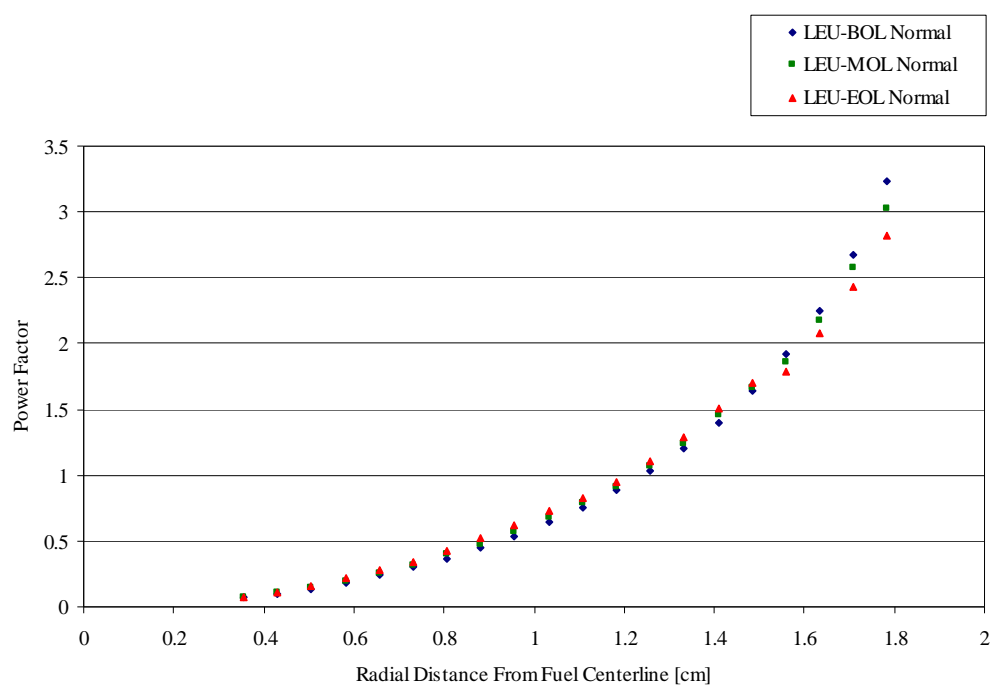


Figure A.10: LEU Normal Core-Radial Power Profile vs. Distance from Fuel Centerline

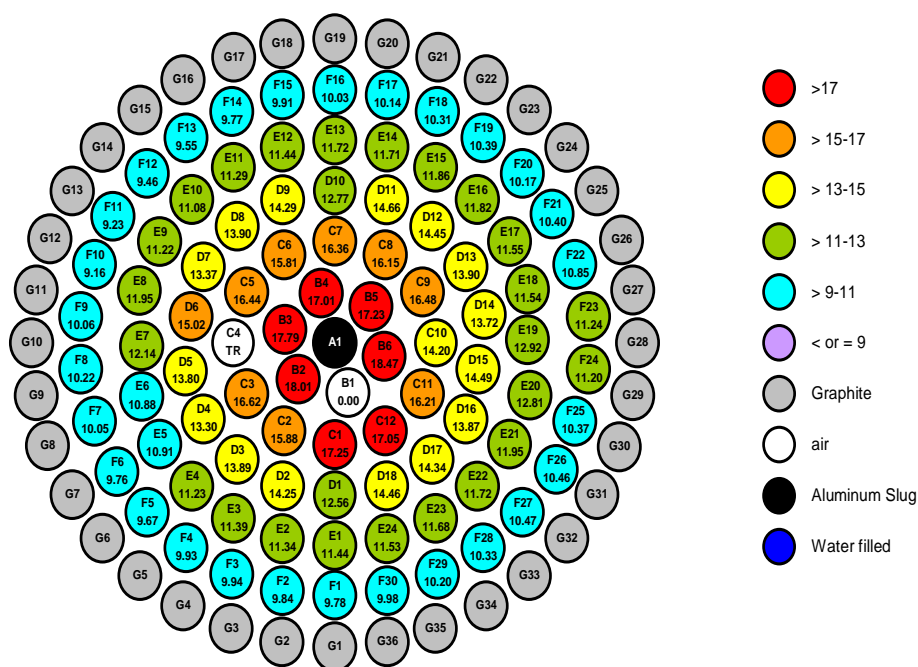


Figure A.11: Core Power Distribution (LEU Beginning of Life ICIT Core) [65]

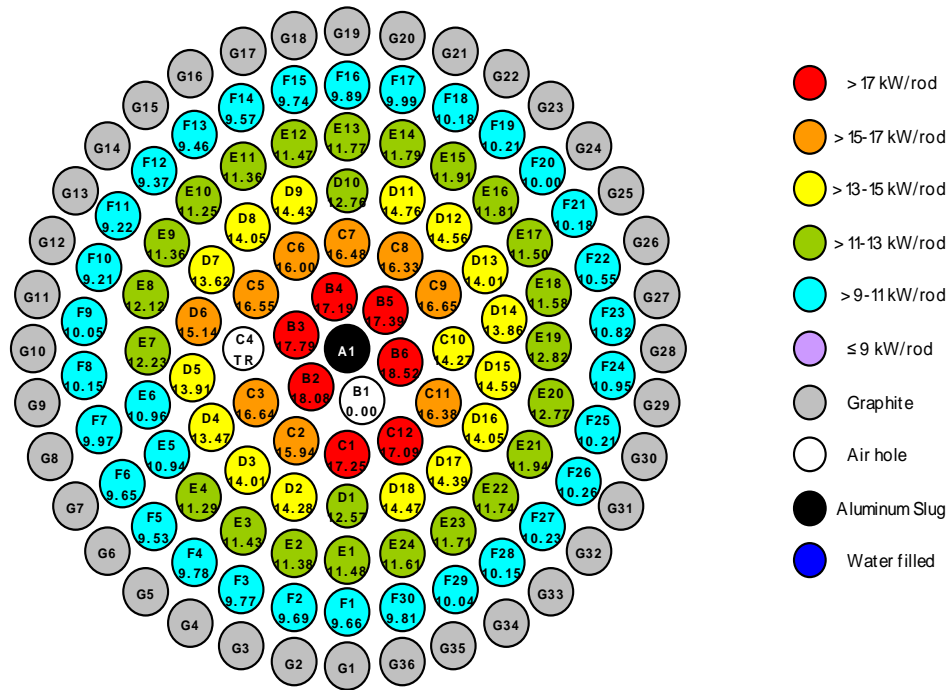


Figure A.12: Core Power Distribution (LEU Middle of Life ICIT Core) [65]

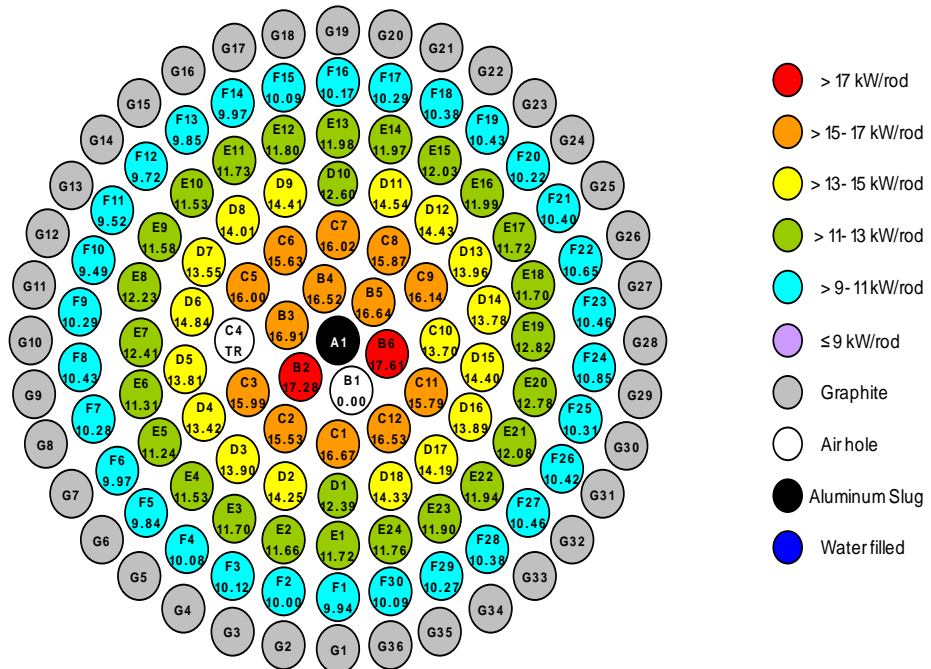


Figure A.13: Core Power Distribution (LEU End of Life ICIT Core) [65]

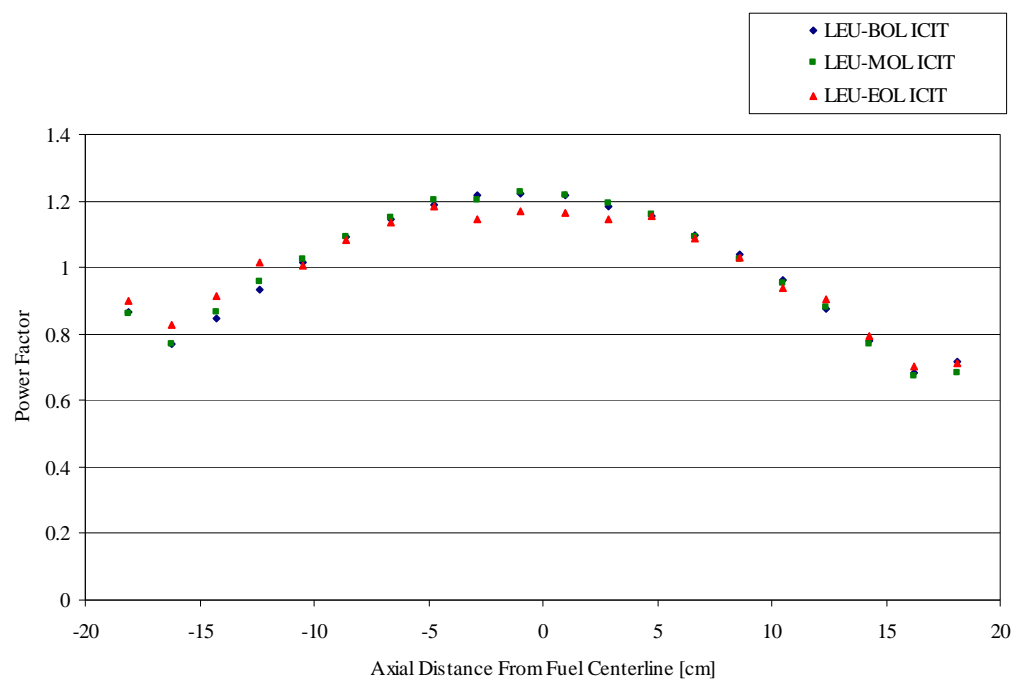


Figure A.14: Axial Power Factor (LEU ICIT Core)

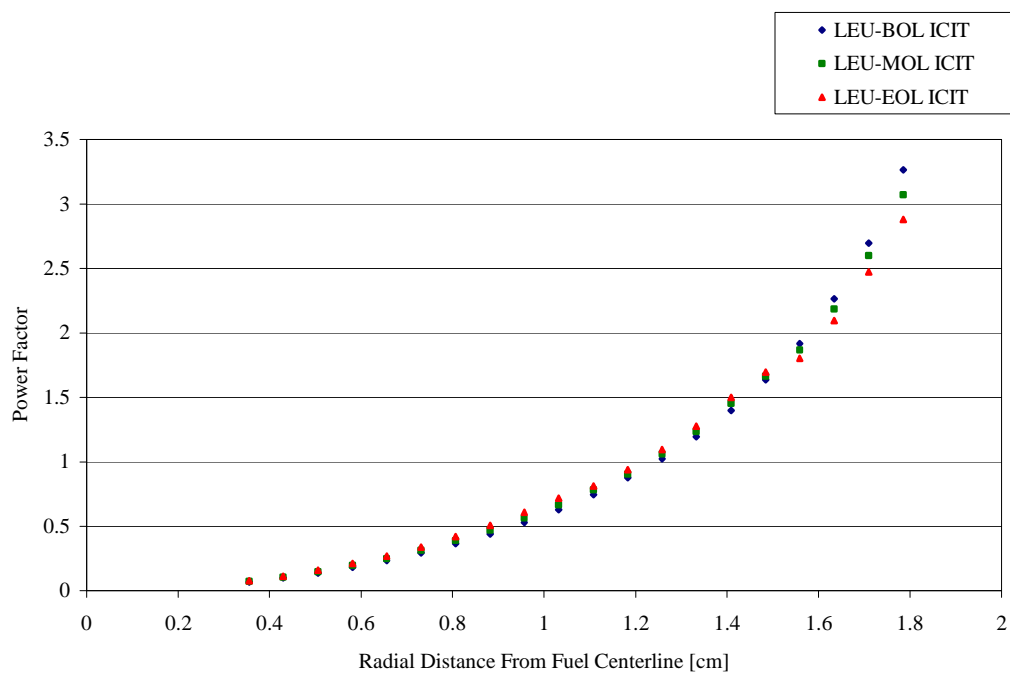


Figure A.15: Radial Power Factor (LEU ICIT Core)

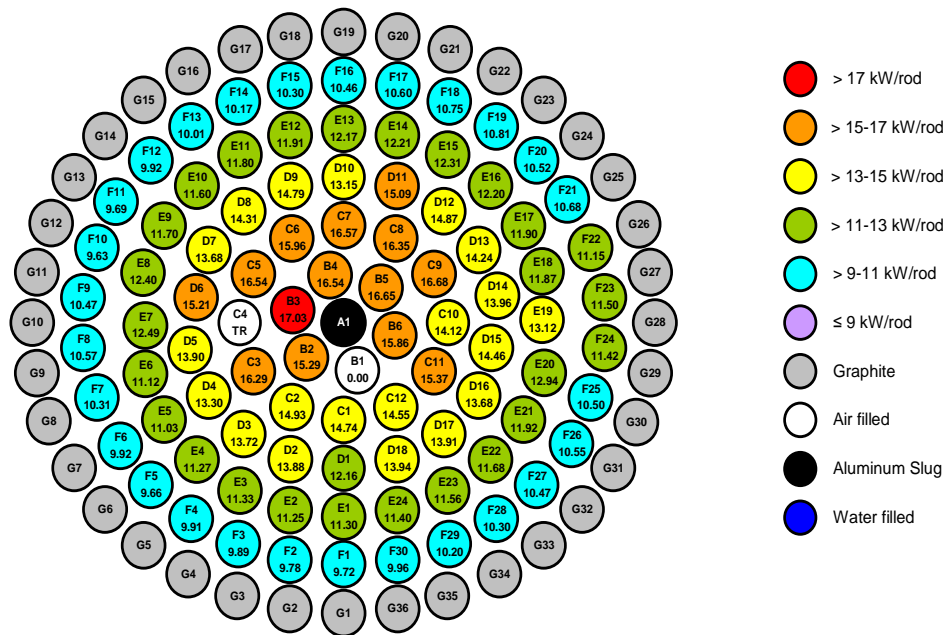


Figure A.16: Core Power Distribution (LEU Beginning of Life CLICIT Core) [65]

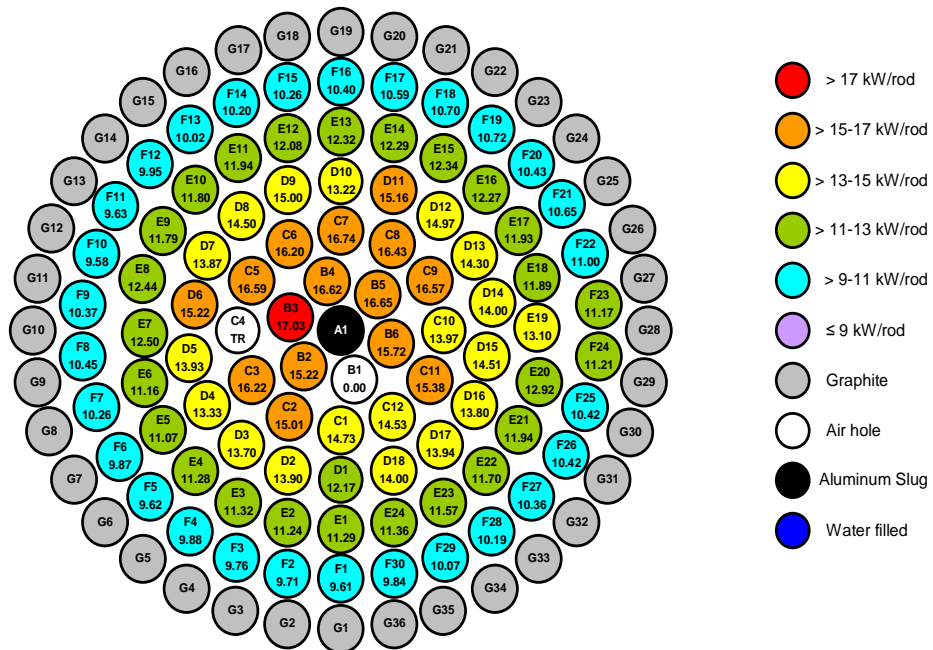


Figure A.17: Core Power Distribution (LEU Middle of Life CLICIT Core) [65]

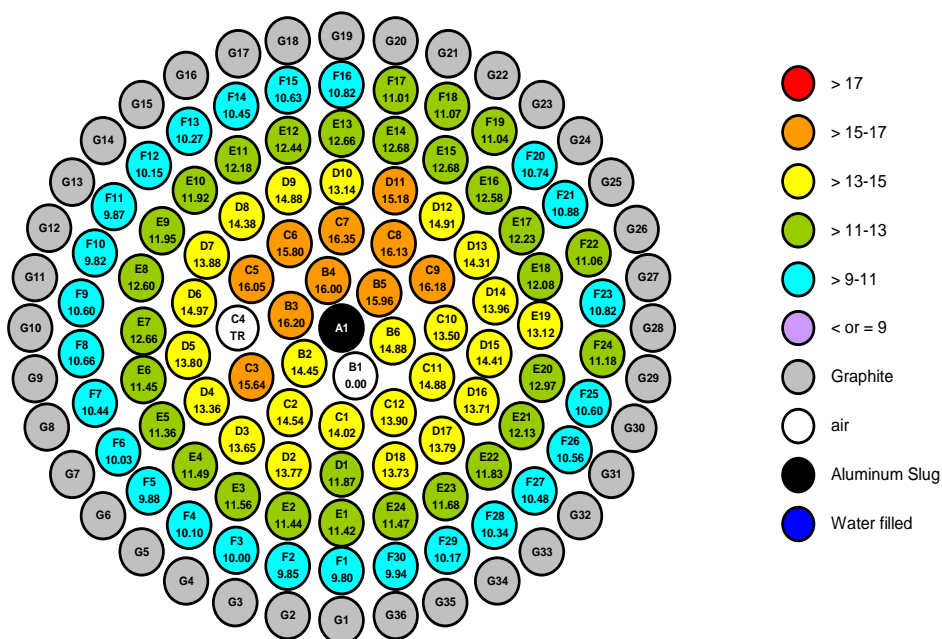


Figure A.18: Core Power Distribution (LEU End of Life CLICIT Core) [65]

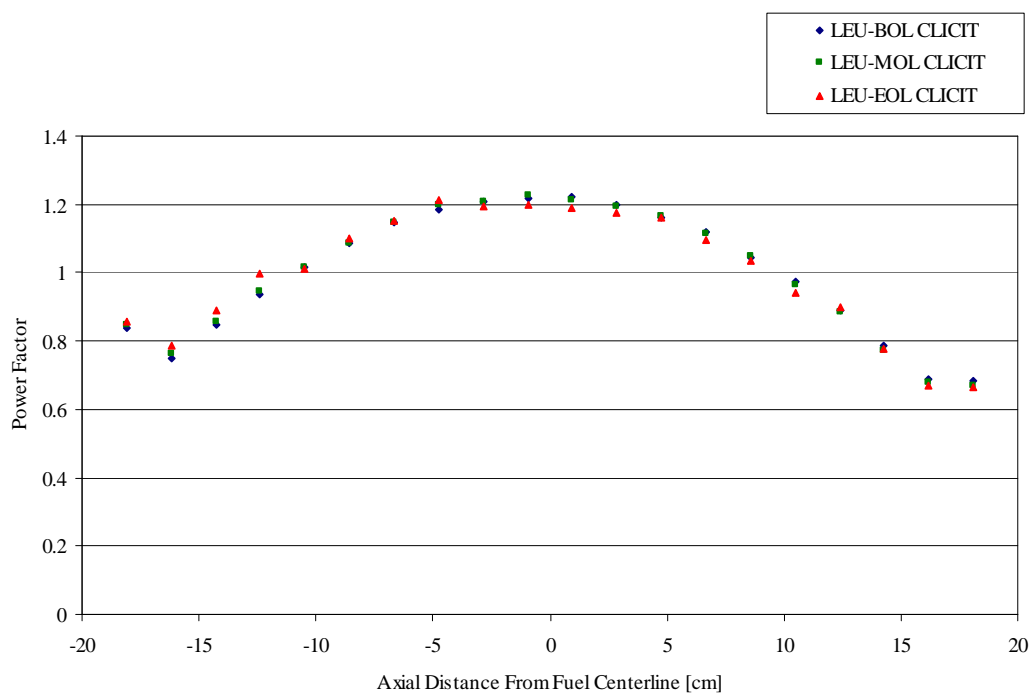


Figure A.19: Axial Power Factor (LEU CLICIT Core)

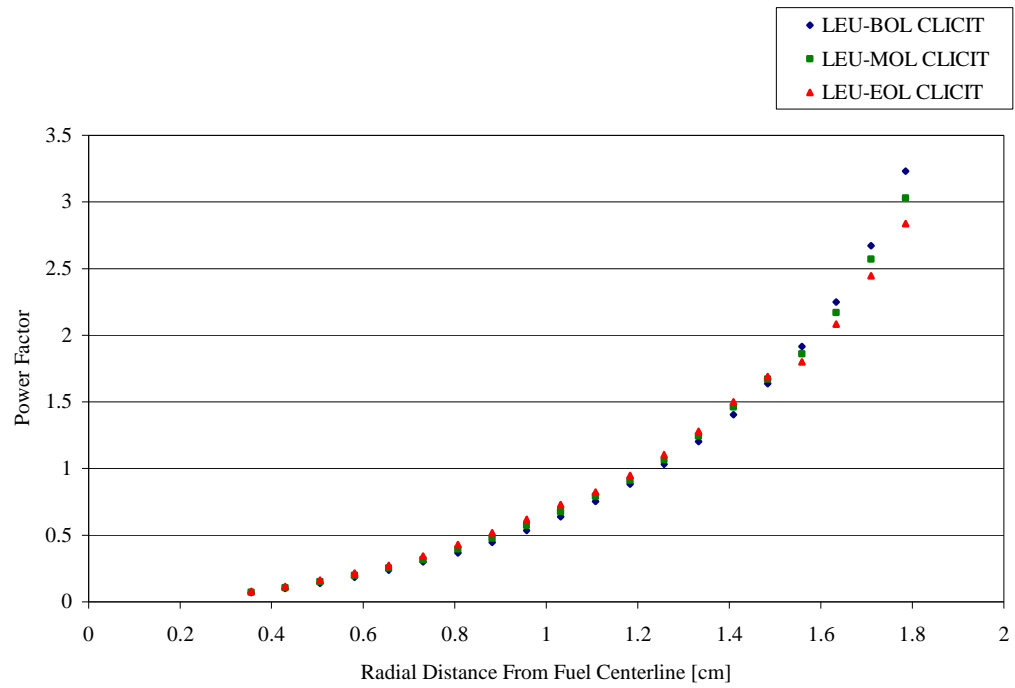


Figure A.20: Radial Power Factor (LEU CLICIT Core)

A.2 Steady State Results

A.2.1 HEU Beginning of Life Normal Core

Table A.1: Steady State Results of OSU HEU Beginning of Life Normal Core

Parameter	Value
Flow rate for hottest rod [kg/s]	0.0825
Maximum flow velocity [m/s]	0.2249
Maximum wall heat flux [kW/m ²]	498.28
Maximum fuel centerline temperature [°C]	447.60
Maximum clad temperature [°C]	131.27
Exit clad temperature [°C]	125.64
Exit bulk coolant temperature [°C]	101.18
MDNBR [Groeneveld 2006, Bernath]	4.844, 2.104

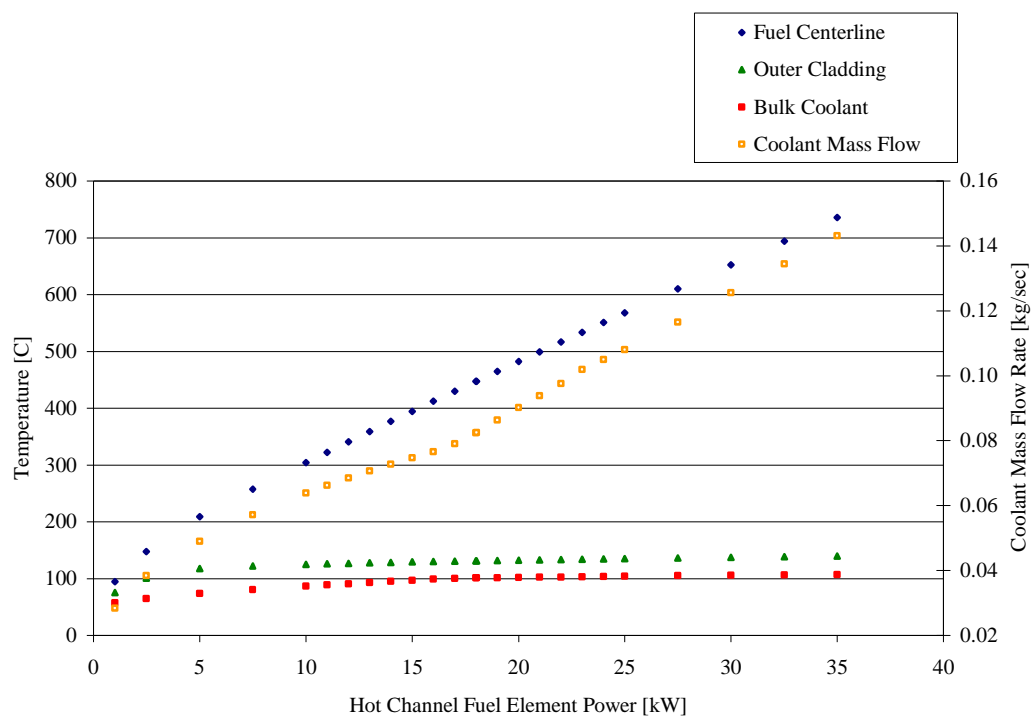


Figure A.21: Hot Channel Properties (HEU Beginning of Life Normal Core)

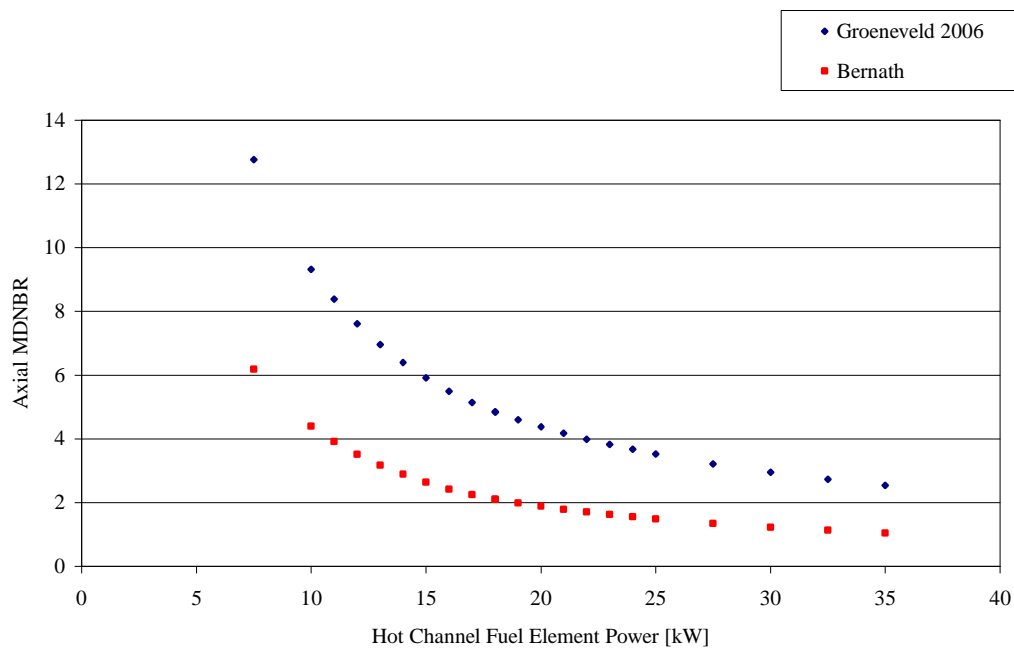


Figure A.22: Hot Channel MDNBR (HEU Beginning of Life Normal Core)

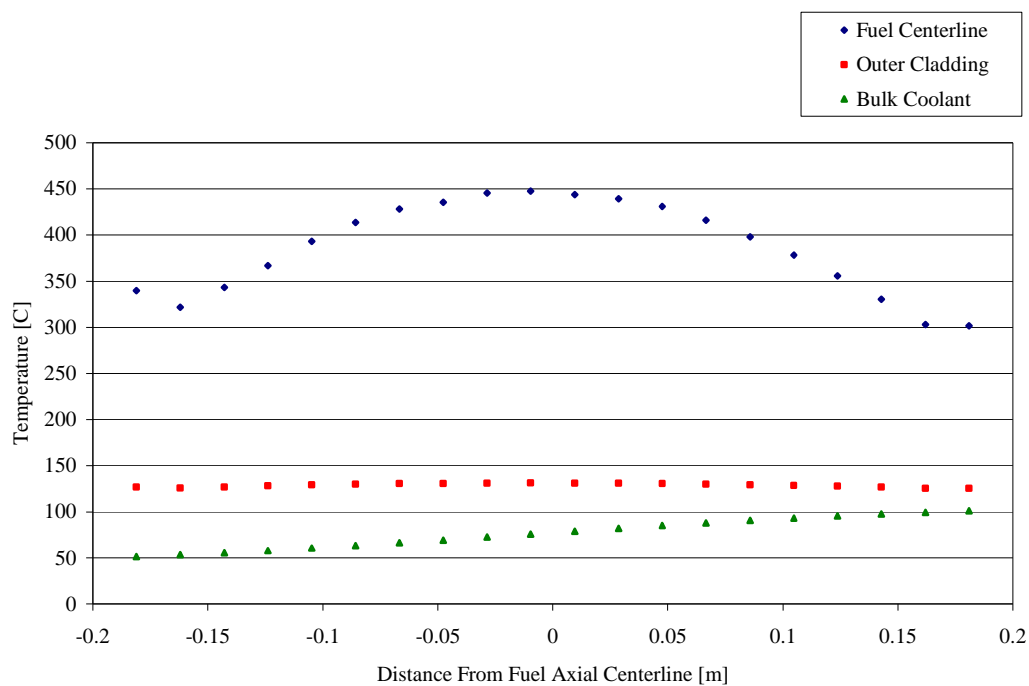


Figure A.23: Axial Temp. Distribution at 18.02 kW (HEU Beginning of Life Normal Core)

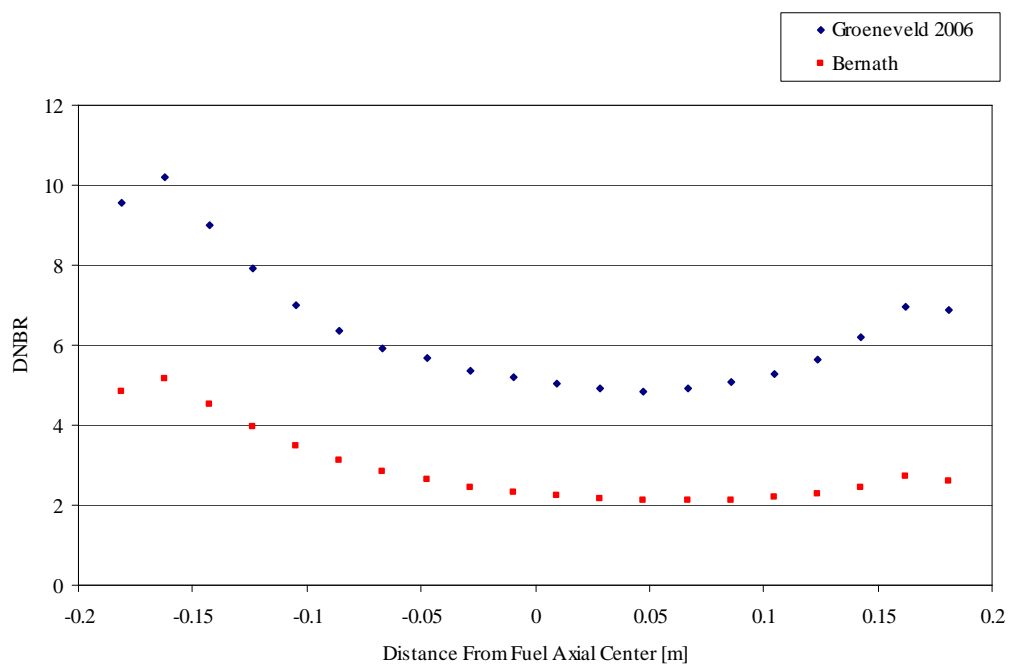


Figure A.24: Axial DNBR at 18.02 kW (HEU Beginning of Life Normal Core).

At 1.1 MW_{th}, the HEU Beginning of Life Normal core has a corresponding 18.02 kW hot rod in the B3 position. For the HEU Beginning of Life core at a power of 1.0 MW_{th}, the temperature measured at the IFE (B1 position) ranged from 356°C to 373°C. Predicted IFE power at 1.0 MW_{th} is $17.39(1.0/1.1) = 15.81$ kW. A RELAP5-3D model was run, simulating the IFE at 15.81 kW while using a gap thickness of 0.1 mills and produced Figure A.25. Predicted steady state IFE temperature is larger than measured steady state IFE temperature by approximately 17°C or 34°C, depending on which IFE temperature is used from Table A.2. Use of a 0.1 mil gap is thus conservative, and therefore all other core calculations use a gap thickness of 0.1 mills.

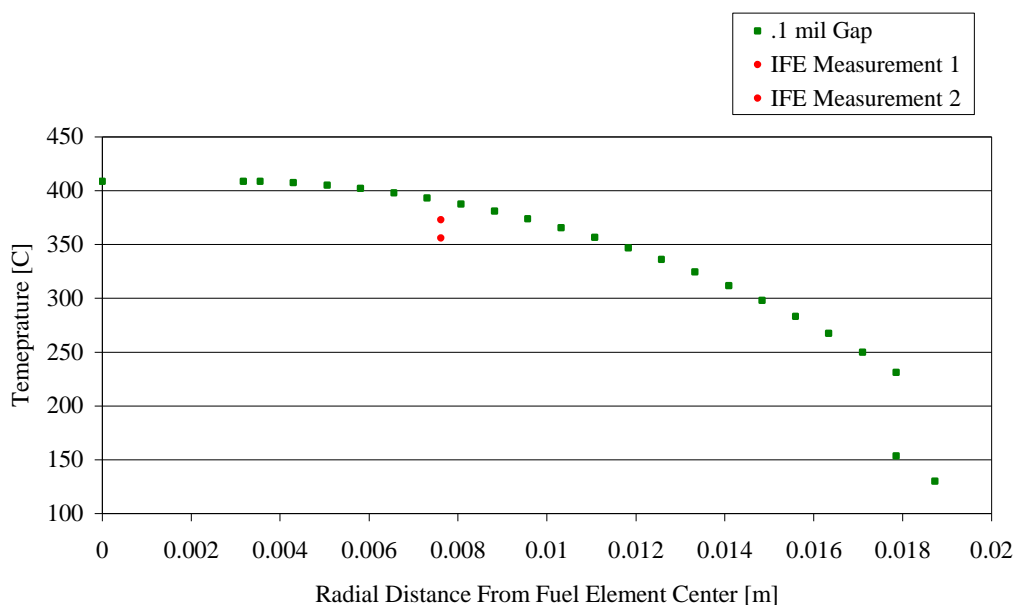


Figure A.25: IFE Radial Temp. Dist. at 15.81 kW (HEU Beginning of Life Normal Core).

The radial temperature distribution in the hot rod at the hottest axial elevation is shown in Figure A.26. Figure A.27 shows the radial temperature distribution in the hot rod with a core power of 1.1 MW_{th}. The different curves correspond to different values of the fuel to clad gap ranging from 1.27E-4 to 1.016E-3 m (0.05 to 0.4 mils). The hot rod in the BOL HEU core is located in position B3. The Instrumented Fuel Element (IFE) in the BOL HEU core is located in position B4. A summary of the

HEU Beginning of life core temperature results is shown in Table A.2. These results are based on a 0.1 mil fuel to clad gap.

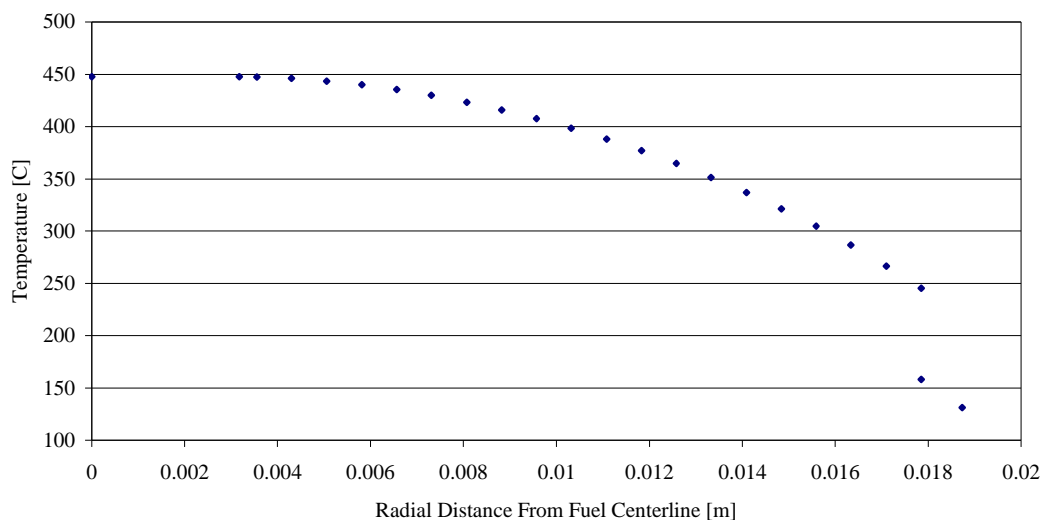


Figure A.26: Radial Fuel Temp. Dist. at 18.02 kW (HEU Beginning of Life Normal Core).

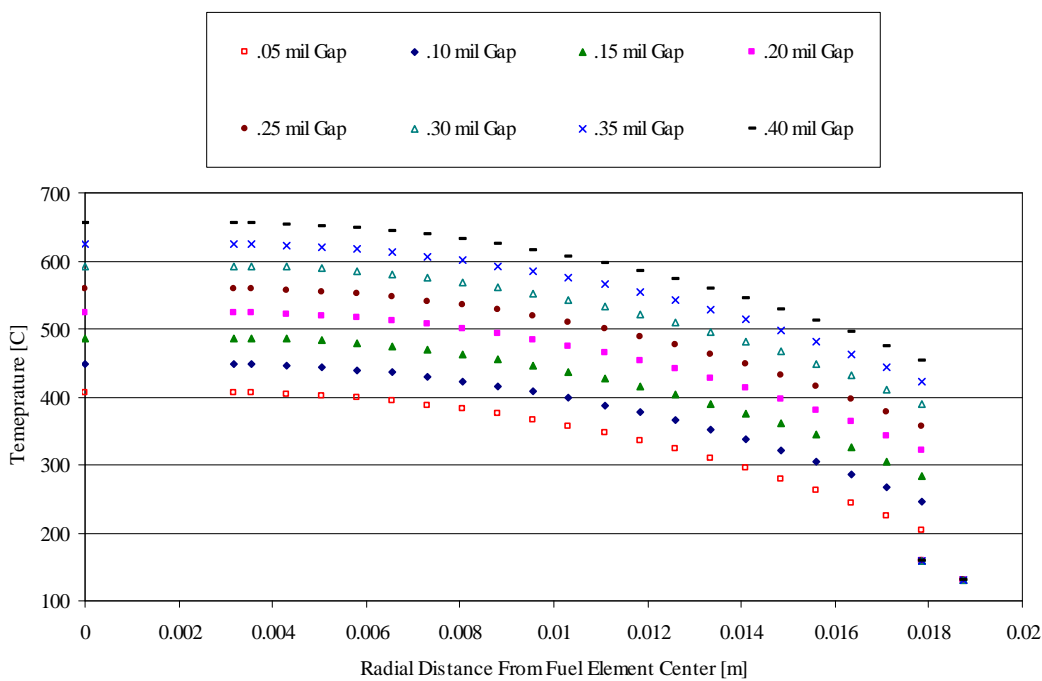


Figure A.27: Fuel Element Radial Temperature Distribution at 1.1 MW_{th}.

For pulse calculations a 0.1 mil gap is also justified. Pulse characteristics are typically adiabatic and thus insensitive to gap size. Furthermore, at the high fuel temperatures expected during the limiting pulse, differential radial expansion will significantly reduce gap size.

Table A.2: Calculated and Measured Fuel Temperatures, HEU Beginning of Life Core

$P_{\text{hot-channel}}$ (kW)	Measured [°C]	Calculated [°C]			
	T_{IFE}	T_{max}	$T_{0.3}$	T_{clad}	T_{coolant}
14.00	356, 373*	377	360	129	95
16.00		412	394	130	99
18.02		448	427	131	101
20.00		482	459	132	102
22.00		517	491	133	103

A.2.2 HEU Middle of Life Normal Core

Table A.3: Steady State Results of OSU HEU Middle of Life Normal Core

Parameter	Value
Flow rate for hottest rod [kg/s]	0.0845
Maximum flow velocity [m/s]	0.234
Maximum wall heat flux [kW/m ²]	495.08
Maximum fuel centerline temperature [°C]	475.63
Maximum clad temperature [°C]	131.27
Exit clad temperature [°C]	125.69
Exit bulk coolant temperature [°C]	100.97
MDNBR [Groeneveld 2006, Bernath]	4.934, 2.052

* Initial measured values, HEU Beginning of Life NORMAL Core at 1.0 MW_{th}.

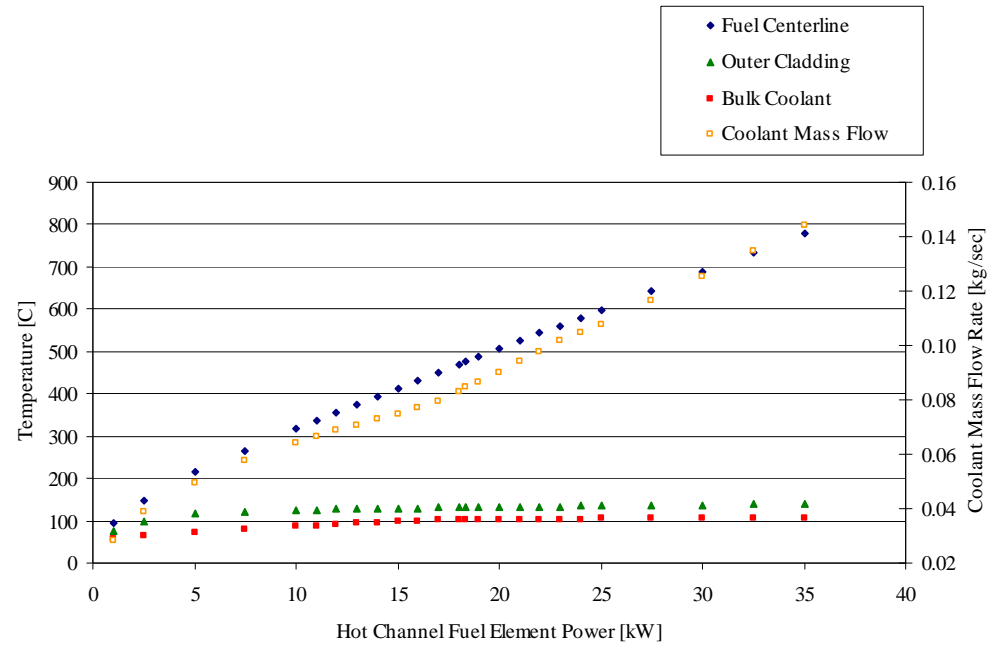


Figure A.28: Hot Channel Properties (HEU Middle of Life Normal Core)

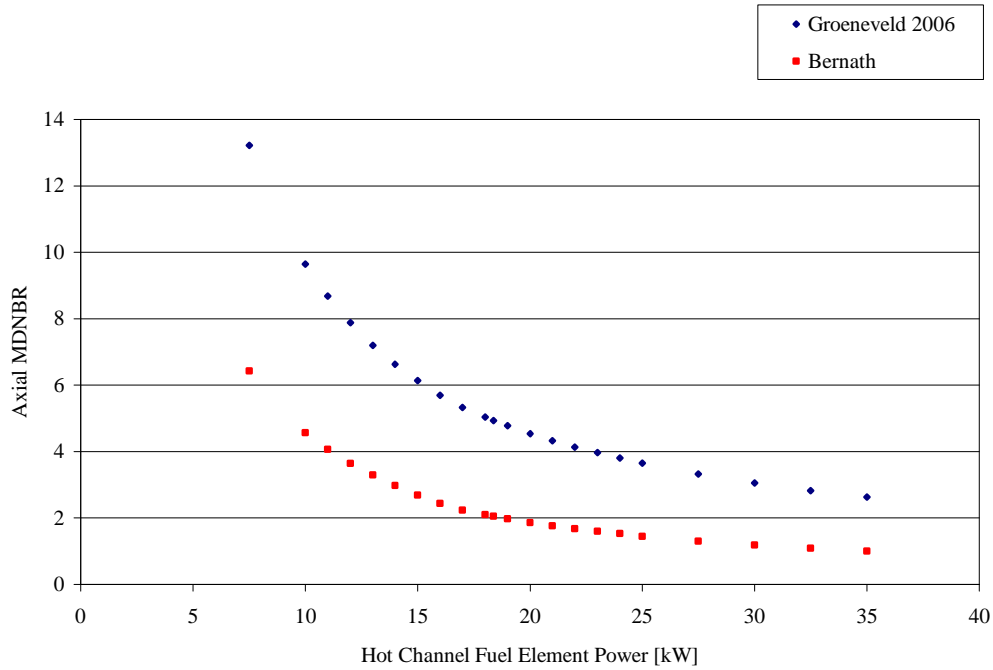


Figure A.29: Hot Channel MDNBR (HEU Middle of Life Normal Core)

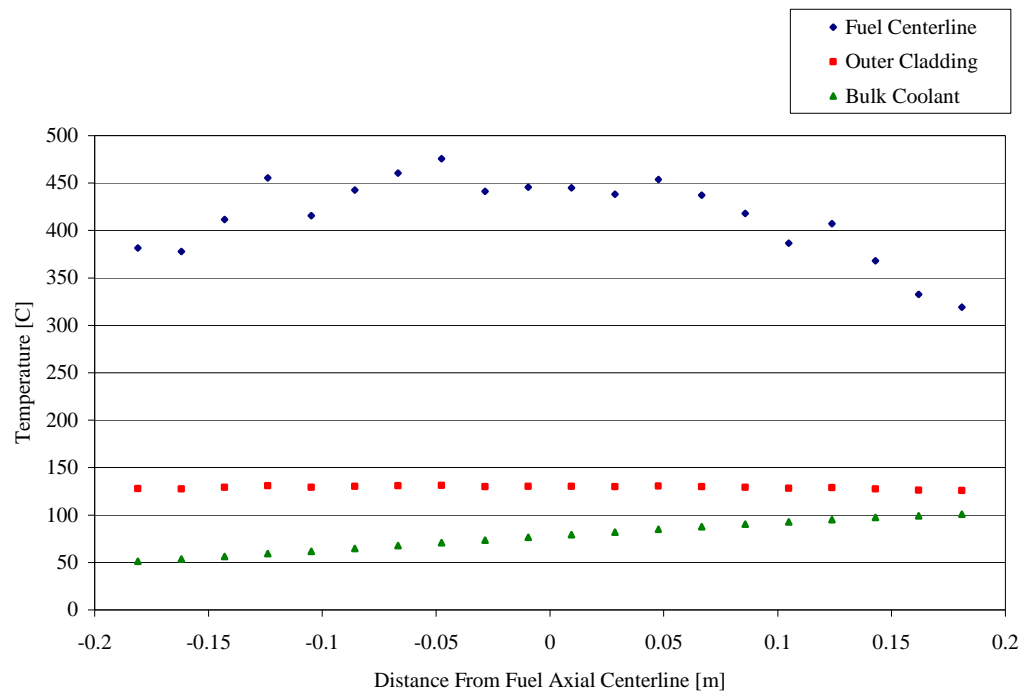


Figure A.30: Axial Temp. Distribution at 18.37 kW (HEU Middle of Life Normal Core)

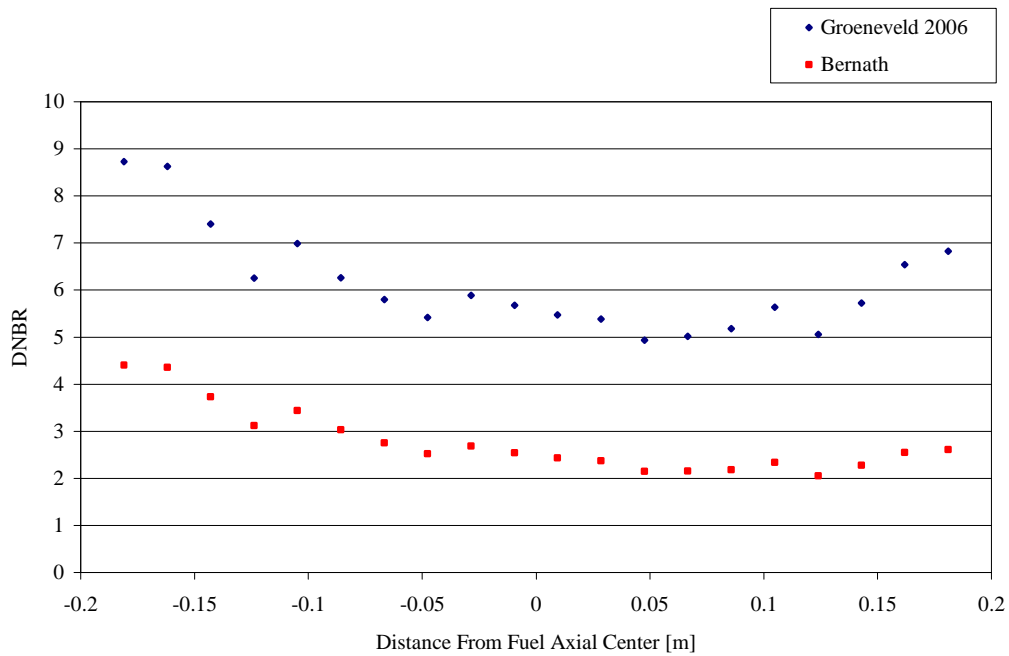


Figure A.31: Hot Channel Axial DNBR at 18.37 kW (HEU Middle of Life Normal Core)

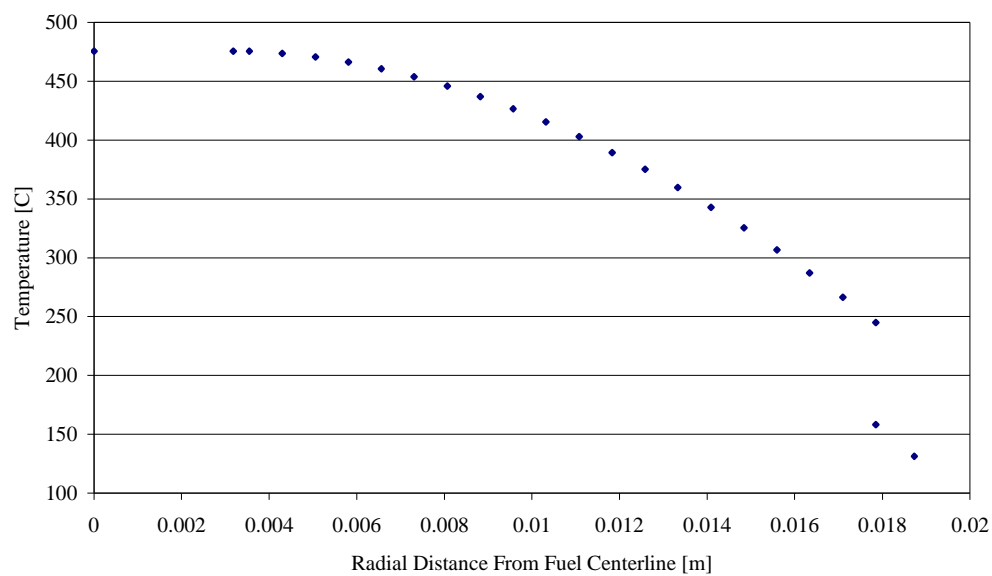


Figure A.32: Radial Temp. Distribution at 18.37 kW (HEU Middle of Life Normal Core)

Table A.4: Calculated Fuel Temp.'s at Powers in the HEU Middle of Life Normal Core

P _{hot-channel} (kW)	Calculated Temperature[°C]			
	T _{max}	T _{0.3}	T _{clad}	T _{coolant}
14.00	393	347	128	95
16.00	431	379	130	99
18.37	476	415	131	101
20.00	506	440	132	102
22.00	543	471	133	103

A.2.3 HEU End of Life Normal Core

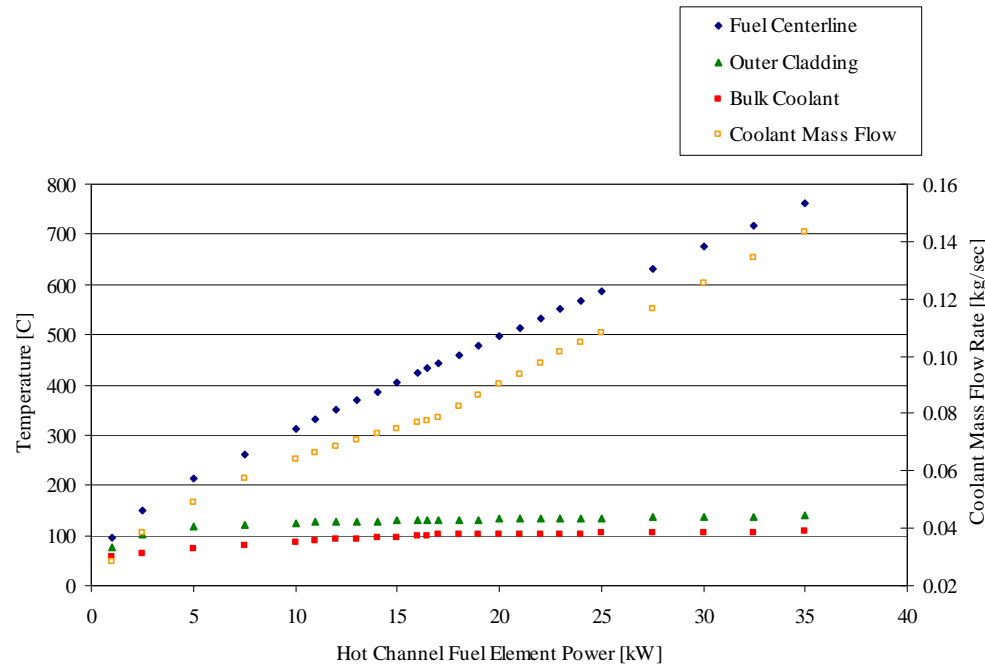


Figure A.33: Hot Channel Properties (HEU End of Life Normal Core)

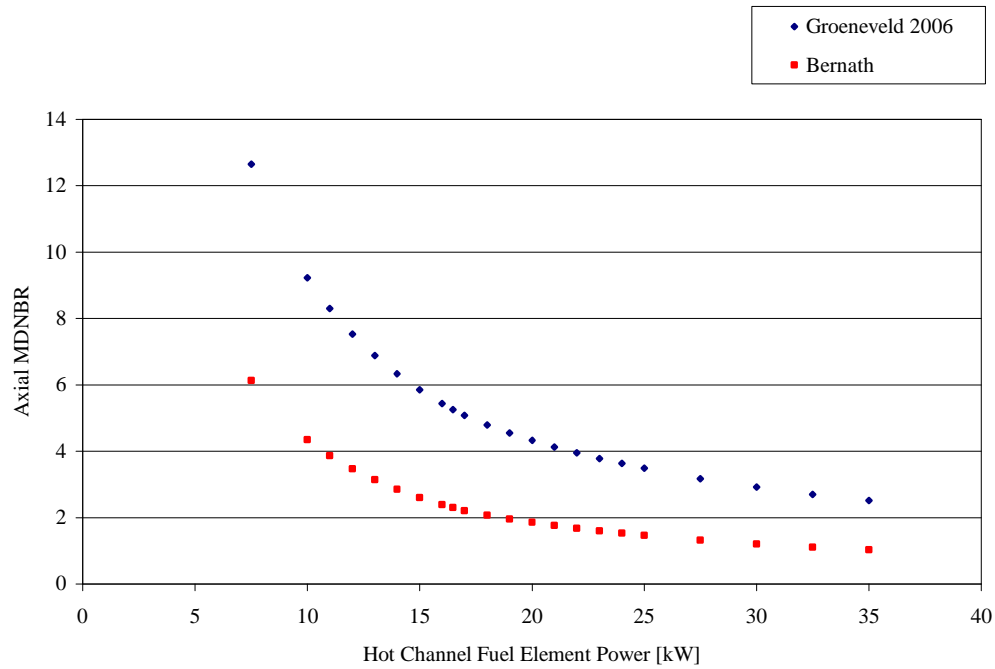


Figure A.34: Hot Channel MDNBR (HEU End of Life Normal Core)

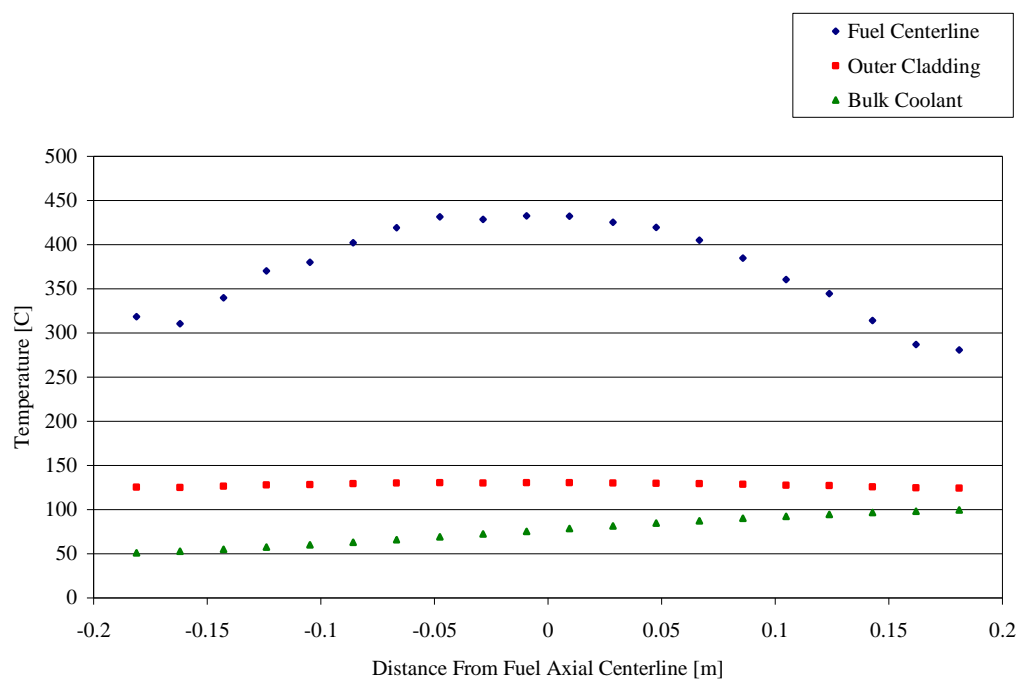


Figure A.35: Axial Temp. Distribution at 16.48 kW (HEU End of Life Normal Core)

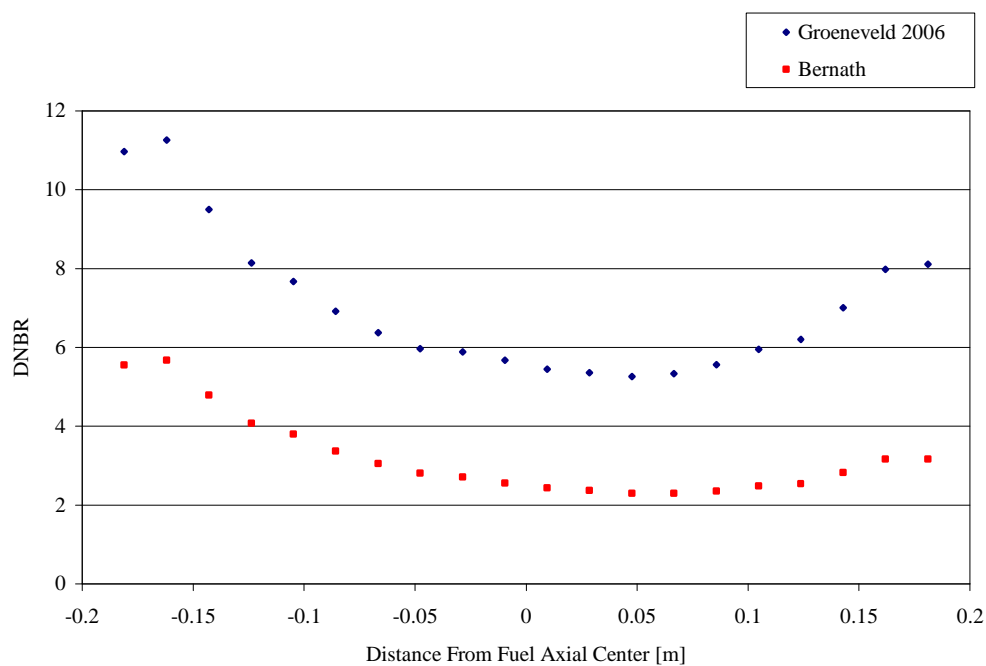


Figure A.36: Hot Channel Axial DNBR at 16.48 kW (HEU End of Life Normal Core)

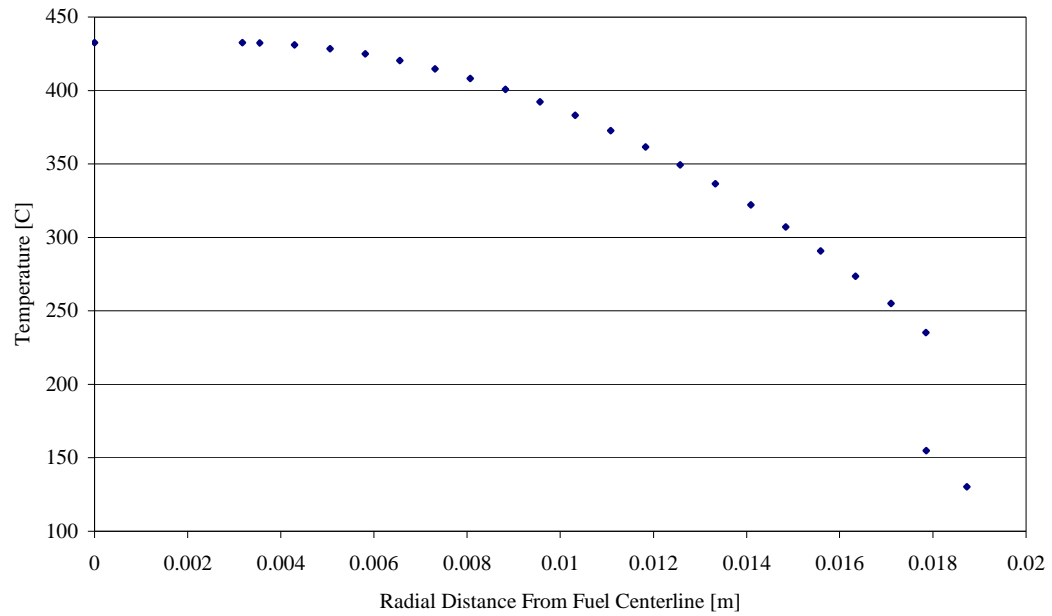


Figure A.37: Radial Temp. Distribution at 16.48 kW (HEU End of Life Normal Core)

Table A.5: Calculated Fuel Temp.'s for Powers in the HEU End of Life Normal Core

P _{hot-channel} (kW)	Calculated [°C]			
	T _{max}	T _{0.3}	T _{clad}	T _{coolant}
14.00	387	345	129	95
16.00	424	376	130	99
16.48	433	383	130	100
20.00	497	436	132	102
22.00	533	466	133	103

A.2.4 LEU Beginning of Life ICIT Core

Table A.6: Steady State Results for LEU Beginning of Life ICIT core at 1.1 MW_{th}

Parameter	Value
Flow rate for hottest rod [kg/s]	0.0843
Maximum flow velocity [m/s]	0.2339
Maximum wall heat flux [kW/m ²]	504.49
Maximum fuel centerline temperature [°C]	448.13
Maximum clad temperature [°C]	131.93
Exit clad temperature [°C]	126.36
Exit bulk coolant temperature [°C]	101.32
MDNBR [Groeneveld 2006, Bernath]	4.796, 2.083

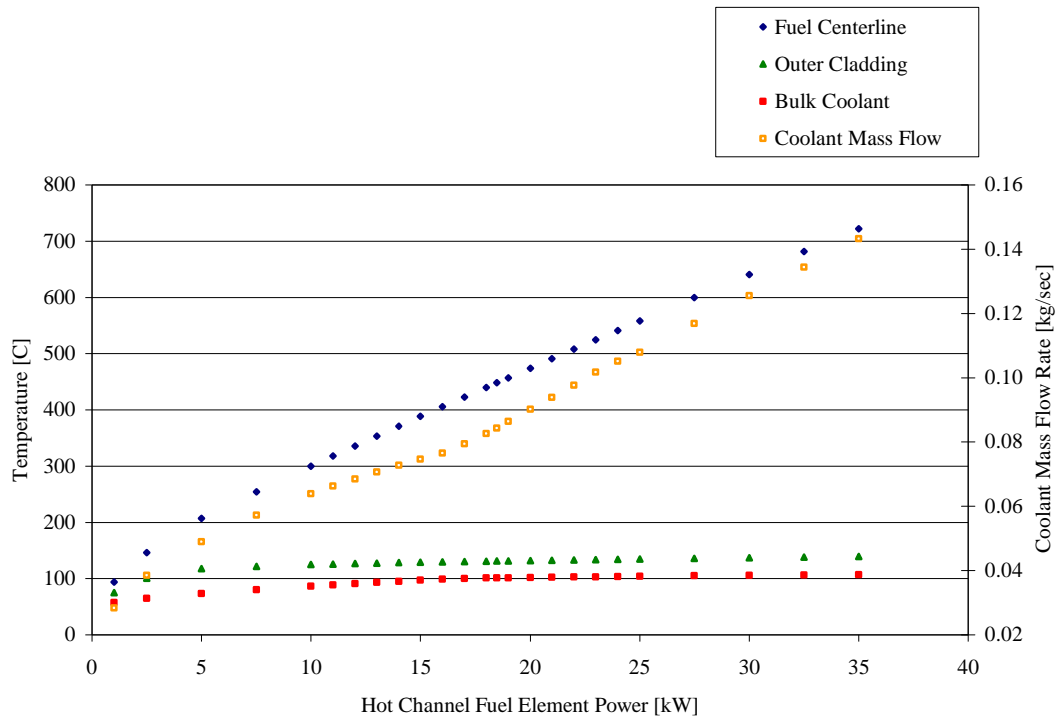


Figure A.38: Hot Channel Properties (LEU Beginning of Life ICIT Core)

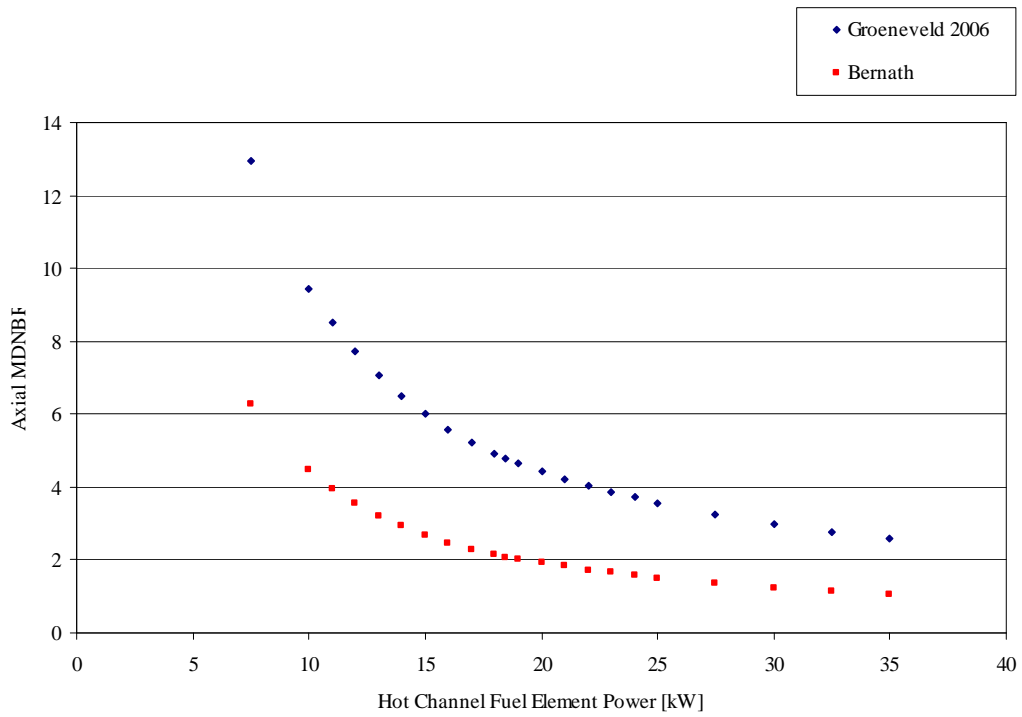


Figure A.39: Hot Channel MDNBR (LEU Beginning of Life ICIT Core)

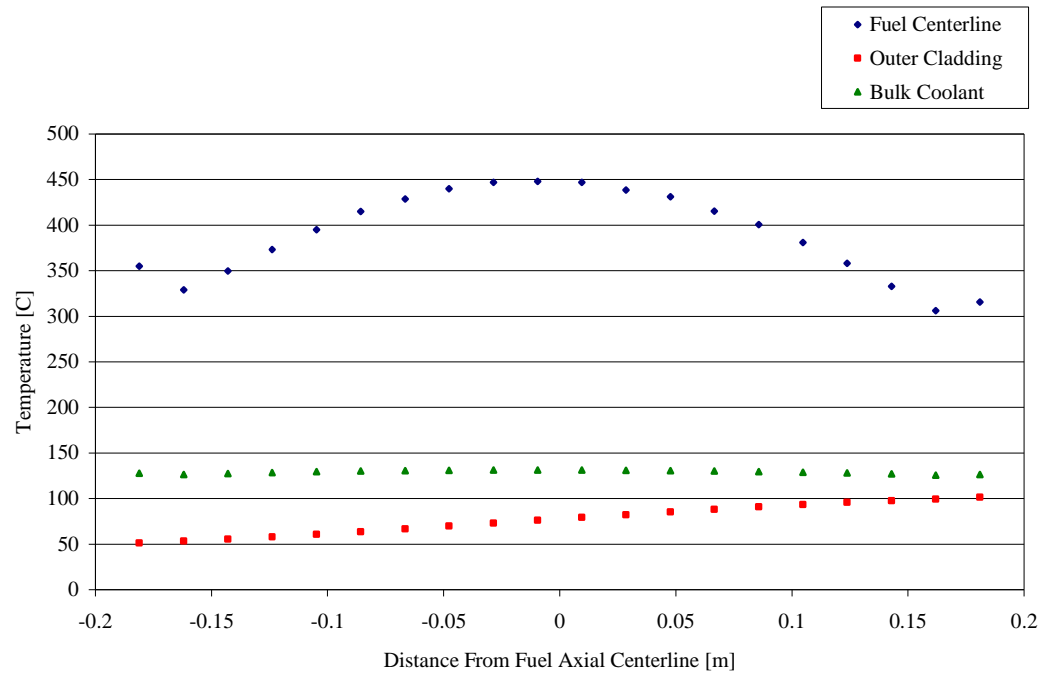


Figure A.40: Axial Temp. Distribution at 18.47 kW (LEU Beginning of Life ICIT Core)

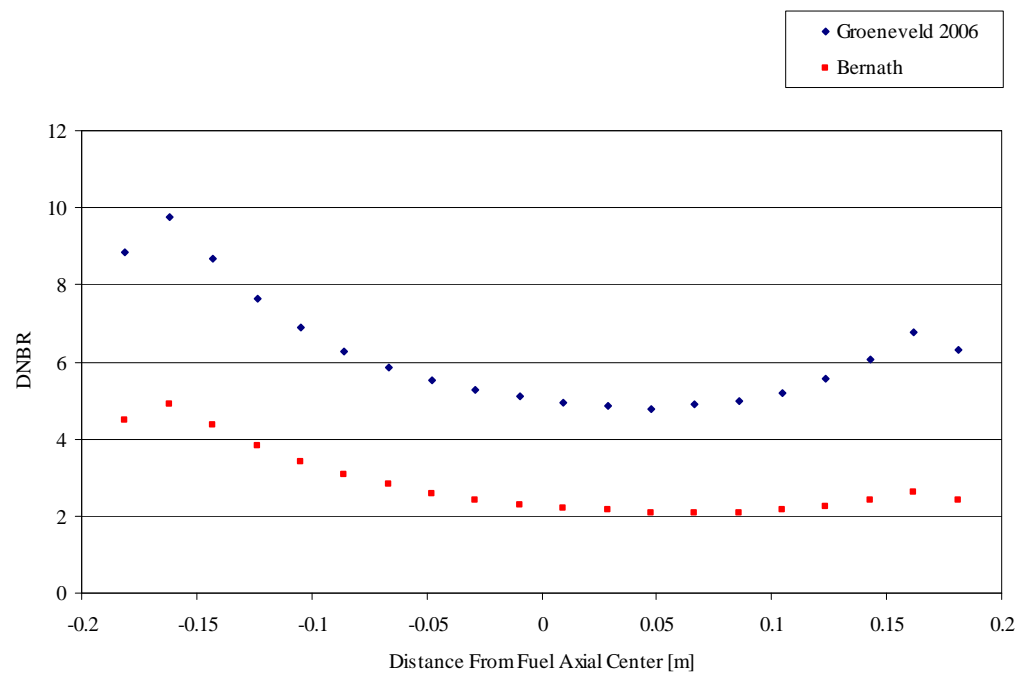


Figure A.41: Hot Channel Axial DNBR at 18.47 kW (LEU Beginning of Life ICIT Core)

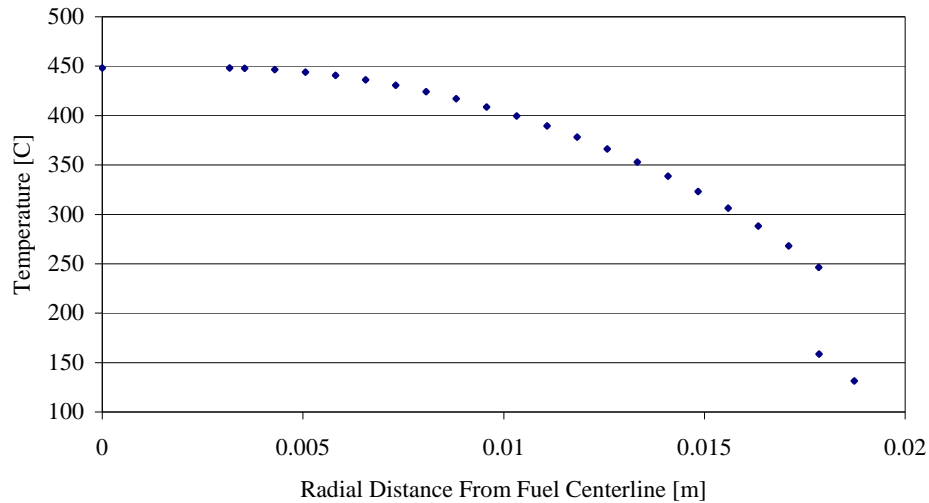


Figure A.42: Radial Temp. Distribution at 18.47 kW (LEU Beginning of Life ICIT Core)

Table A.7: Calculated Fuel Temp.'s for Powers in the LEU Beginning of Life ICIT Core

P _{hot-channel} (kW)	Calculated [°C]			
	T _{max}	T _{0.3}	T _{clad}	T _{coolant}
14.00	371	358	129	95
16.00	406	391	130	99
18.47	448	431	131	101
20.00	474	455	132	102
22.00	508	487	133	103

The LEU steady state results shown above are for the In Core Irradiation Tube (ICIT) core configuration. The LEU Beginning of Life ICIT core has a higher effective peaking factor than the LEU Beginning of Life Cadmium Lined In Core Irradiation Tube (CLICIT) core or the LEU Beginning of Life Normal core, and thus is the bounding core for steady state operation. The ICIT core configuration has a MDNBR of 2.083 at 1.1 MW_{th} steady state using the Bernath Correlation. Figure 4-51 shows that the MDNBR in the hot channel will reach a value of 2.00 at approximately 20.0 kW hot channel steady state power. This is 108.3% of the 18.47 kW produced in the hot channel of the LEU Beginning of Life ICIT core operating at 1.1 MW_{th}. Using either the Bernath or the Groeneveld 2006 correlations, the LEU Beginning of Life ICIT core is operating at power well below that required for departure from nucleate boiling.

A.2.5 LEU Middle of Life ICIT Core

Table A.8: Steady State Results for LEU Middle of Life ICIT core at 1.1 MW_{th}

Parameter	Value
Flow rate for hottest rod [kg/s]	0.0844
Maximum flow velocity [m/s]	0.2352
Maximum wall heat flux [kW/m ²]	507.74
Maximum fuel centerline temperature [°C]	457.66
Maximum clad temperature [°C]	131.46
Exit clad temperature [°C]	125.98
Exit bulk coolant temperature [°C]	101.40
MDNBR [Groeneveld 2006, Bernath]	4.754, 2.06

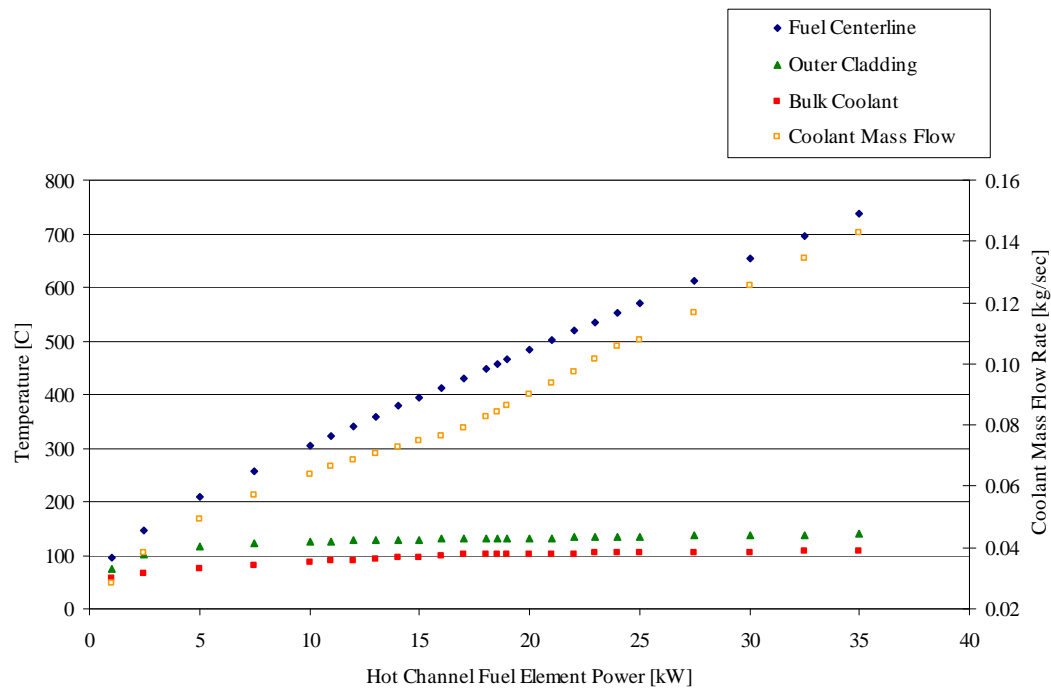


Figure A.43: Hot Channel Properties (LEU Middle of Life ICIT Core)

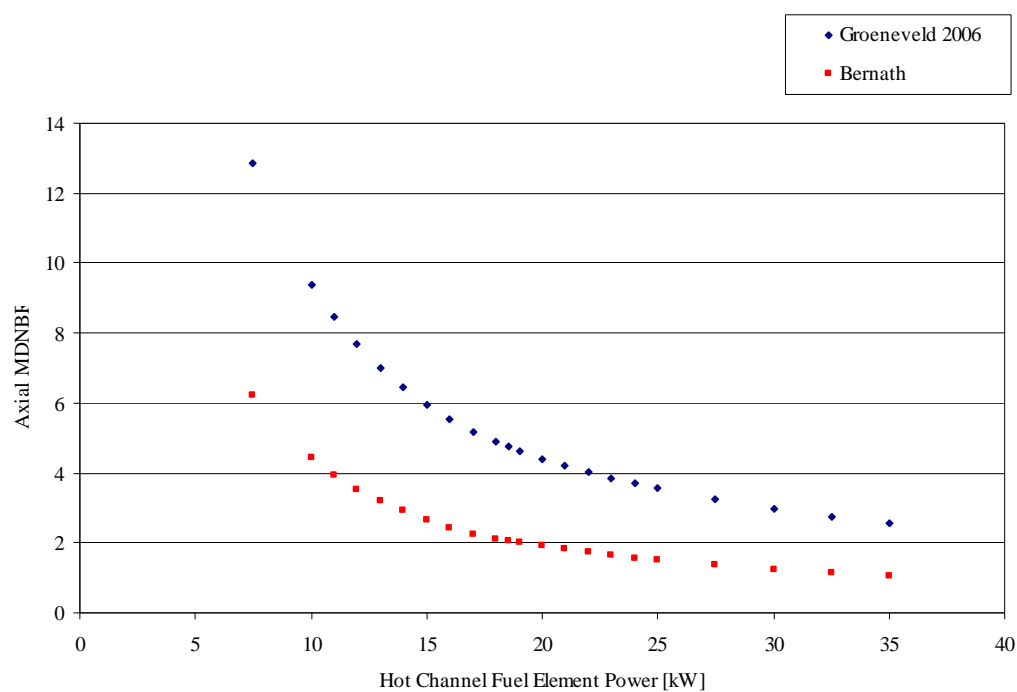


Figure A.44: Hot Channel MDNBR (LEU Middle of Life ICIT Core)

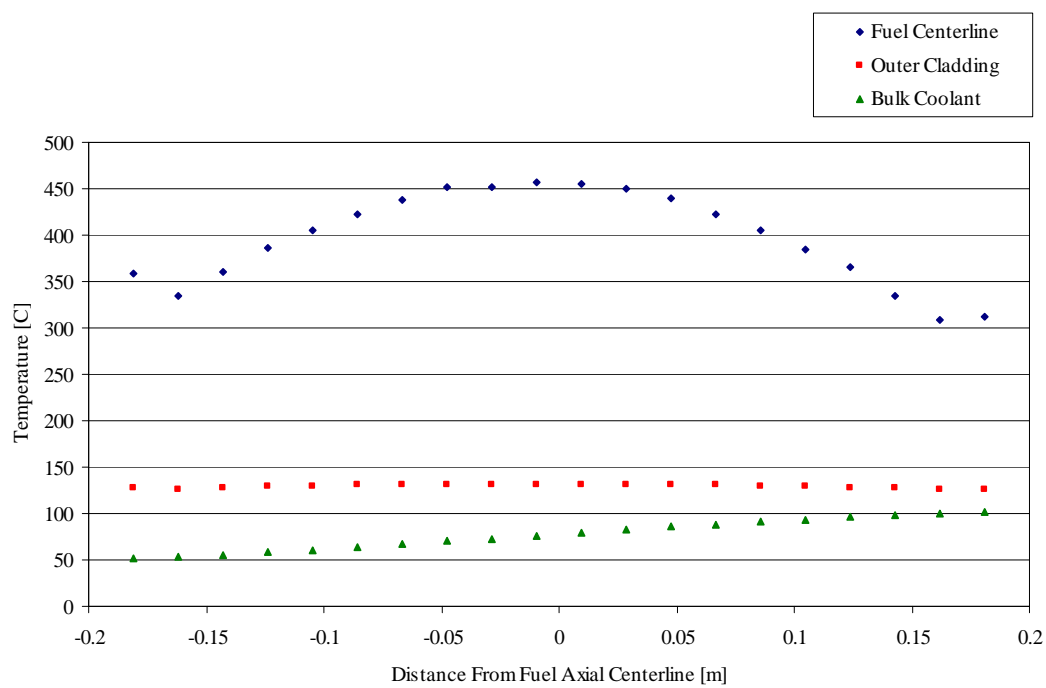


Figure A.45: Axial Temperature Distribution at 18.52 kW (LEU Middle of Life ICIT Core)

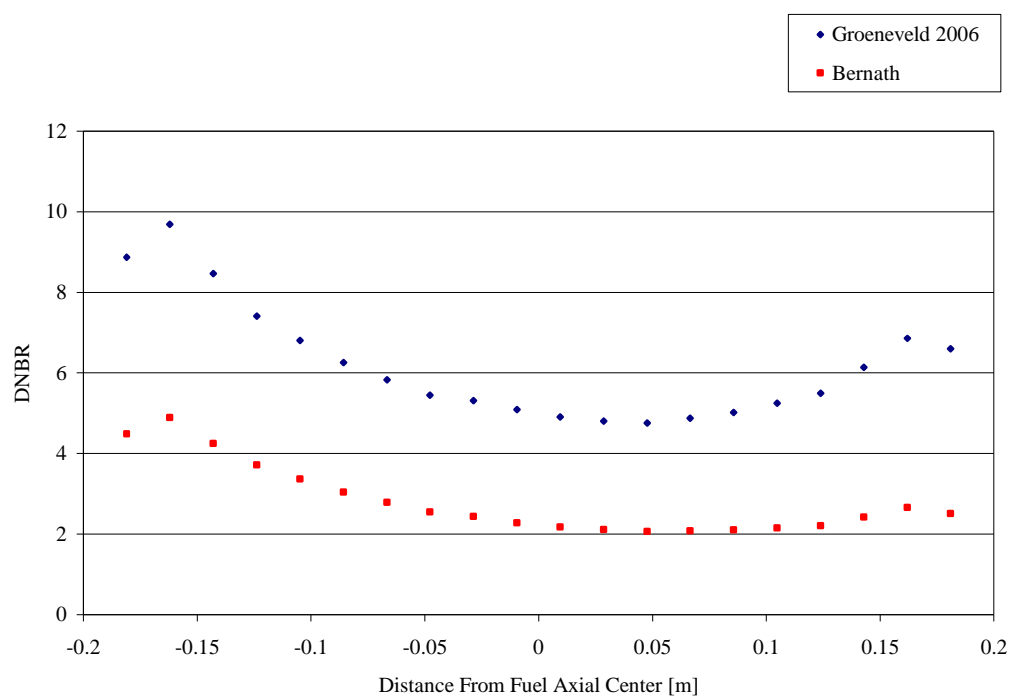


Figure A.46: Hot Channel Axial DNBR at 18.52 kW (LEU Middle of Life ICIT Core)

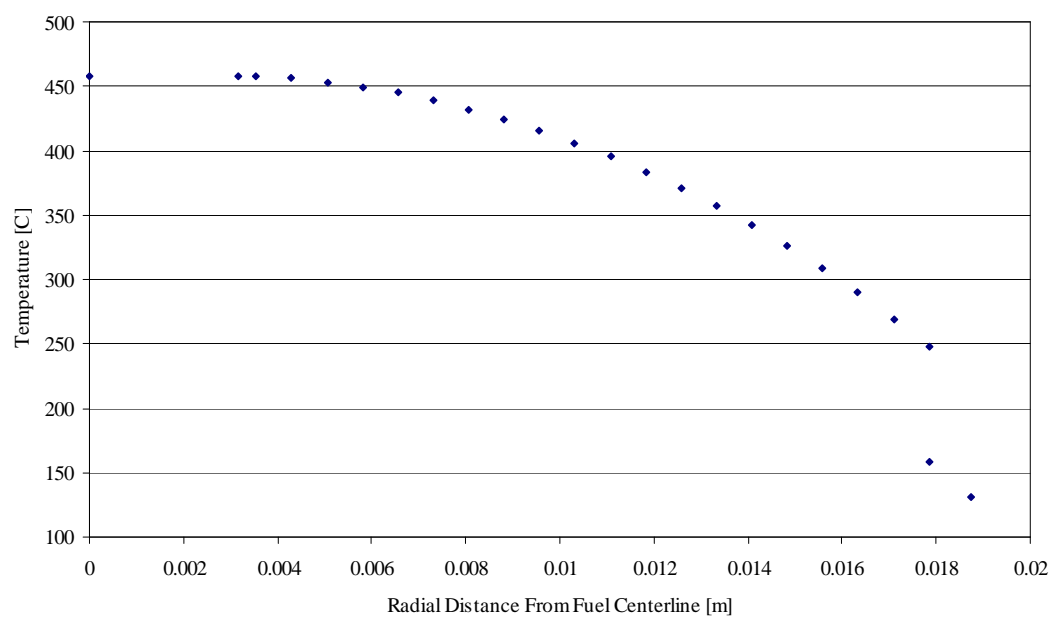


Figure A.47: Radial Fuel Temp. Distribution at 18.52 kW (LEU Middle of Life ICIT Core)

Table A.9: Calculated Fuel Temp.'s for Powers in the LEU Middle of Life ICIT Core

$P_{\text{hot-channel}}$ (kW)	Calculated Temperature[°C]			
	T_{max}	$T_{0.3}$	T_{clad}	T_{coolant}
14.00	378	361	129	95
16.00	413	394	130	99
18.52	458	436	131	101
20.00	483	460	132	102
22.00	518	492	133	103

The LEU steady state results shown above are for the ICIT core configuration. The LEU BOL ICIT core has a higher effective peaking factor than the LEU BOL CLICIT core or the LEU BOL Normal core, and thus is the bounding core for steady state operation. The ICIT core configuration has a MDNBR of 2.06 at 1.1 MW_{th} steady state using the Bernath Correlation. Figure A.44 shows that the MDNBR in the hot channel will reach a value of 2.00 at approximately 19.85 kW hot channel steady state power. This is 107.2% of the 18.52 kW produced in the hot channel of the LEU BOL ICIT core operating at 1.1 MW_{th}. Using either the Bernath or the Groeneveld 2006 correlations, the LEU BOL ICIT core is operating at power well below that required for departure from nucleate boiling.

A.2.6 LEU End of Life ICIT Core

Table A.10: LEU End of Life ICIT Core at 1.1 MW_{th}

Parameter	Value
Flow rate for hottest rod [kg/s]	0.0812
Maximum flow velocity [m/s]	0.2245
Maximum wall heat flux [kW/m ²]	465.55
Maximum fuel centerline temperature [°C]	438.39
Maximum clad temperature [°C]	130.57
Exit clad temperature [°C]	125.87
Exit bulk coolant temperature [°C]	100.78
MDNBR [Groeneveld 2006, Bernath]	5.048, 2.202

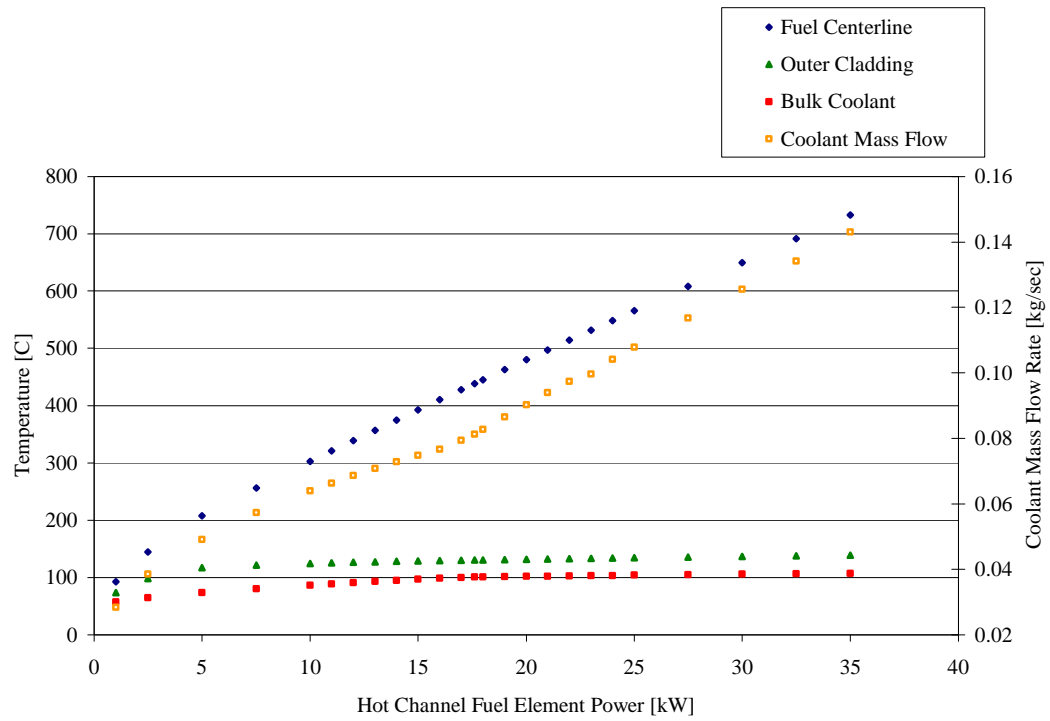


Figure A.48: Hot Channel Properties (LEU End of Life ICIT Core)

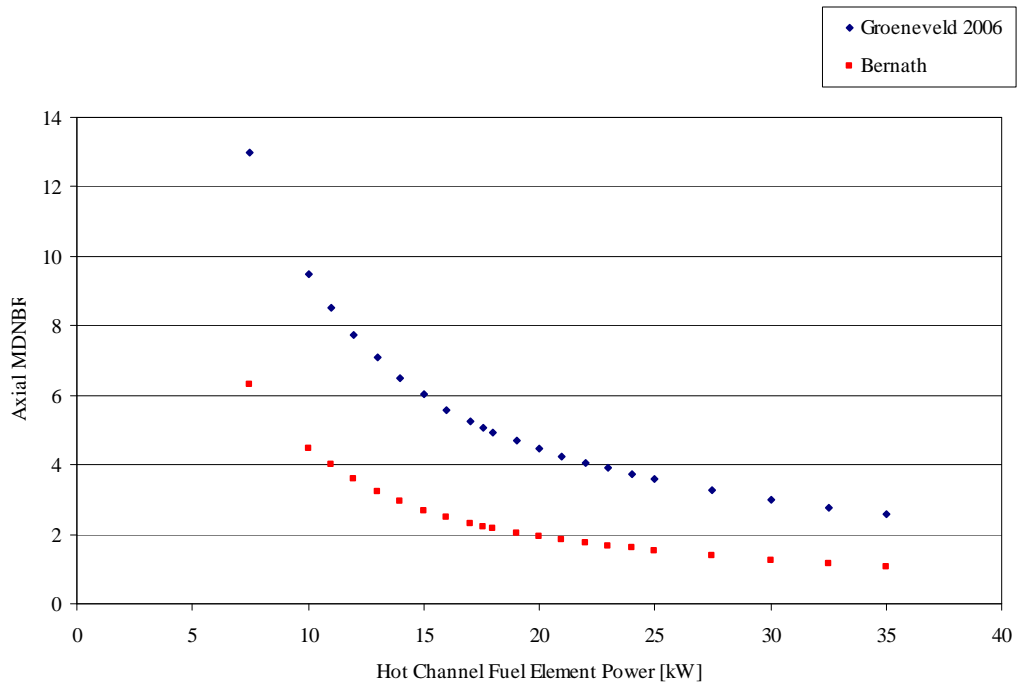


Figure A.49: Hot Channel MDNBR (LEU End of Life ICIT Core).

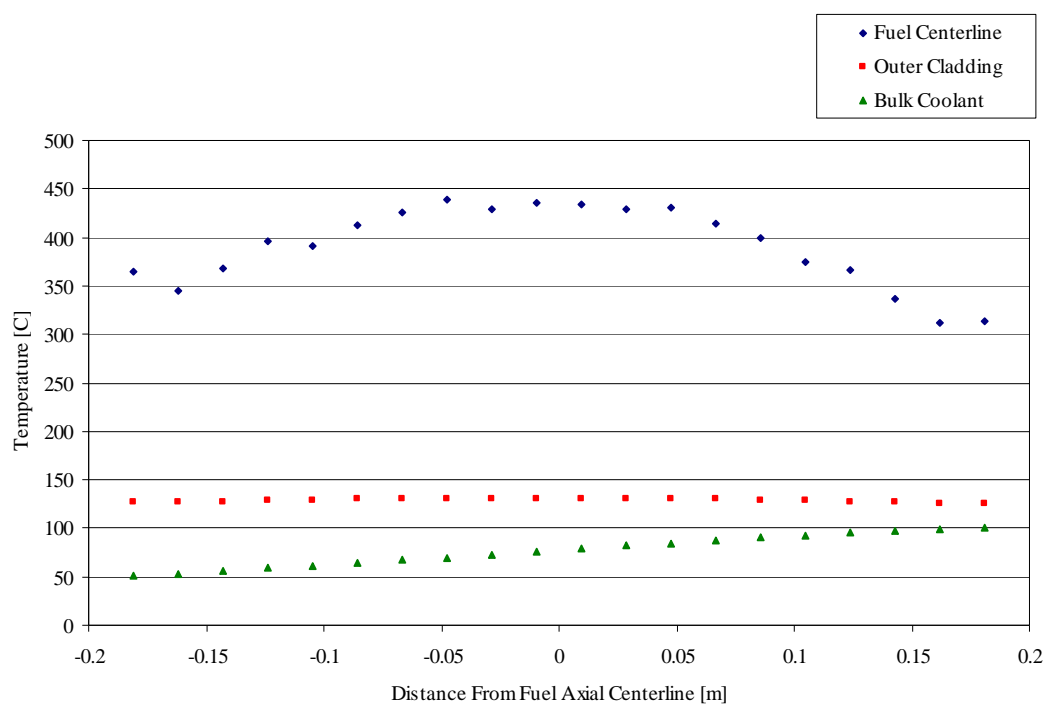


Figure A.50: Axial Temperature Distribution at 17.61 kW (LEU End of Life ICIT Core)

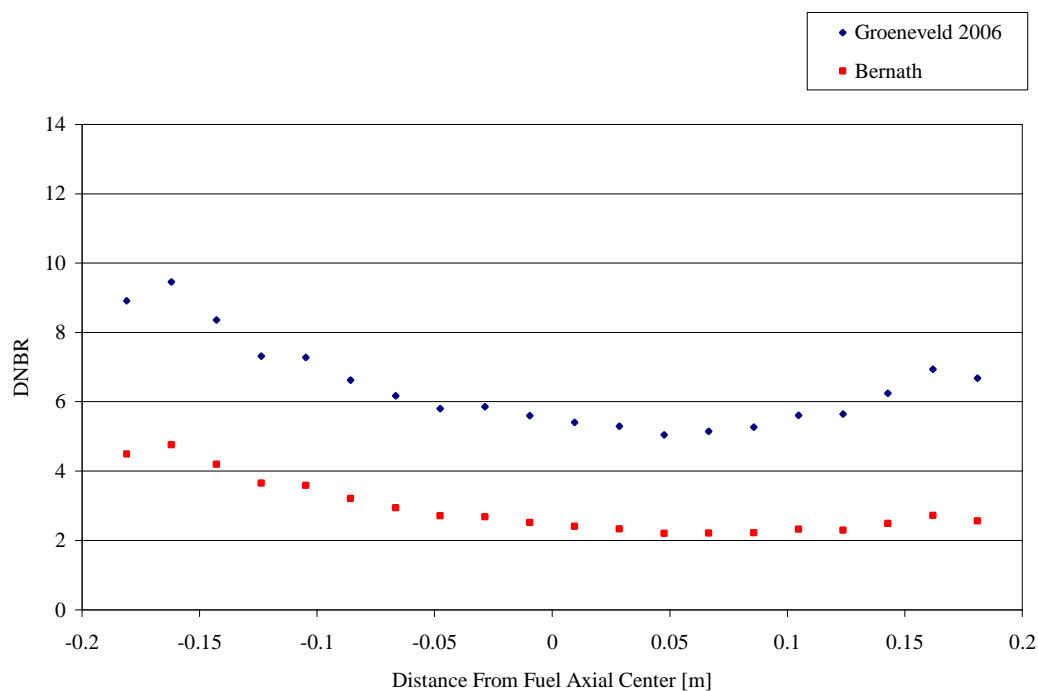


Figure A.51: Hot Channel Axial DNBR at 17.61 kW (LEU End of Life ICIT Core)

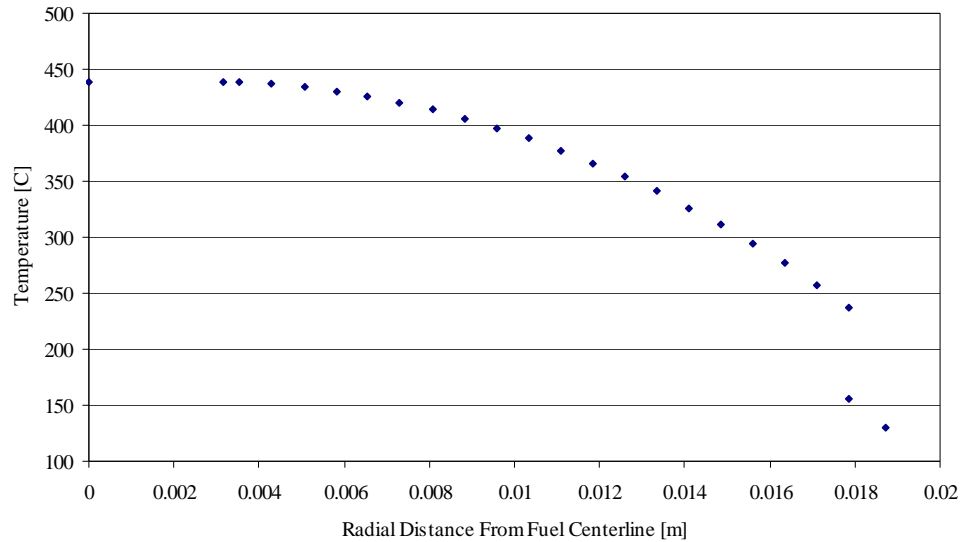


Figure A.52: Radial Fuel Temp. Distribution at 17.61 kW (LEU End of Life ICIT Core)

Table A.11: Calculated Fuel Temp.'s for Powers in the LEU End of Life ICIT Core

P _{hot-channel} (kW)	Calculated [°C]			
	T _{max}	T _{0.3}	T _{clad}	T _{coolant}
14.00	375	358	128	95
16.00	410	391	130	99
17.61	438	417	131	101
20.00	480	456	132	102
22.00	514	488	133	103

The LEU steady state results shown above are for the ICIT core configuration. The LEU BOL ICIT core has a higher effective peaking factor than the LEU BOL CLICIT core or the LEU BOL Normal core, and thus is the bounding core for steady state operation. The ICIT core configuration has a MDNBR of 2.20 at 1.1 MW_{th} steady state using the Bernath Correlation. Figure A.49 shows that the MDNBR in the hot channel will reach a value of 2.00 at approximately 20.0 kW hot channel steady state power. This is 113.6% of the 17.61 kW produced in the hot channel of the LEU BOL ICIT core operating at 1.1 MW_{th}. Using either the Bernath or the Groeneveld 2006 correlations, the LEU BOL ICIT core is operating at power well below that required for departure from nucleate boiling.

A.3 Pulse Results

A.3.1 HEU End of Life Normal Core

The pulse analysis was conducted by implementing the point reactor kinetics model in RELAP5-3D as previously discussed. An adjacent subchannel was modeled next to the hot channel simulating the remaining fuel elements in the HEU End of Life Normal Core. All Doppler feedback characteristics calculated by RELAP5-3D refer to the core average properties produced by the adjacent subchannel.

The technical specifications require that the SCRAM after a pulse occurs prior to 15.0 seconds, in reality a SCRAM occurs ~0.5 seconds after the transient rod is ejected. When conducting the pulse analysis it is assumed that the transient rod remains out of the core for 15.0 seconds and then is fully inserted back into the core, this scenario provides the most limiting conditions during a pulse. Figure A.53 presents the prompt total core power and energy trace produced in the RELAP5-3D model after inserting \$2.00 of reactivity. Figure A.54 provides power and energy trace information out to 100 seconds after the pulse. When referring to Figure A.54, a prompt core power drop occurs at 15.0 seconds, this is due to the insertion of the transient rod back into the core. A second peak fuel temperature or “delayed” peak fuel temperature is produced as a result holding the transient rod out of the core for 15.0 seconds. Although the reactor inherently shuts itself down as a result of the erbium in the fuel absorbing the neutron population within the core, such a large excess in reactivity is held out of the core that the absorption potential of the erbium is saturated and therefore the reactor does not return to a shut down power of ~15 Watts, but rather a much higher shutdown power of ~3.5 MW_{th} as seen in Figure A.54. Once the transient rod is inserted back into the core, a normal shutdown power of ~15 Watts is attained and the corresponding fuel temperature drops significantly to its nominal shut down temperature ~50 °C.

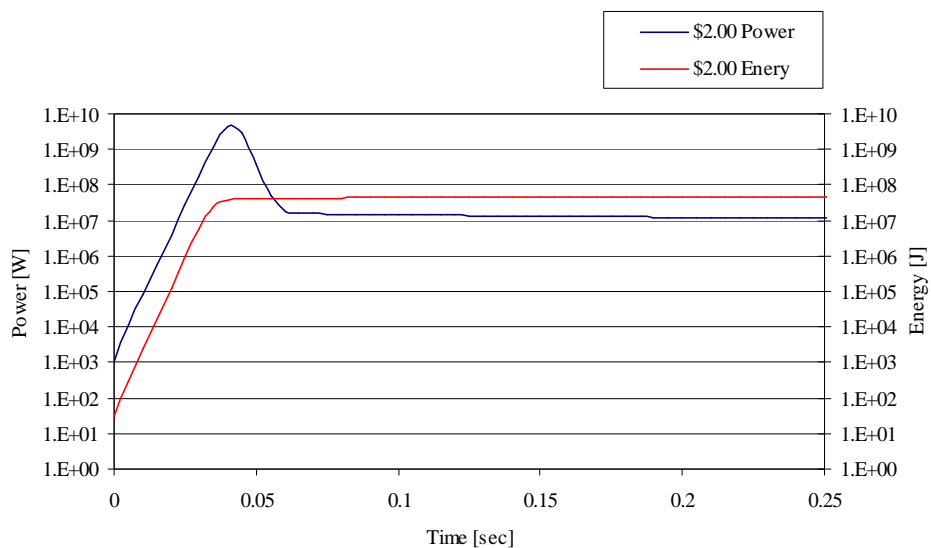


Figure A.53: HEU End of Life Normal Core \$2.00 Short Power/Energy Trace

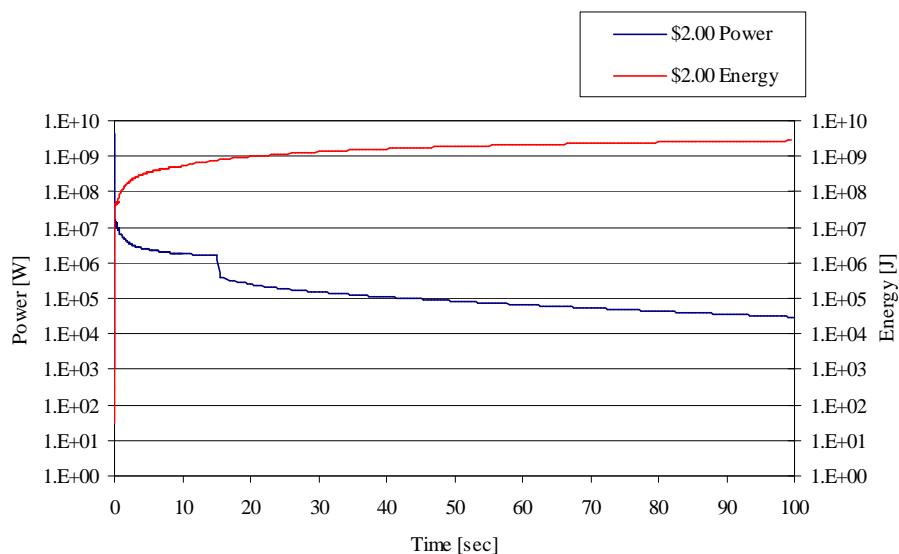


Figure A.54: HEU End of Life Normal Core \$2.00 Long Power/Energy Trace

The HEU EOL core is analyzed in order to allow comparison with data contained in the HEU SAR as seen in Figure A.55. The HEU core at EOL is considered to be the most limiting HEU core since it has the prompt temperature reactivity coefficient of the smallest magnitude, and thus a pulse due to a given amount of reactivity at EOL

will be larger than a pulse due to the same amount of reactivity at other times in core life.

The maximum adiabatic core temperature reached in a pulse is directly related to the energy released during the pulse, which is the integral of core power over the duration of the pulse. Changes in the maximum power reached in a pulse have little effect on this maximum temperature, as the reactor is only in the maximum power state for a small fraction of the total pulse duration, particularly for larger reactivity insertions.

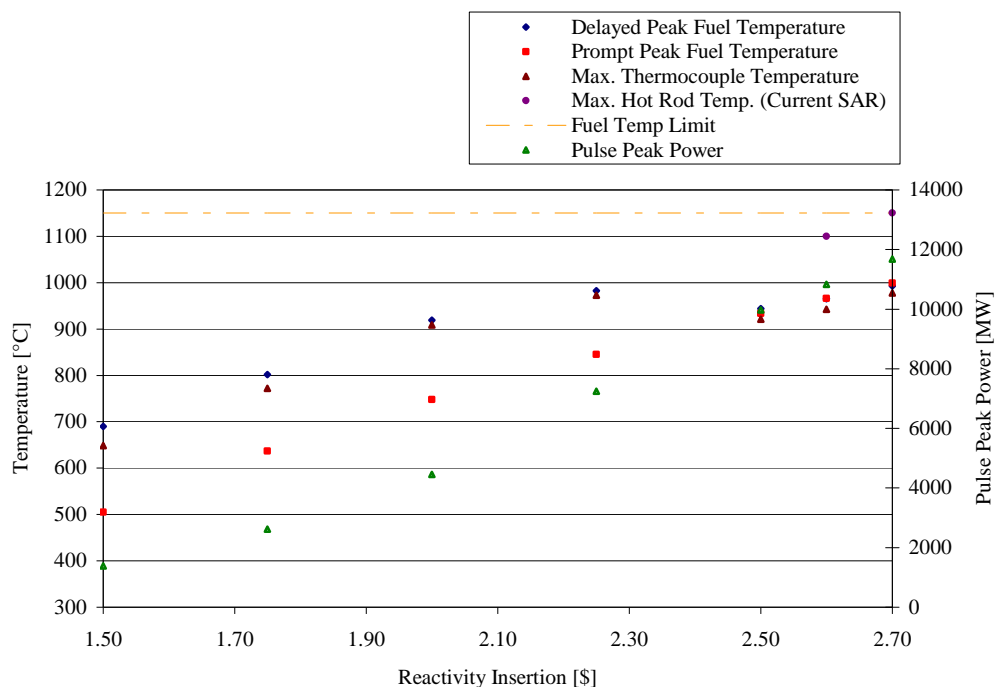


Figure A.55: Pulse Results Summary (HEU EOL Normal Core).

As mentioned, during the pulse analysis the transient rod is held withdrawn from the core for a total of 15.0 seconds due to the technical specifications. The initial prompt power transient during a pulse produces a peak fuel temperature within ~0.05 seconds after the initial rod motion; this can be seen for a \$2.00 pulse in Figure A.56. After the prompt power transient during the pulse a larger equilibrium power is then obtained in the core due to the excess reactivity of the withdrawn transient rod for

15.0 seconds. This brief increased equilibrium power produces a second or delayed peak in fuel temperature as observed in Figure A.57. The maximum resulting fuel temperature produced from due to this increased power is reported in Figure A.55 as the delayed peak fuel temperature while the maximum fuel temperature resulting from the prompt power transient is reported as the prompt maximum fuel temperature.

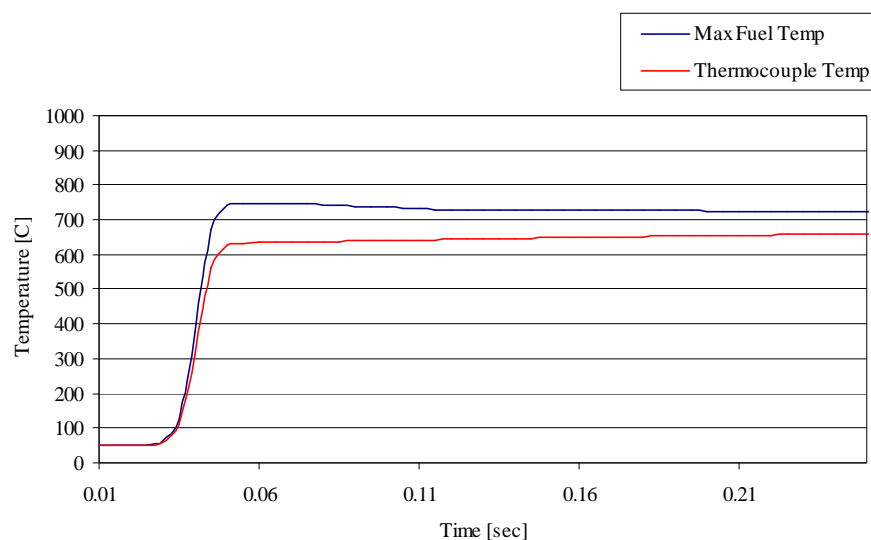


Figure A.56: HEU EOL, Short Hot Channel Pulse Fuel Temperatures (\$2.00 Insertion)

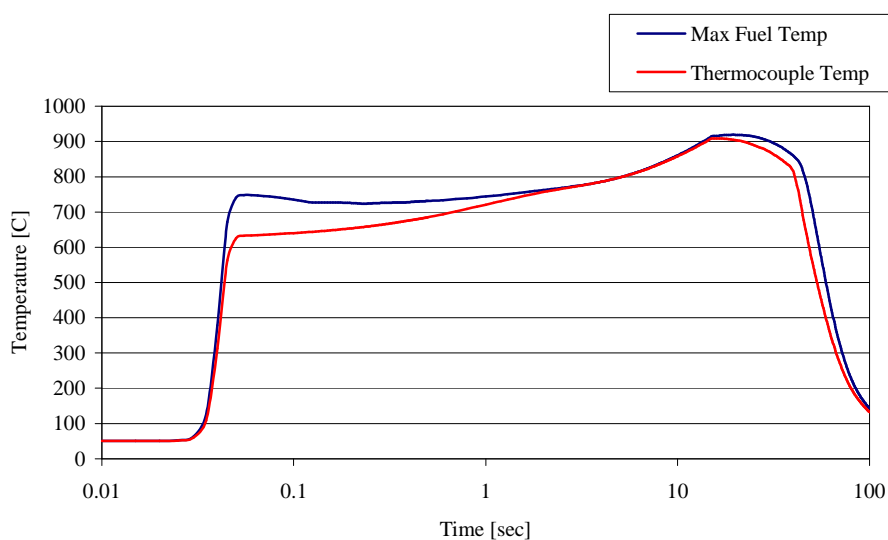


Figure A.57: HEU EOL, Long Hot Channel Pulse Fuel Temperatures (\$2.00 Insertion)

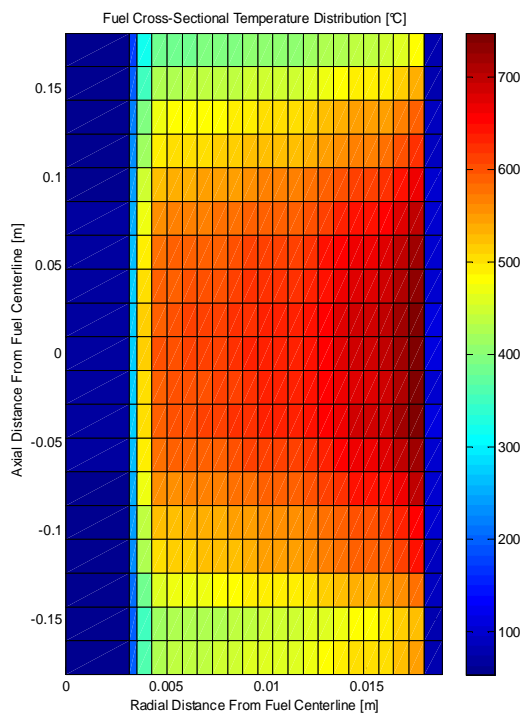


Figure A.58: Fuel Temperature Distribution at Time of Prompt Max Fuel Temperature

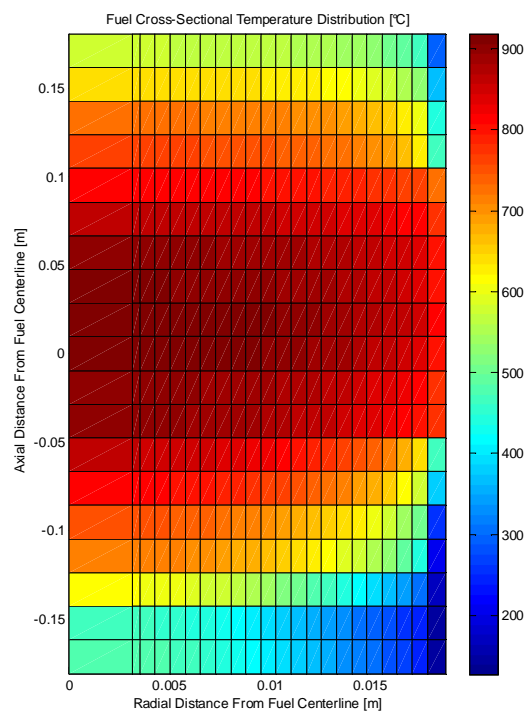


Figure A.59: Fuel Temperature Distribution at Time of Delayed Max Fuel Temperature

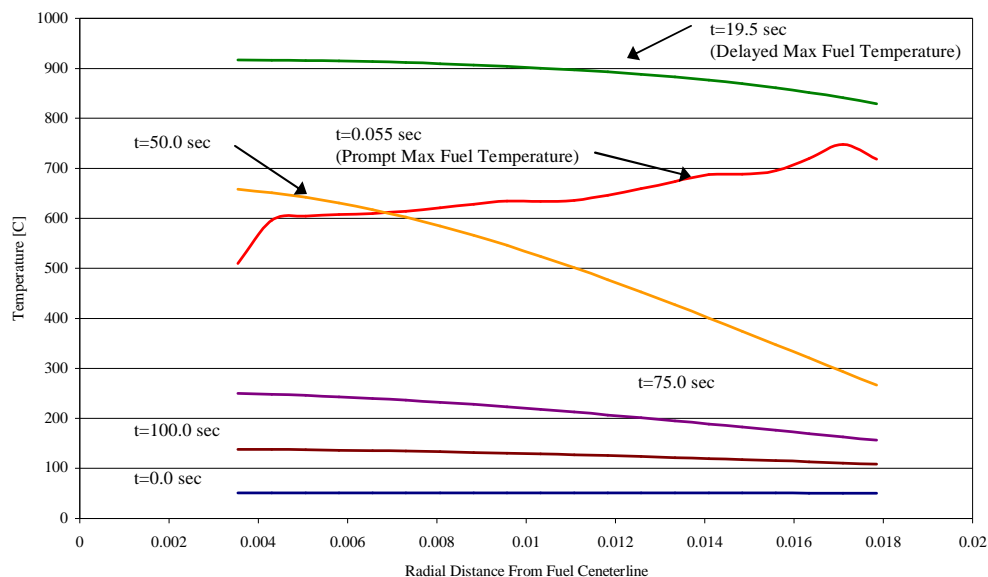


Figure A.60: HEU End of Life Normal, Radial Temp. Profile After Pulse (\$2.00 Insertion)

In the HEU SAR, the peak fuel temperature is identified as 1100°C for a reactivity insertion of \$2.59 and 1150°C for a reactivity insertion of \$2.70. Peak temperatures predicted by the methods used in this conversion SAR are 966.3°C for a \$2.59 pulse and 999.1°C for a \$2.70 pulse. The effective hot rod peak factor for the HEU SAR in the HEU EOL core is 3.41, while the effective hot rod peak factor used during this conversion analysis is 2.68 for the HEU EOL core. This difference in effective peak factor is partially responsible for the lower values of maximum fuel temperature produced during this conversion analysis study. Differences between the prompt reactivity coefficient used in the HEU SAR and the coefficient used in the conversion SAR also affect predicted peak temperatures.

A.3.2 LEU Beginning of Life ICIT Core

Five figures are given for each stage of core life. Values of important parameters are summarized in a table for each stage on core life.

The pulse summary figure graphically displays the following information for a series of pulses of different magnitudes:

1. the peak power of the core during the pulse
2. the prompt maximum value of the fuel in the hot channel
3. the delayed maximum value of the fuel in the hot channel
4. the maximum thermocouple temperature during the pulse, assuming that the IFE is located in the hot rod position

The hot channel temperature figure shows maximum fuel temperature in the core and maximum thermocouple temperature (assuming the IFE is the hot rod) as a function of time after a pulse. The hot channel fuel temperature distribution figures display fuel temperature in the hot rod at the time the prompt maximum fuel temperature and delayed maximum fuel temperature occurs. The hot channel fuel radial temperature

profile figure displays radial temperature distribution in the hot rod at various key times following a pulse.

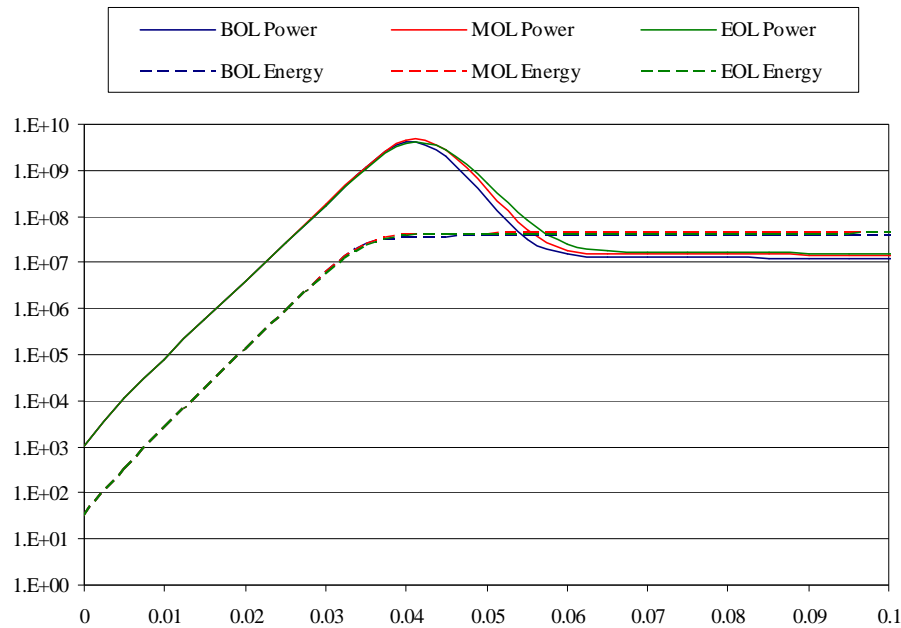


Figure A.61: Integral Core Pulse Power Trace (\$2.00 Pulse, LEU ICIT Core)

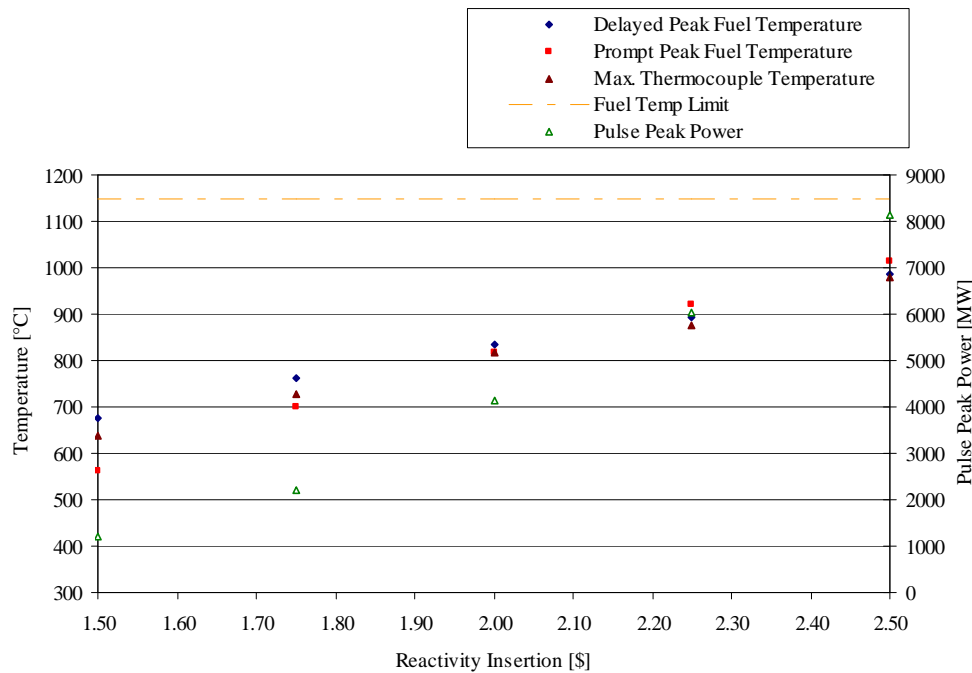


Figure A.62: Pulse Summary (LEU Beginning of Life ICIT Core).

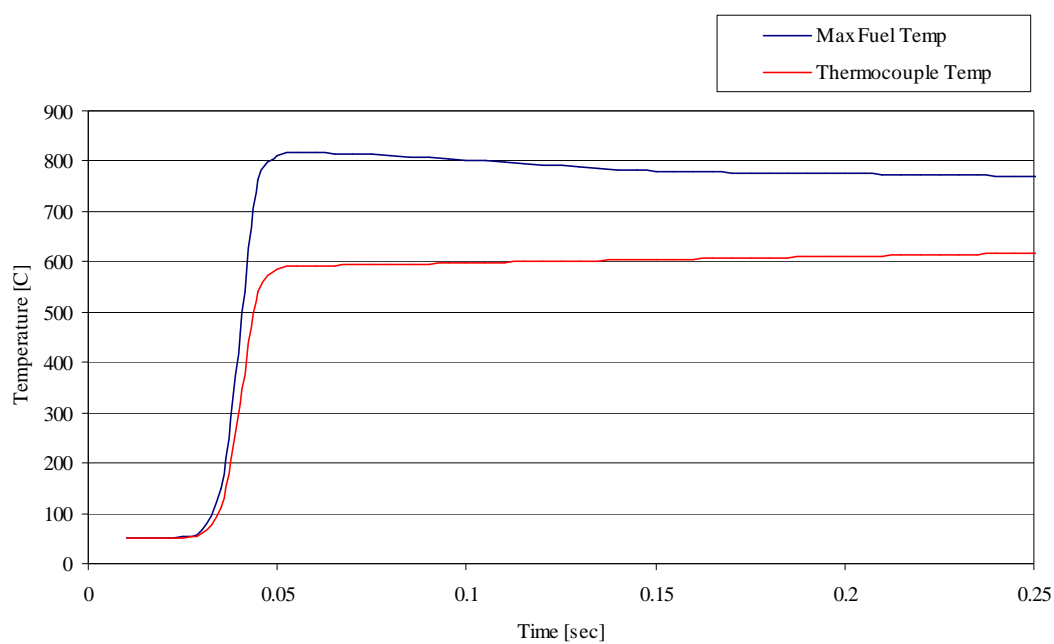


Figure A.63: LEU Beginning of Life ICIT, Short Hot Channel Fuel Temp. (\$2.00 Pulse)

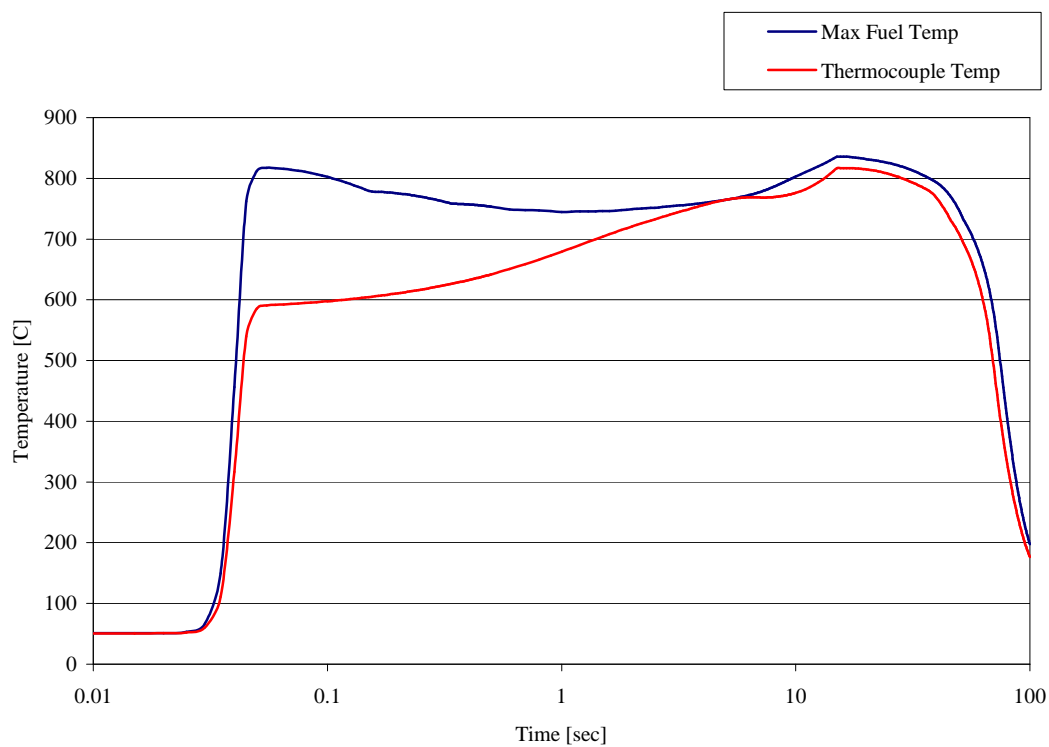


Figure A.64: LEU Beginning of Life ICIT, Long Hot Channel Fuel Temp. (\$2.00 Pulse)

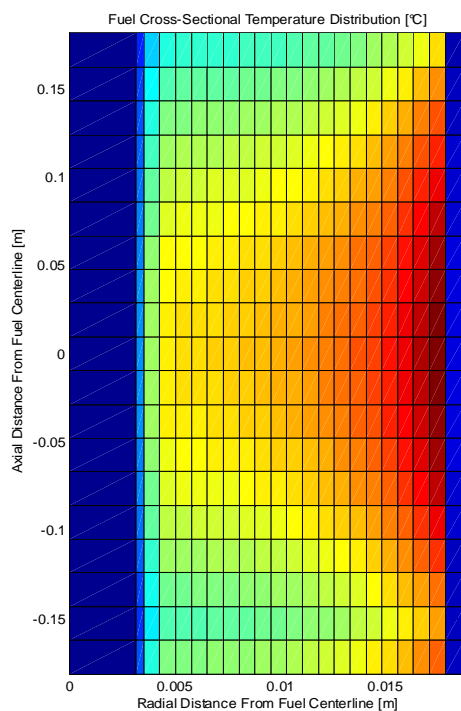


Figure A.65: Fuel Temperature Distribution at Time of Prompt Max Fuel Temperature

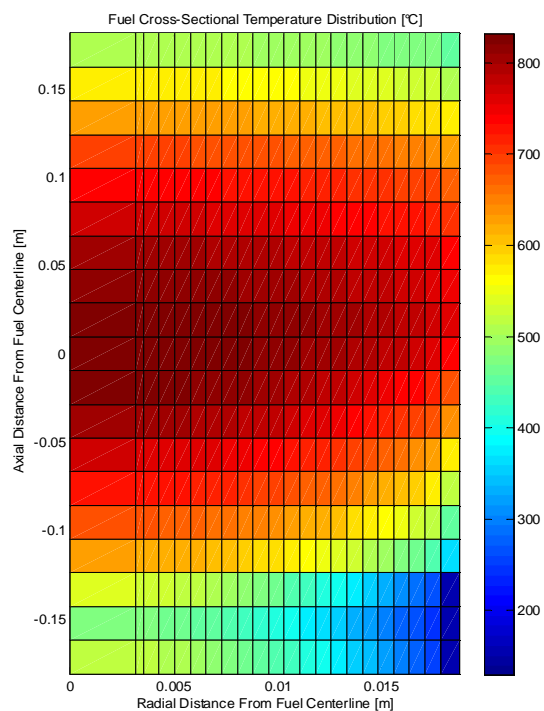


Figure A.66: Fuel Temperature Distribution at Time of Delayed Max Fuel Temperature

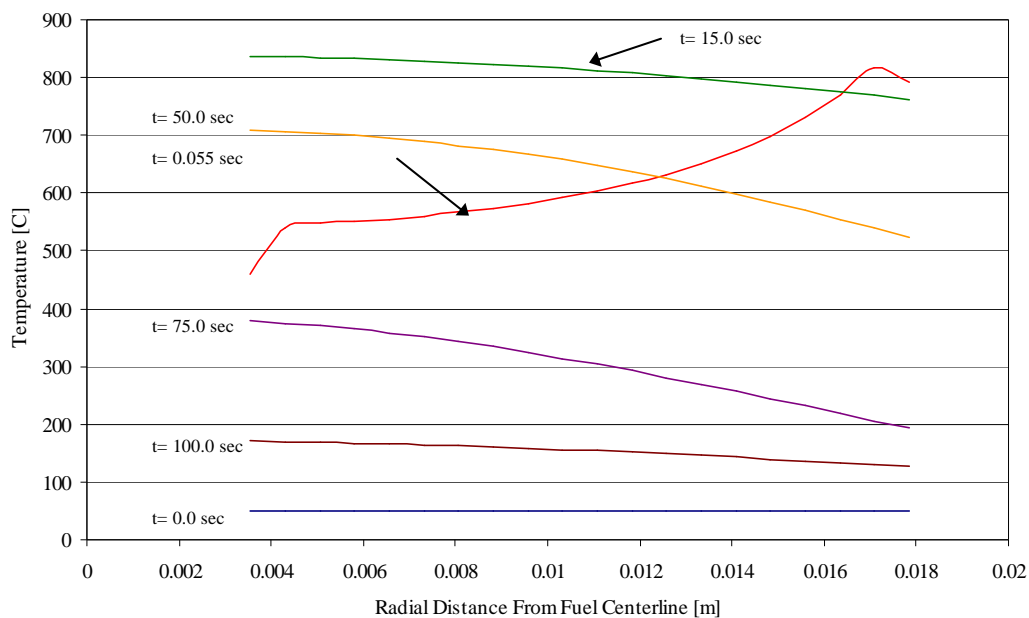


Figure A.67: HEU Beginning of Life ICIT Radial Temp. Profile after Pulse (\$2.00 Insertion)

Table A.12: Summary of LEU Beginning of Life ICIT Core Pulse Behavior

LEU-BOL ICIT Core Configuration Pulse Results Summary					
Reactivity Insertion [\$]	1.50	1.75	2.00	2.25	2.50
Peak Total Core Power [MW]	1216.40	2222.14	4138.70	6022.31	8138.44
Delayed Peak Fuel Temperature °C	674.30	762.70	835.90	892.90	984.50
Prompt Peak Fuel Temperature °C	560.90	701.18	817.40	919.50	1014.80
Max. Thermocouple Temperature °C	636.29	727.30	816.90	874.60	978

A.3.3 LEU Middle of Life ICIT Core

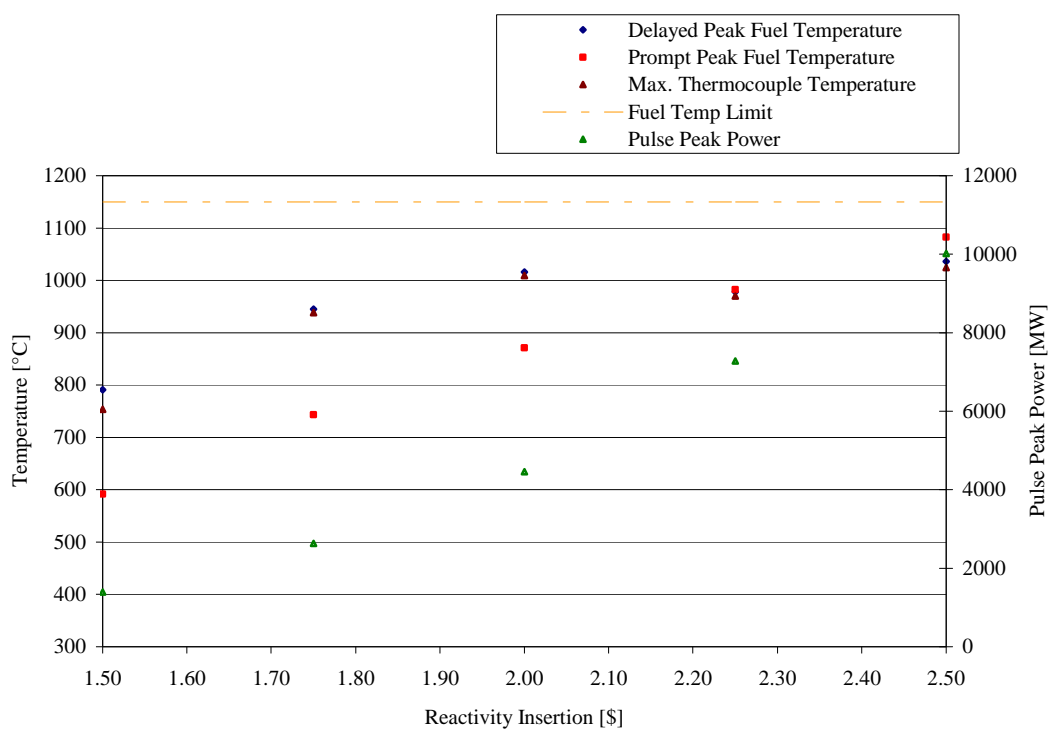


Figure A.68: Pulse Summary (LEU Middle of Life ICIT Core)

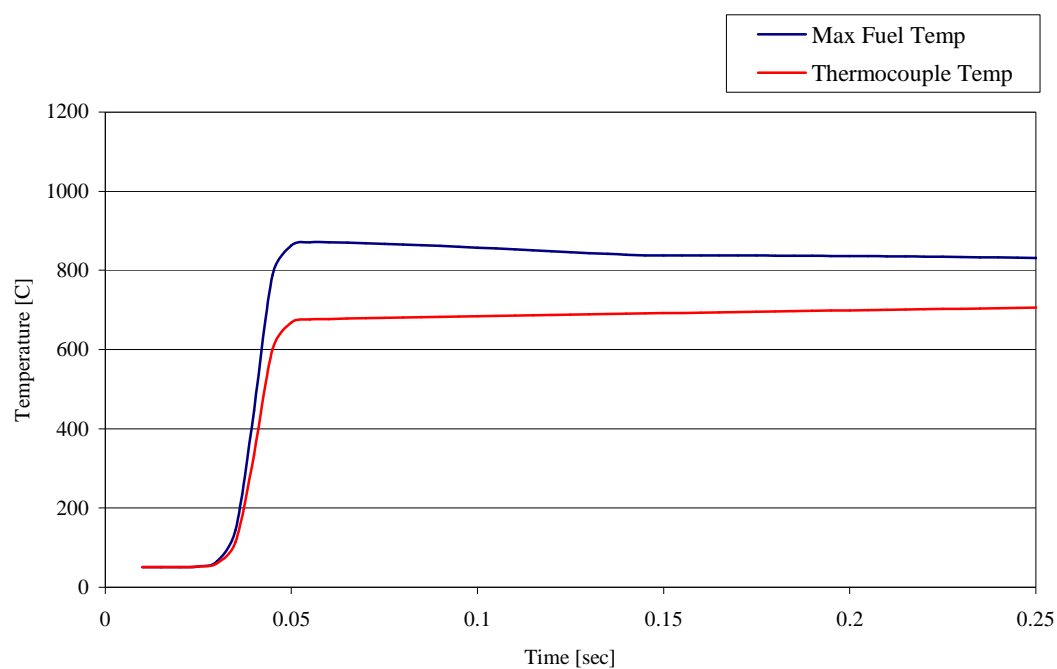


Figure A.69: LEU Middle of Life, Short Hot Channel Fuel Temperatures (\$2.00 Pulse)

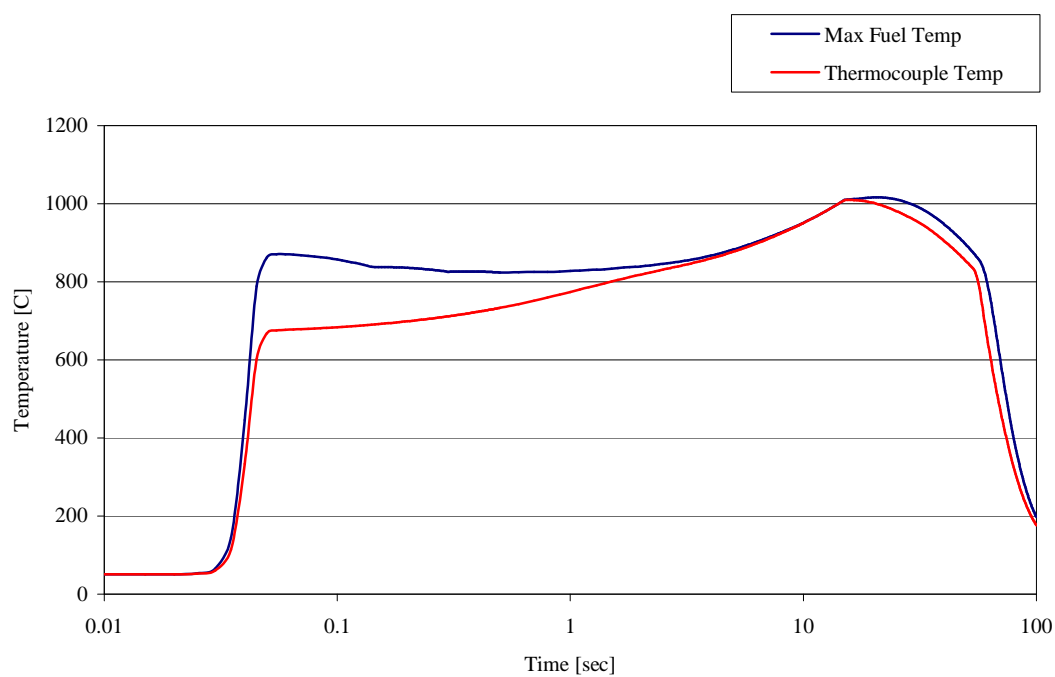


Figure A.70: LEU Middle of Life, Long Hot Channel Fuel Temperatures (\$2.00 Pulse)

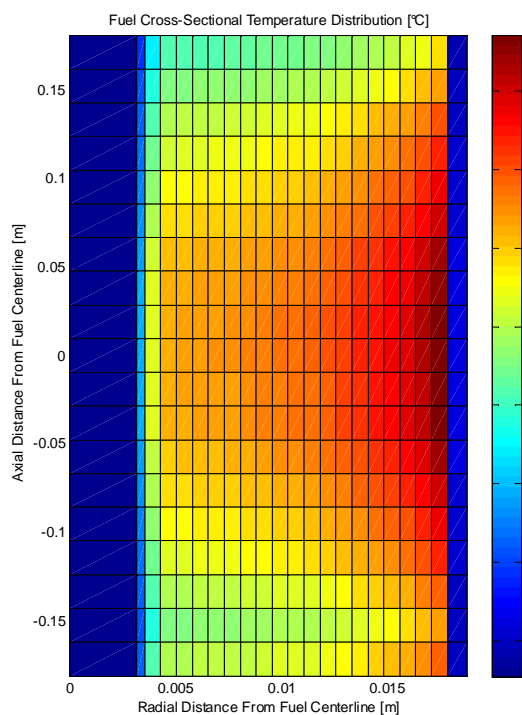


Figure A.71: Fuel Temperature Distribution at Time of Prompt Max Fuel Temperature

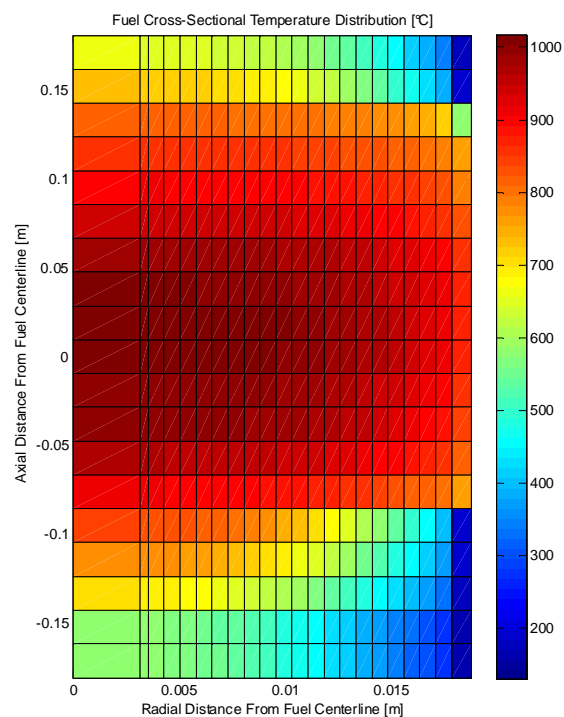


Figure A.72: Fuel Temperature Distribution at Time of Delayed Max Fuel Temperature)

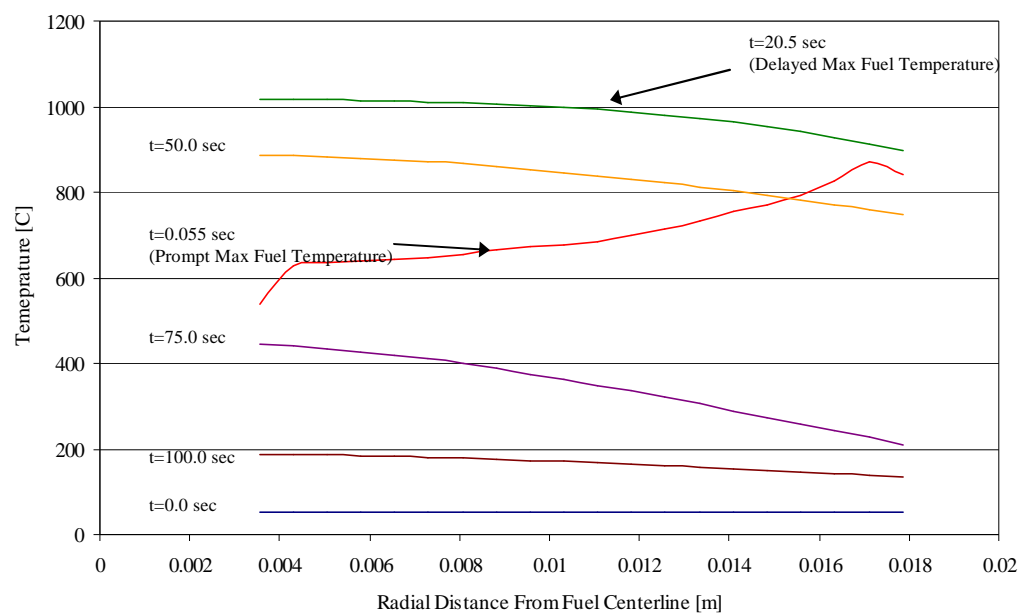


Figure A.73: LEU Middle of Life ICIT, Radial Temp. Profile after Pulse (\$2.00 Insertion)

Table A.13: Summary of LEU MOL ICIT Pulse Behavior

LEU-MOL ICIT Core Configuration Pulse Results Summary					
Reactivity Insertion [\$]	1.50	1.75	2.00	2.25	2.50
Peak Total Core Power [MW]	1393.62	2635.93	4459.49	7276.15	10017.10
Delayed Peak Fuel Temperature °C	790.80	945.30	1016.20	978.30	1036.40
Prompt Peak Fuel Temperature °C	591.56	743.10	870.80	982.10	1082.80
Max. Thermocouple Temperature °C	753.90	938.10	1009.50	969.90	1024.40

A.3.4 LEU End of Life ICIT Core

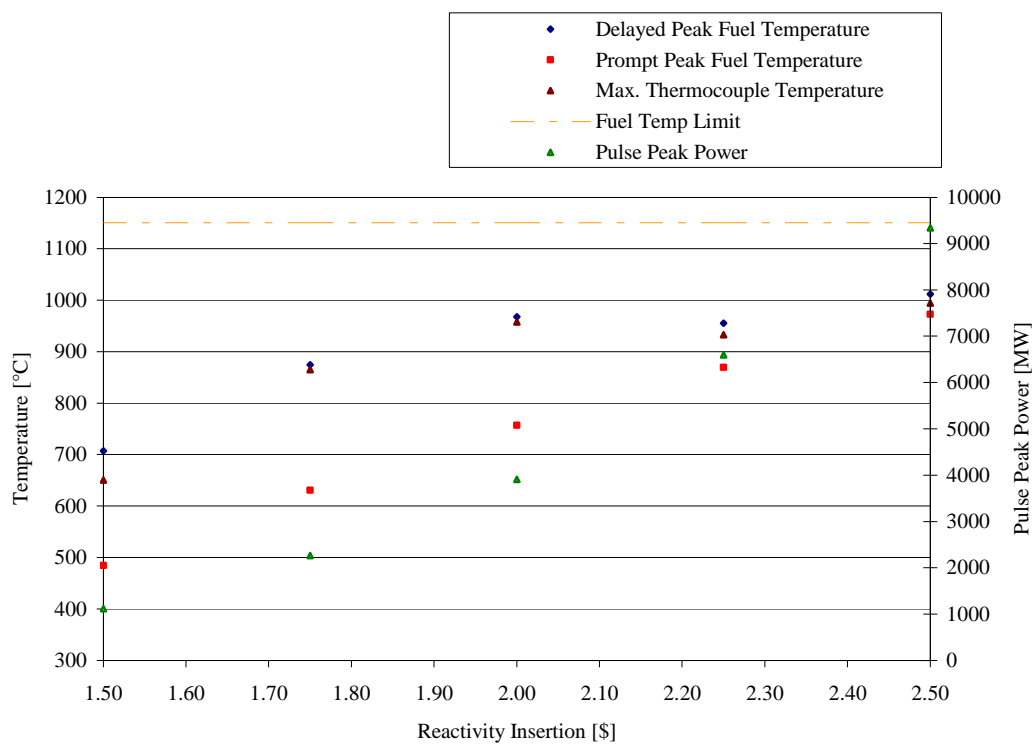


Figure A.74: Pulse Summary (LEU End of Life ICIT Core).

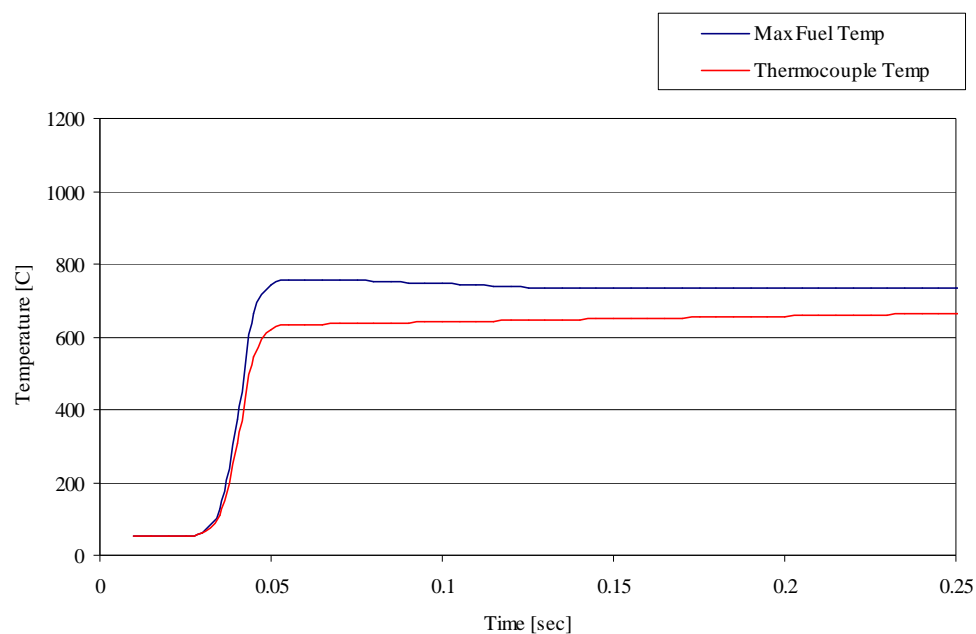


Figure A.75: LEU End of Life, Short Hot Channel Fuel Temperatures (\$2.00 Pulse)

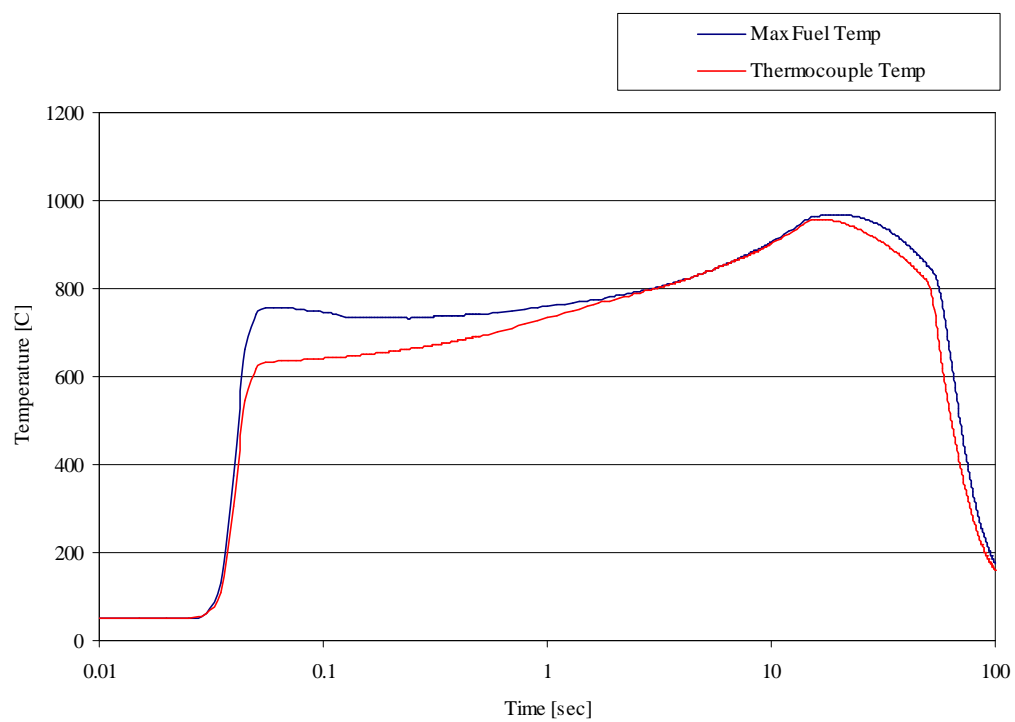


Figure A.76: LEU End of Life, Long Hot Channel Fuel Temperatures (\$2.00 Pulse)

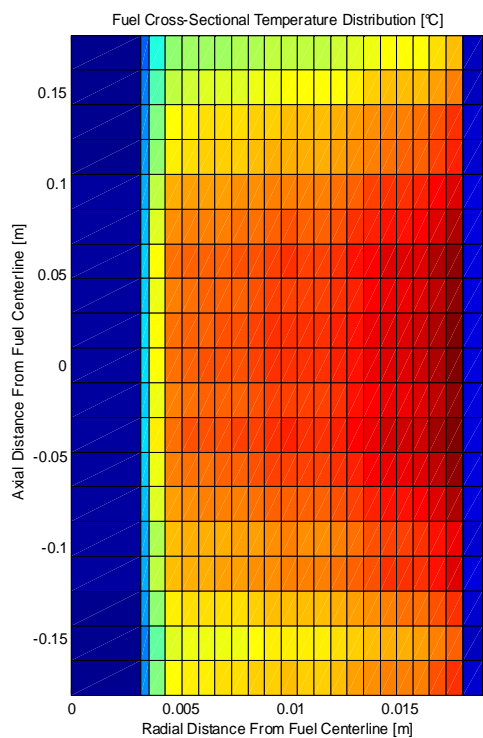


Figure A.77: Fuel Temperature Distribution at Time of Prompt Max Fuel Temperature

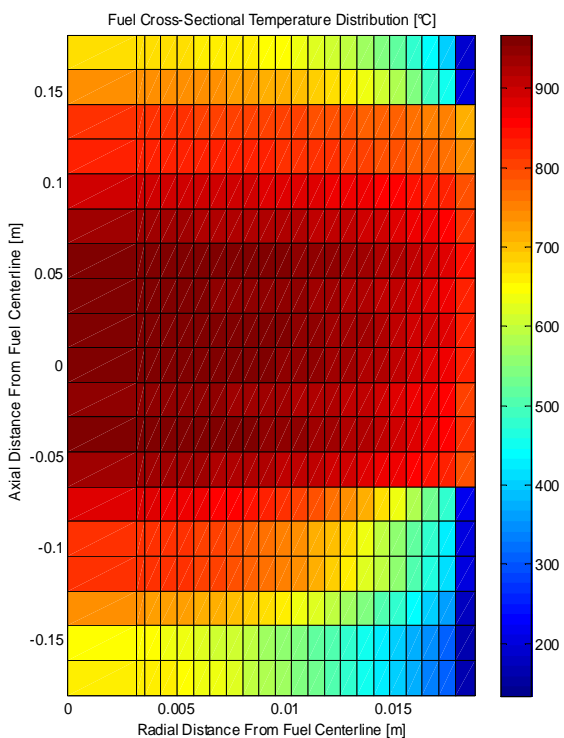


Figure A.78: Fuel Temperature Distribution at Time of Prompt Max Fuel Temperature

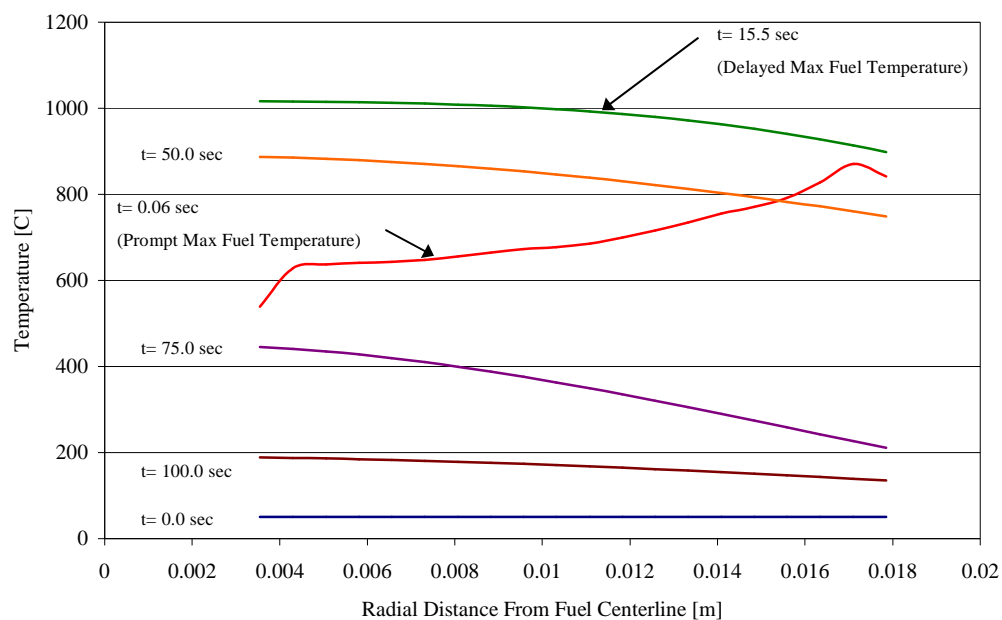


Figure A.79: LEU End of Life ICIT, Radial Temp. Profile after Pulse (\$2.00 Insertion)

Table A.14: Summary of LEU End of Life ICIT Pulse Behavior

LEU-EOL ICIT Core Configuration Pulse Results Summary					
Reactivity Insertion [\$]	1.50	1.75	2.00	2.25	2.50
Peak Total Core Power [MW]	1120.09	2268.33	3908.95	6598.40	9339.51
Delayed Peak Fuel Temperature °C	707.00	874.20	967.40	955.20	1011.60
Prompt Peak Fuel Temperature °C	484.33	630.44	757.00	869.60	972.40
Max. Thermocouple Temperature °C	650.64	865.10	957.40	932.80	994.40

As can be seen from Figure A.73, and Table A.13, the LEU Middle of Life ICIT Core is the bounding ICIT core in terms of maximum fuel temperature produced for a given reactivity insertion.

Peak temperature observed during a pulse is linearly proportional to the prompt reactivity insertion. Linear extrapolation of the peak temperatures associated with the \$2.00 and \$2.20 pulses in the LEU Middle of Life ICIT core indicate that a peak fuel temperature of 950°C do to the prompt maximum fuel temperature will be produced by the insertion of \$2.18 in the limiting core. A pulse reactivity insertion limit of \$2.15 will ensure that at all times in core life, and in all core configurations, the maximum fuel temperature in the core will not exceed 950°C.

B APPENDIX (PRKE Derivation)

B.1 PRKE Derivation

Equations (B.1) and (B.2) repeats the point reactor kinetic equations presented in Chapter 6, while Equations (B.3) and (B.4) are coupled equations to the PRKEs that allow for the incorporation of the OSTR fuel properties during a pulse. The following, section describes the discretization process used to explicitly solve the point reactor kinetic equations for the OSTR during a pulse using the Integral factor method.

$$\frac{d}{dt}P(t) = \left(\frac{\rho(t) - \beta}{\Lambda} \right) P(t) + \sum_{i=1}^6 \lambda_i C_i(t) \quad \text{Equation (B.1)}$$

$$\frac{d}{dt}C_i(t) = -\lambda_i C_i(t) + \frac{\beta_i}{\Lambda} P(t), \quad i = 1 \dots 6 \quad \text{Equation (B.2)}$$

The inherent reactivity control mechanism found in TRIGA[®] reactors is dominated by the prompt fuel temperature coefficient (α_T), and can be solved within the point reactor kinetics equations as follows:

$$\int_{\rho_o}^{\rho} d\rho = \int_{T_o}^T \alpha(T') dT' \quad \text{Equation (B.3)}$$

As presented in Equation (B.3), the prompt fuel temperature coefficient is a temperature dependent property of the fuel. Because of the extremely short time scale in which the majority of energy during a pulse is deposited in the fuel it is assumed that the core fuel is adiabatic during the process. Equation (B.4) solves for the fuel temperature during a pulse.

$$C_p(T') \frac{dT'}{dt} = P(t) \quad \text{Equation (B.4)}$$

From Equation (B.1), rewrite as:

$$\frac{dP(t)}{dt} - AP(t) = SUM \quad \text{Equation (B.5)}$$

Where:

$$A = \left(\frac{\rho(t) - \beta}{\Lambda} \right) \quad \text{and} \quad SUM = \sum_{i=1}^6 \lambda_i C_i(t)$$

The definition for Λ is as follows:

$$\Lambda(t) = \frac{\ell}{k(t)} \quad \text{and} \quad k(t) = \frac{1}{(1 - \rho(t))}$$

Then,

$$\Lambda(t) = \ell(1 - \rho(t))$$

From this, A becomes:

$$A = \left(\frac{\rho(t) - \beta}{\ell(1 - \rho(t))} \right)$$

The solution will be taking on some exponential function to get:

$$\exp(-At) \frac{dP(t)}{dt} - \exp(-At) AP(t) = \exp(-At) SUM$$

upon simplifying it becomes:

$$\frac{d}{dt} [\exp(-At) P(t)] = \exp(-At) SUM$$

Now the equation can be integrated over a generic time step and finally simplified to get:

$$P_{n+1} = P_n \exp(A\Delta t_{n+1}) + \frac{SUM_n}{A} [\exp(-A\Delta t_{n+1}) - 1] \quad \text{Equation (B.6)}$$

Equation (B.6) is the first of 9 equations. The precursor concentrations are now developed.

Multiplying Equation (B.2) through by $\exp(\lambda_i t)$ yields:

$$\frac{d}{dt} [\exp(\lambda_i t) C_i(t)] = \exp(\lambda_i t) \left[\frac{\beta_i}{\ell(1-\rho(t))} \right] P(t) \quad \text{Equation (B.7)}$$

Again the equation can be integrated over a generic time step to achieve:

$$C_{i,n+1} = C_{i,n} \exp(-\lambda_i \Delta t_{n+1}) + \left[\frac{\beta_i}{\ell(1-\rho_n)} \right] \int_{t_n}^{t_{n+1}} \exp(-\lambda_i t') P(t') dt'$$

In order to solve for $P(t')$ the trapezoid rule is used to obtain:

$$P(t') = \frac{1}{2} [P_n + P_{n+1}]$$

Now the integral can be completed and through simplification of the precursor equation one can obtain:

$$C_{i,n+1} = C_{i,n} \exp(-\lambda_i \Delta t_{n+1}) + \left[\frac{P_n + P_{n+1}}{2} \right] \left[\frac{\beta_i}{\ell(1-\rho_n)} \right] \left[\frac{1 - \exp(-\lambda_i \Delta t_{n+1})}{\lambda_i} \right] \quad \text{Equation (B.8)}$$

Equation (B.8) represents six of the nine equations that are coupled together, where i represents one of six delayed neutron groups.

Equation (B.4) is then integrated:

$$\int C_p(T') dT' = \int \frac{dP}{dt}$$

The specific volume is a linearly temperature dependent function as follows while the numerical definition for TRIGA[®] fuel is identified in Equation (4.9) of Chapter 4:

$$C_p(T) = C_{p0} + C_{p1} \cdot T$$

Then after integrating the temperature:

$$C_p(T) = C_{p0} \cdot T + \frac{C_{p1}}{2} \cdot T^2$$

Then:

$$\left[C_{p0} \cdot T_{n+1} + \frac{C_{p1}}{2} \cdot T_{n+1}^2 \right] - \left[C_{p0} \cdot T_n + \frac{C_{p1}}{2} \cdot T_n^2 \right] - \left[\frac{P_{n+1} + P_n}{2} \right] \cdot \Delta t_{n+1} = 0$$

Simplifying the quadratic equation above for temperature the following equation is produced:

$$T_{n+1} = \frac{-C_{p0} + \left\{ C_{p0}^2 + 2 \cdot C_{p1} \cdot \left[\left(C_{p0} \cdot T_n + \frac{C_{p1}}{2} \cdot T_n^2 \right) + \left(\frac{P_{n+1} + P_n}{2} \right) \cdot \Delta t_{n+1} \right] \right\}^{\frac{1}{2}}}{C_{p1}} \quad \text{Equation (B.9)}$$

Lastly, the reactivity must be coupled into the iteration by incorporating the prompt fuel temperature coefficient; the definition of reactivity presented in Equation (B.3) can be explicitly solved as seen in Equation (B.10).

$$\rho_{n+1} = \rho_n + \alpha(T_{n+1}) \cdot (T_{n+1} - T_n) \quad \text{Equation (B.10)}$$

The prompt neutron lifetime ℓ , effective delayed neutron fraction β , and prompt temperature coefficient α_F for all core configurations considered during the core conversion project as a result of the MCNP analysis are summarized in Table B.1.

Table B.1: Summary of Fuel Fissile Characteristics [65]

	Description	HEU BOL	HEU MOL	HEU EOL	LEU BOL	LEU MOL	LEU EOL
(ℓ)	Prompt Neutron Lifetime [μsec]	18.7 ±2.8	32.5 ±3.1	37.1 ±2.9	22.6 ±2.9	19.0 ±1.9	30.7 ±2.8
(β)	Effective Delayed Neutron Fraction	0.0076 ±0.0002	0.0078 ±0.0002	0.0073 ±0.0002	0.0076 ±0.0001	0.0073 ±0.0002	0.0075 ±0.0002
(α_F)	Prompt Temperature Coefficient [(%Δk/k)/°C]	2.601E-05T - 2.872E-04	1.886E-05T - 2.926E-05	1.433E-05T + 1.092E-03	1.797E-05T + 1.065E-03	1.320E-05T + 1.161E-03	8.733E-06T + 2.167E-03

Equation (B.6) and (B.8) require information regarding individual group delayed neutron decay constants. It is assumed that the only fissile isotope in the point reactor kinetics model is ^{235}U . The decay constants for this isotope are summarized in Table B.2:

Table B.2: U-235 Delayed Neutron Group Half-Life Values [78]

²³⁵ U properties	
Group	Half-Life sec
1	54.51
2	21.84
3	6.000
4	2.230
5	0.496
6	0.179

The decay constant for a given isotope is as follows:

$$\lambda_i = \frac{\ln(2)}{t_{1/2_i}}$$

As a result of this definition the decay constants for the six groups presented in the table above are as shown in **Table B.3**:

Table B.3: U-235 Delayed Neutron Group Decay Constant Values

²³⁵ U properties	
Group	Decay Constant [1/sec]
1	0.01272
2	0.03174
3	0.11552
4	0.31083
5	1.39747
6	3.87233

B.2 MATLAB® Code

```

%%%%%%%%%%%%%%%%%%%%%%%%%%%%%%%%%%%%%%%%%%%%%%%%%%%%%%%%%%%%%%%%%%%%%%%%%%%%%%
%      Numerical Solutions of Point Reactor Kinetics Equations      %
%      By: Wade Marcum                                           %
%                                                                    %
%      "Integration Factor Method"                                  %
%                                                                    %
%      This program is built to give the user the ability to solver the %
%      the point reactor kinetics equations using integration factor method. %
%                                                                    %
%      Note:  Constants hard-coded are referred to for U-235 specifically %
%=====

```

```

clear all
clc
fprintf('1)  HEU BOL\n2)  HEU MOL\n3)  HEU EOL\n4)  LEU BOL\n5)  LEU MOL\n6)  LEU
EOL\n7)  Simnad\n');
which=input('Which Core Configuration [1-6]?: ');
%HEU BOL
if which==1
    beta=0.0075;
    alphaT=inline('2.601E-07*T-2.872E-06', 'T');
    L=18.7E-6;
    Cp0=69058;
    Cp1=141.68;
end
% HEU MOL
if which==2
    beta=0.0078;
    alphaT=inline('1.886E-07*T-2.926E-05', 'T');
    L=32.5E-6;
    Cp0=69058;
    Cp1=141.68;
end
% HEU EOL
if which==3
    beta=0.0073;
    alphaT=inline('1.433E-07*T+1.092E-05', 'T');
    L=37.1E-6;
    Cp0=69058;
    Cp1=141.68;
end
% LEU BOL
if which==4
    beta=0.0076;
    alphaT=inline('1.797E-07*T+1.065E-05', 'T');
    L=22.6E-6;
    Cp0=69058;
    Cp1=141.68;
end
% LEU MOL
if which==5
    beta=0.0073;
    alphaT=inline('1.320E-07*T+1.161E-05', 'T');
    L=19.0E-6;
    Cp0=69058;
    Cp1=141.68;
end
% LEU EOL
if which==6
    beta=0.0075;
    alphaT=inline('8.733E-08*T+2.167E-05', 'T');
    L=30.7E-6;
    Cp0=69058;
    Cp1=141.68;
end
if which==7
    beta=0.0073;
    alphaT=9.6E-5;
    L=3.2E-5;
    Cp0=128000.0;
    Cp1=257.6;
end
end

```

```

% Implementing the Core Configuration Information to the U-235 properties
%-----%
L=L; % mean neutron generation time
hl=[54.51 21.84 6 2.23 0.496 .179]; % half lives for 6 groups
dc=log(2)./hl; % decay constants for 6 groups
betai=[.038 .213 .188 .407 .128 .026]; % Relative Yield
beta=beta; % average delayed neutron fraction
bi=betai.*beta; % delayed neutron fraction for each group
Cp0=Cp0; % Specific Heat Constant
Cp1=Cp1; % Specific Heat Slope

% Time-step Solution Parameters
%-----%
finish=.15; % end of t interval sec
%%step=input('Enter value for step size sec: '); % t step size sec
step=1E-5; % time step size sec
count=finish/step+1; % # of steps that will be taken
t=(0:count); % Iteration Number
ttime(1)=0;
for tt=2:count+1
    ttime(tt)=ttime(tt-1)+step;
end

% System Parameter inputs
%-----%
%%Power(1)=input('Enter value for initial power [W]: ');
%%dollars=input('Enter value for initial reactivity [$]: ');
%%Temp(1)=input('Energy value for initial temperature °C: ');
Power=1.05E3;
dollars=2.0;
Temp=50;
rho=dollars*beta;

% Solving Using integration factor
%-----%
for i=1:6
    C(i)=(bi(i))/(dc(i)*L*(1-rho(1)))*Power(1);
end

for j=1:count-1
    A=(rho(j)-beta)/(L*(1-rho(j)));

    % Power Calculation
    Power(j+1)=(Power(j)*exp(A*step)+((sum(C))/A)*(exp(A*step)-1));

    % Precursor Calculation
    for i=1:6
        C(i)=C(i)*exp(-dc(i)*step)+(Power(j)+Power(j+1))*(1/2)*(bi(i)/(L*(1-rho(j))))*(1-exp(-dc(i)*step))/dc(i);
    end

    % Temperature Calculation
    X=(step)*(Power(j+1)+Power(j))/2;
    Y=Cp0*Temp(j)+(1/2)*Cp1*(Temp(j))^2;
    c=-1*(X+Y);
    a=(Cp1)/2;
    b=Cp0;
    Temp(j+1)=(-b+sqrt(b^2-4*a*c))/(2*a);

    % Reactivity Calculation
    if which==7
        rho(j+1)=rho(j)-alphaT*(Temp(j+1)-Temp(j));
    else
        rho(j+1)=rho(j)-alphaT*(Temp(j+1))*(Temp(j+1)-Temp(j));
    end
end
end

```

C APPENDIX (OSTR Experimental Temperature Mapping)

C.1 Introduction

The objective of this experiment is to map the coolant temperature at different axial locations within the OSTR core in order to provide general feedback toward discrepancies found in the RELAP5-3D model developed for the OSTR core conversion project. Temperature readings are taken at 1.0 MW_{th} power steady state reactor operation.

C.2 Equipment and Methods

C.2.1 Data Acquisition Equipment

Table C.1: Equipment used for Temperature Measurement

Equipment	Brand	Model Number
Thermocouples	Omega	TJ36-CASS-116U-240
Signal Conditioning Unit	HP Agilent	34970A
Computer	Dell	E1705
Transmitter Module	GBIP/USB Interface	82352357A
DAQ User Interface	LabVIEW	7.1

C.2.2 Hardware Acquired for Experimental Assembly

Table C.2: Hardware Acquired for Experimental Assembly

Part	Description	Brand	Part Number	Qty.
Aluminum Channel	Alloy 6063 Al., 1/8" Thick, 4" Base x 1" Legs, 8' lg.	McMasterCarr	9001K13	1
Aluminum Tubing	6061 Al., 1/4" OD, .12" ID, .065 Thick, 6' Length	McMasterCarr	89965K44	17
Tube Union	Al. Tube Union	Swagelok	A-400-6	16
Thermocouples	Type K S.S. Sheathed	Omega	TJ36-CASS-116U-240	5

C.2.3 Overview of Experimental Procedure

- 1) Develop LabVIEW program to actively collect, correct, adjust, and calibrate thermocouple measurement for over a known time interval at a given acquisition frequency. A block diagram of the LabVIEW code logic that was implemented during the experiment is presented in Figure C.1.

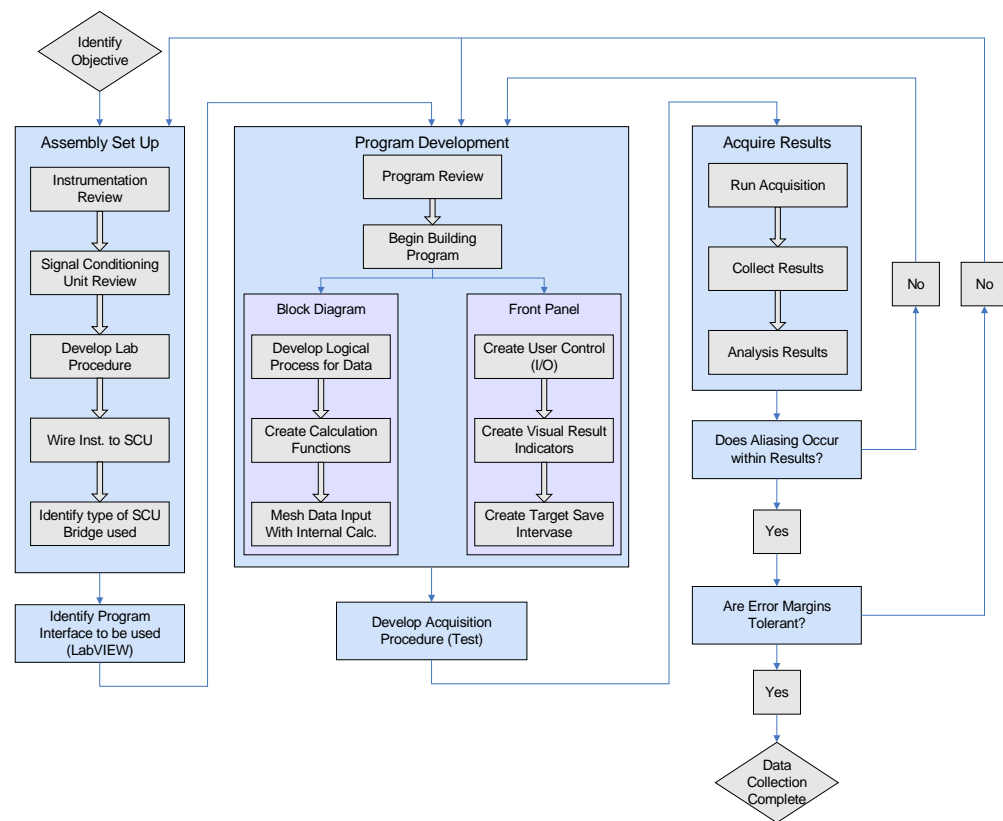


Figure C.1: Block Diagram of LabVIEW code logic implemented during the experiment

- 2) Connect data acquisition (DAQ) bucket, Agilent 34970A, to computer model and Interface with LabVIEW.



Figure C.2: The Assembled Configuration of the DAQ Bucket to Computer Module

- 3) Connect thermocouples to DAQ bucket deck module and insert deck into DAQ Bucket.
- 4) Calibrate thermocouples through “shunt” calibration method within LabVIEW Program.

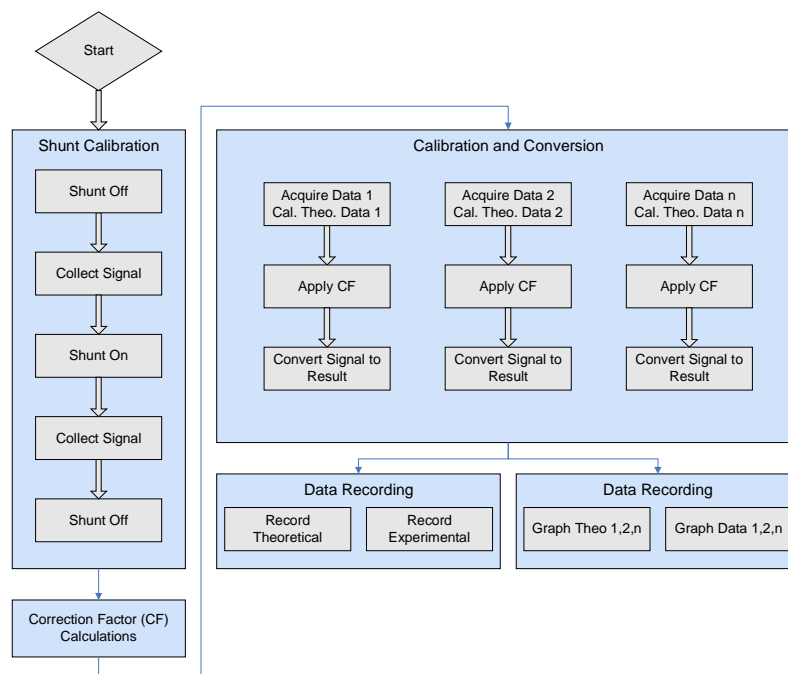


Figure C.3: Block Diagram of the Methodology Used to Conduct the Shunt Calibration

- 5) Verify OSTR is at 1MW_{th} steady state power.

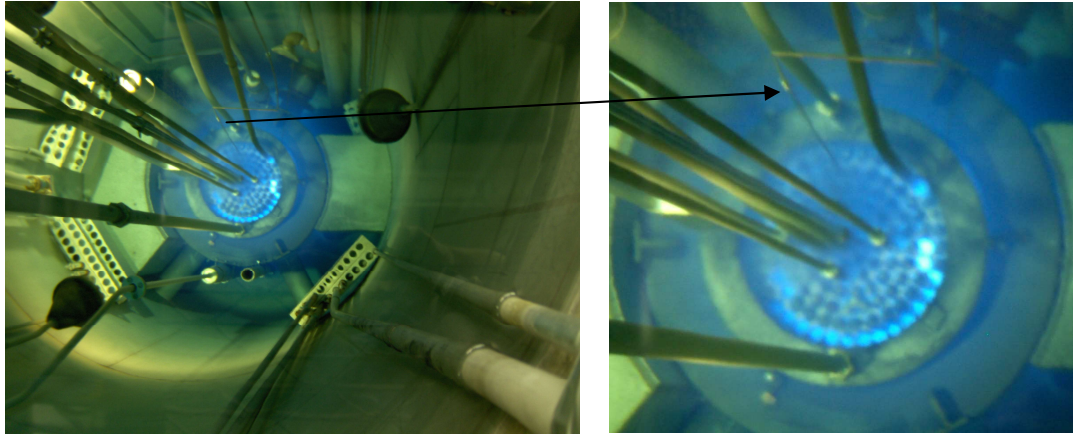


Figure C.4: Picture of the Thermocouple in the OSTR core at Steady State Operation

- 6) Verify that the Thermocouple is in the correct location within the OSTR Core

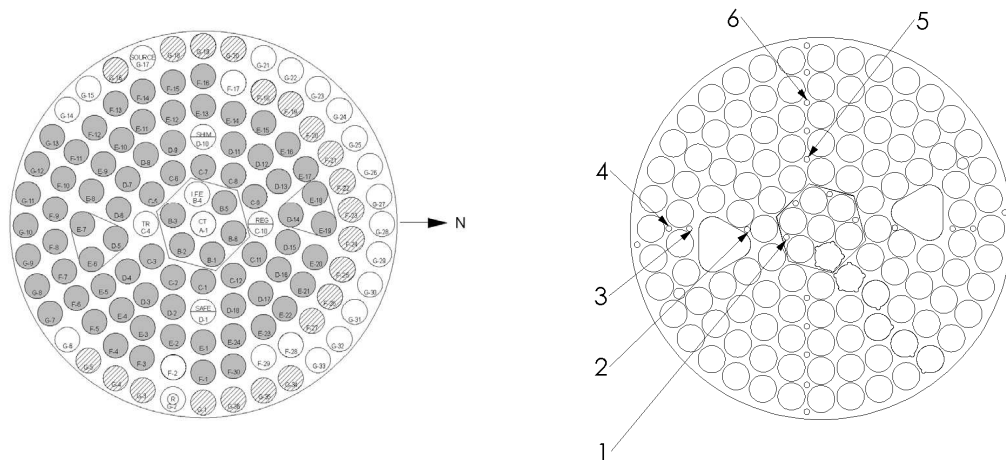


Figure C.5: Components Comprising Current OSTR Core and Measurement Locations

- 7) Start data acquisition through DAQ bucket.
- 8) Start LabVIEW program (record data to hard drive).

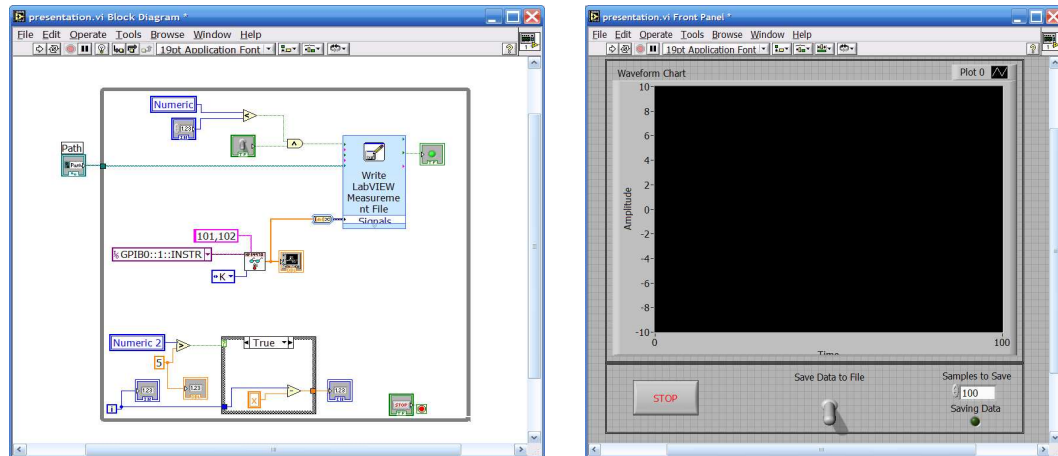


Figure C.6: Figure of Code and Front Panel of LabVIEW Developed for the Experiment

9) End data acquisition after 60 seconds (1000 readings).

10) Write data to file on hard drive.

C.3 Results

Figure C.7 through Figure C.12 identify the axial bulk coolant temperature distribution with reference to their radial core location which can be identified in Figure C.5.

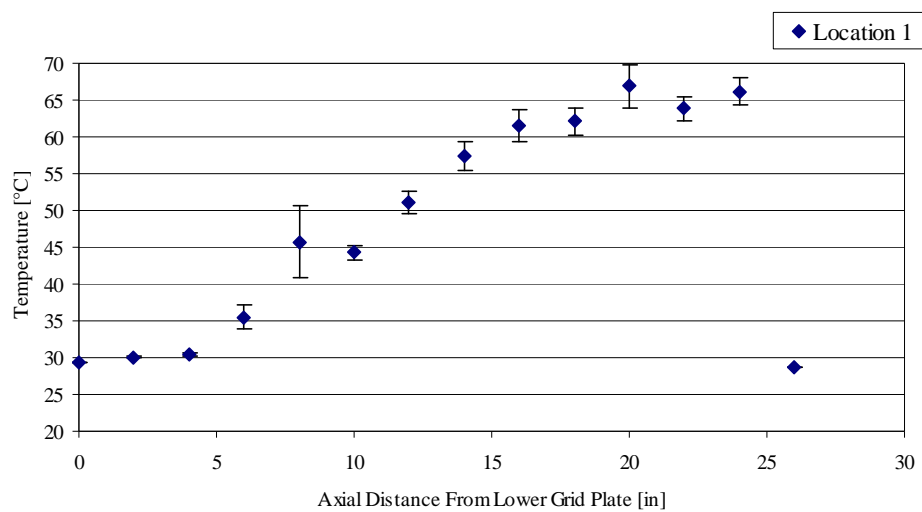


Figure C.7: Axial Bulk Coolant Temperature Distribution at Location 1 (Figure C.5)

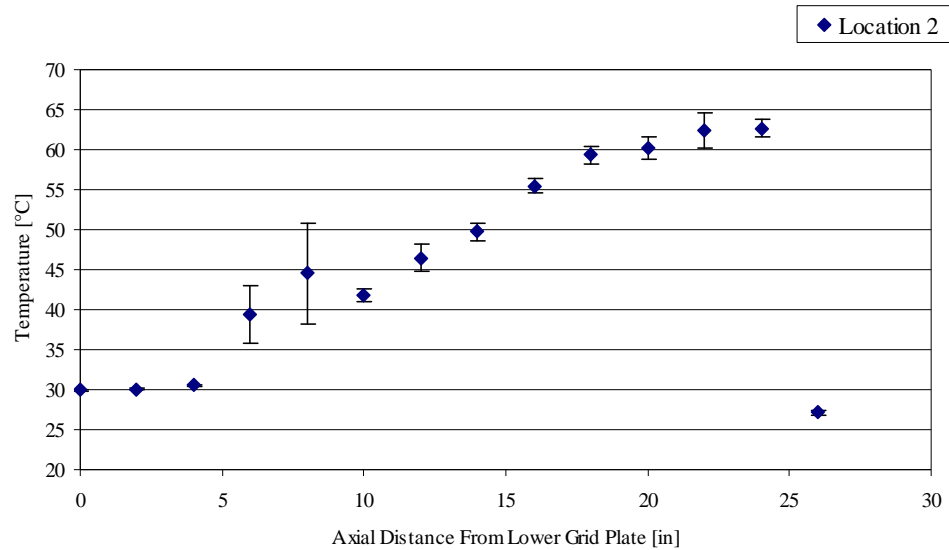


Figure C.8: Axial Bulk Coolant Temperature Distribution at Location 2 (Figure C.5)

Figure C.7 and Figure C.8 presents evidence that cross flow between the advancement subchannels located next to “Location 1” and “Location 2” are negligibly small compared to the primary vertical velocity vector. This is because the axial bulk coolant temperature distribution resembles the theoretical sine function that is typical of a single channel temperature distribution. This is further reassured by the radial location in the core in which these temperature readings were taking. Location 1 and Location 2 are located near the largest heat production region in the core, therefore the heat flux produced by a given fuel element adjacent to the location in which Figure C.7 and Figure C.8 were taken, deposits more enthalpy into the fluid than those located in outer radial regions within the core, thereby increasing the buoyancy forces on the fluid in that given subchannel and increasing the local axial velocity in the vertical direction.

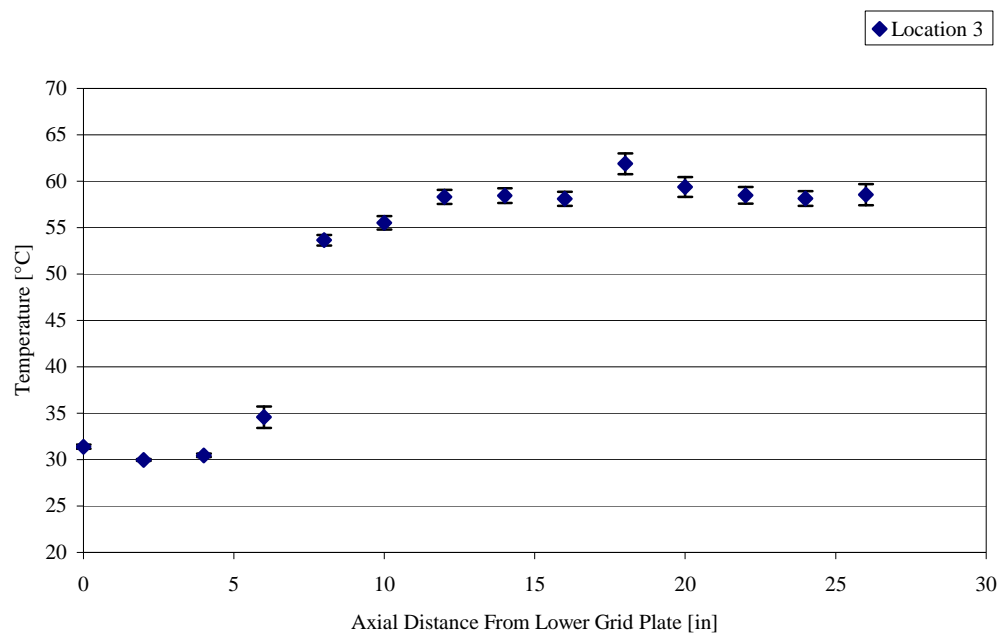


Figure C.9: Axial Bulk Coolant Temperature Distribution at Location 3 (Figure C.5)

Evidence of cross flow in the lower power density regions of the core can be found in Figure C.9 through Figure C.12 where large fluctuations in the axial bulk coolant temperature distribution can be observed.

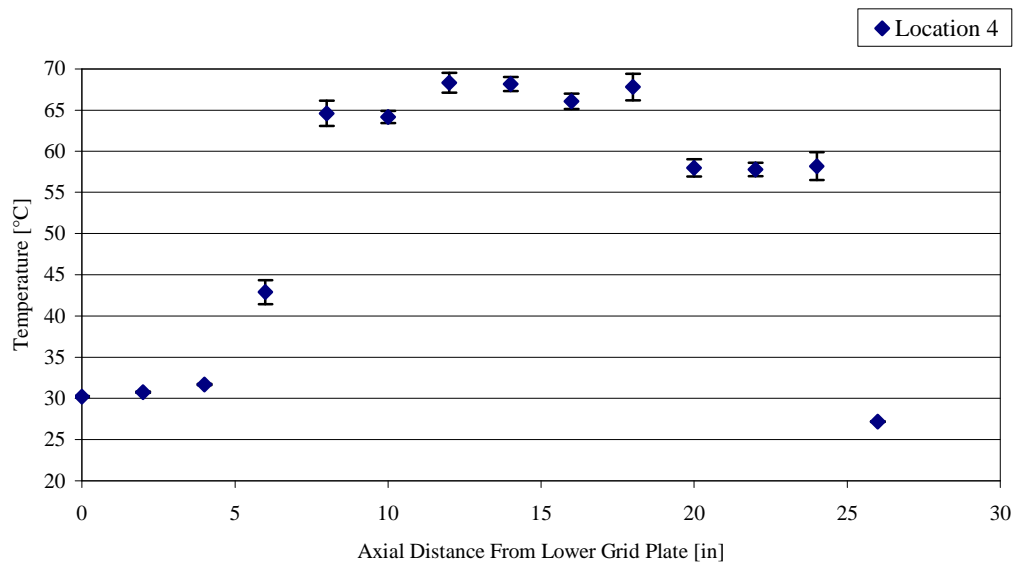


Figure C.10: Axial Bulk Coolant Temperature Distribution at Location 4 (Figure C.5)

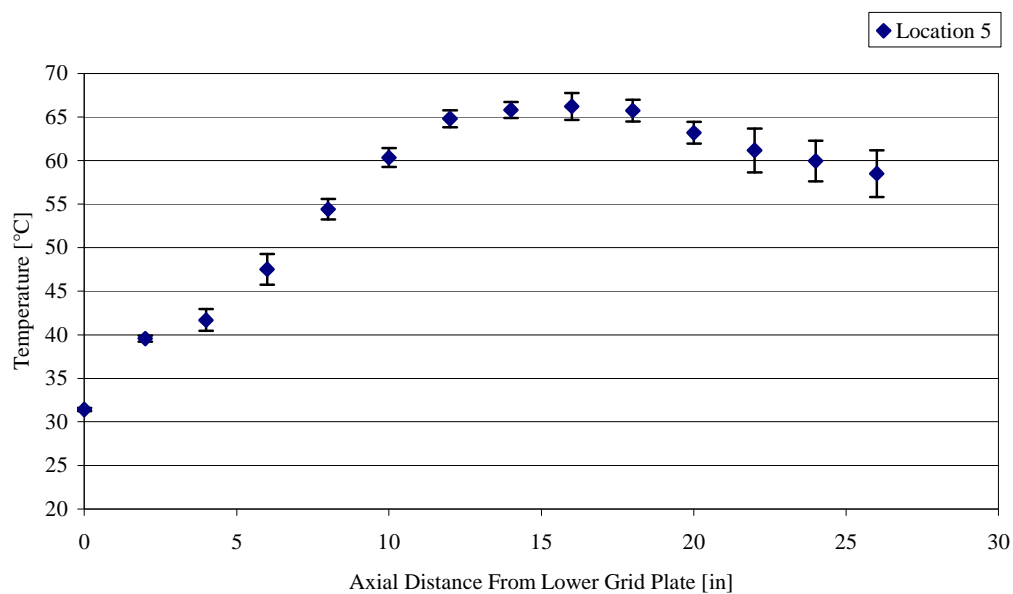


Figure C.11: Axial Bulk Coolant Temperature Distribution at Location 5 (Figure C.5)

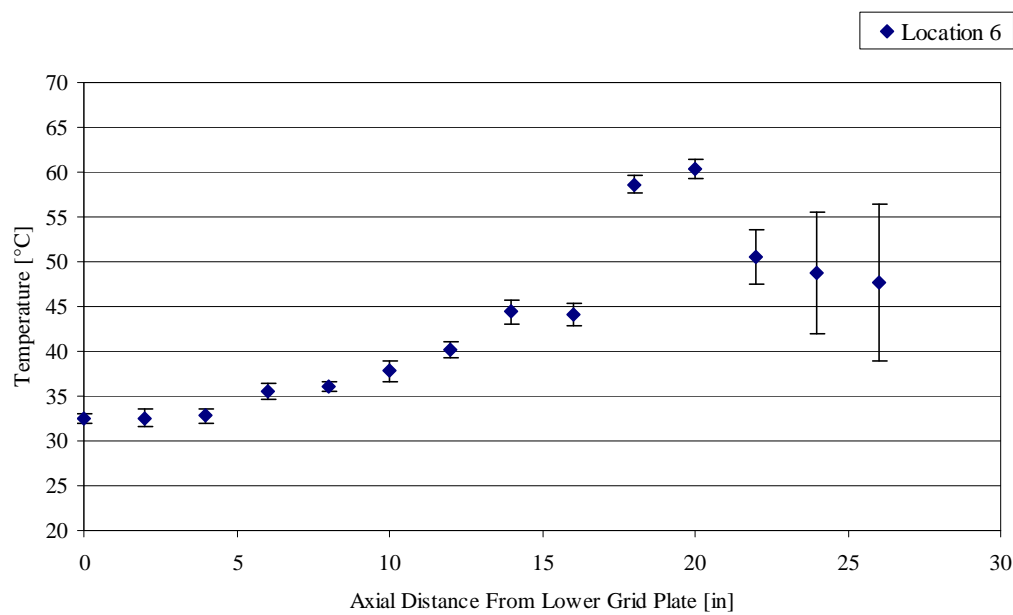


Figure C.12: Axial Bulk Coolant Temperature Distribution at Location 6 (Figure C.5)

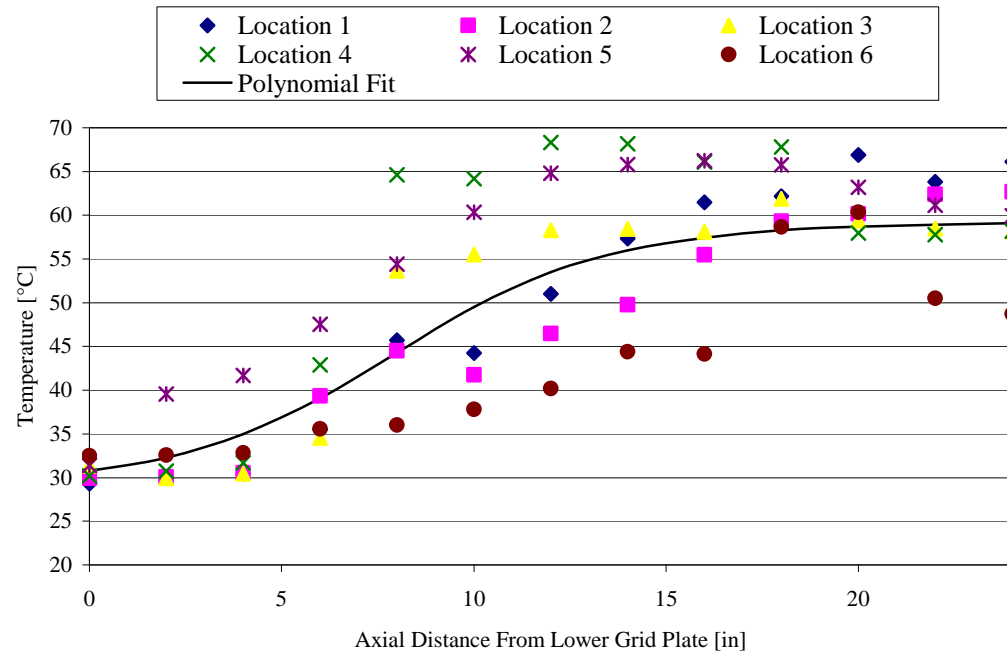


Figure C.13: Axial Bulk Coolant Temperature Distribution Summary

Figure C.13 provides a summary of all axial bulk coolant temperature distributions measured during the experiment. Additionally a trend line is presented in the figure above; all temperature readings were averaged at each given axial location in the core and a third order polynomial trend line was fit to the average. As a result of this, a general sine distribution can be seen in average axial bulk coolant temperature measurements taken during the experiment, providing information toward the average bulk coolant velocity direction in the core.